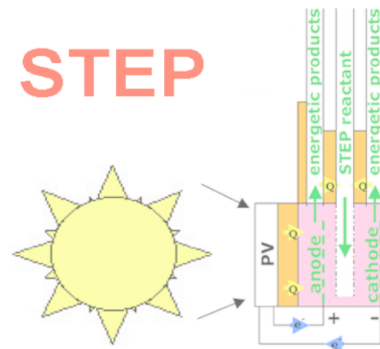


A fundamental, new solar process has been introduced, the **STEP** process, which efficiently removes carbon from the atmosphere and generates the staples needed by society, ranging from fuels, to metals, bleach and construction materials, at high solar efficiency and without carbon dioxide generation. By using the full spectrum of sunlight, **STEP** captures more solar energy than the most efficient solar cell or photoelectrochemical processes.

-STEP's concentrated sunlight drives new high temperature molten CO₂-free syntheses at industrial production rates.



Included are four Technical Write-ups of:

- 1) **STEP 2011** -Includes theory, solar efficiency, and individual STEP processes for Fuels, Metals, Bleach and Desalinization.
- 2) **STEP Cement 2012**
- 3) **STEP Iron 2013**
- 3) **STEP Fertilizer 2014**
- 4) **The import of electrochemistry in solar energy conversion**
Nature cover article 1987

Further information available at Licht research group sites:

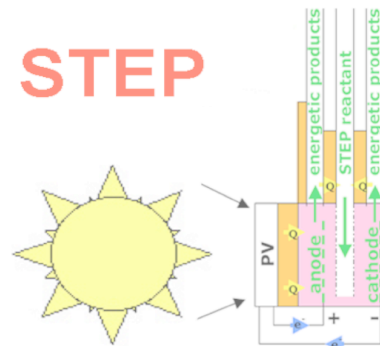
<http://home.gwu.edu/~slicht/index.html>

<http://departments.columbian.gwu.edu/chemistry/people/103>

The **Licht research group** has taken on the challenge of *a comprehensive solution to climate change*. We're working towards changing today's fossil fuel, to a renewable chemical economy, replacing the largest greenhouse gas emitters, including iron & fuel production, by new, inexpensive, solar, CO₂-free, chemistries.

A fundamental, new solar process has been introduced, the **STEP** process, which efficiently removes carbon from the atmosphere and generates the staples needed by society, ranging from fuels, to metals, bleach and construction materials, at high solar efficiency and without carbon dioxide generation. By using the full spectrum of sunlight, **STEP** captures more solar energy than the most efficient solar cell or photoelectrochemical processes.

-STEP's concentrated sunlight drives new high temperature molten CO₂-free syntheses at industrial production rates.



Included are three Technical Write-ups (in order) of:

1) STEP 2011 -Includes theory, solar efficiency, and individual STEP

processes for Fuels, Metals, Bleach and Desalinization.

2) STEP Cement 2012

3) STEP Iron 2013

Further information available at Licht research group sites:

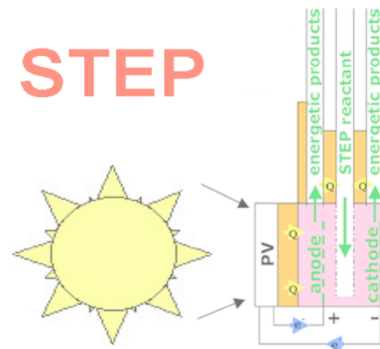
<http://home.gwu.edu/~slicht/index.html>

<http://departments.columbian.gwu.edu/chemistry/people/103>

The **Licht research group** has taken on the challenge of *a comprehensive solution to climate change*. We're working towards changing today's fossil fuel, to a renewable chemical economy, replacing the largest greenhouse gas emitters, including iron & fuel production, by new, inexpensive, solar, CO₂-free, chemistries.

A fundamental, new solar process has been introduced, the **STEP** process, which efficiently removes carbon from the atmosphere and generates the staples needed by society, ranging from fuels, to metals, bleach and construction materials, at high solar efficiency and without carbon dioxide generation. By using the full spectrum of sunlight, **STEP** captures more solar energy than the most efficient solar cell or photoelectrochemical processes.

-STEP's concentrated sunlight drives new high temperature molten CO₂-free syntheses at industrial production rates.



Included are four Technical Write-ups of:

- 1) **STEP 2011** -Includes theory, solar efficiency, and individual STEP processes for Fuels, Metals, Bleach and Desalinization.
- 2) **STEP Cement 2012**
- 3) **STEP Iron 2013**
- 4) **The import of electrochemistry in solar energy conversion**

Nature cover article 1987

Further information available at Licht research group sites:

<http://home.gwu.edu/~slicht/index.html>

<http://departments.columbian.gwu.edu/chemistry/people/103>

The **Licht research group** has taken on the challenge of *a comprehensive solution to climate change*. We're working towards changing today's fossil fuel, to a renewable chemical economy, replacing the largest greenhouse gas emitters, including iron & fuel production, by new, inexpensive, solar, CO₂-free, chemistries.

In the field of energy storage for devices ranging from EVs to consumer electronics and peak power storage, we're pioneering the study of new multiple electron (per molecule) storage processes, to learn to create batteries with greater storage capacity than gasoline.



Included are Technical Write-ups of:

- 1) Molten Air Batteries (selected publications from 2013-onward)
- 2) The VB_2 /Air Battery (selected publications from 2008-onward)
- 3) Super-iron Batteries (selected publications from 1999-onward)
- 4) Sulfur Batteries (select publication from 1987-onward)



Further information available at Licht research group sites:

<http://home.gwu.edu/~slicht/index.html>

<http://departments.columbian.gwu.edu/chemistry/people/103>

The **Licht research group** has taken on the challenge of *a comprehensive solution to climate change*. We're working towards changing today's fossil fuel, to a renewable chemical, economy, replacing the largest greenhouse gas emitters, and discovering new high energy, highest storage capacity batteries.

In the field of energy storage for devices ranging from EVs to consumer electronics and peak power storage, we're pioneering the study of new multiple electron (per molecule) storage processes, to learn to create batteries with greater storage capacity than gasoline.



Included are Technical Write-ups of:

- 1) Molten Air Batteries (selected publications from 2013-onward)
- 2) The VB₂/Air Battery (selected publications from 2008-onward)
- 3) Super-iron Batteries (selected publications from 1999-onward)
- 4) Sulfur Batteries (select publication from 1987-onward)



Further information available at Licht research group sites:

<http://home.gwu.edu/~slicht/index.html>

<http://departments.columbian.gwu.edu/chemistry/people/103>

The **Licht research group** has taken on the challenge of *a comprehensive solution to climate change*. We're working towards changing today's fossil fuel, to a renewable chemical, economy, replacing the largest greenhouse gas emitters, and discovering new high energy, highest storage capacity batteries.

Efficient Solar-Driven Synthesis, Carbon Capture, and Desalinization, STEP: Solar Thermal Electrochemical Production of Fuels, Metals, Bleach

S. Licht*

STEP (solar thermal electrochemical production) theory is derived and experimentally verified for the electrosynthesis of energetic molecules at solar energy efficiency greater than any photovoltaic conversion efficiency. In STEP the efficient formation of metals, fuels, chlorine, and carbon capture is driven by solar thermal heated endothermic electrolyses of concentrated reactants occurring at a voltage below that of the room temperature energy stored in the products. One example is CO₂, which is reduced to either fuels or storable carbon at a solar efficiency of over 50% due to a synergy of efficient solar thermal absorption and electrochemical conversion at high temperature and reactant concentration. CO₂-free production of iron by STEP, from iron ore, occurs via Fe(III) in molten carbonate. Water is efficiently split to hydrogen by molten hydroxide electrolysis, and chlorine, sodium, and magnesium from molten chlorides. A pathway is provided for the STEP decrease of atmospheric carbon dioxide levels to pre-industrial age levels in 10 years.

1. Introduction

The anthropogenic release of carbon dioxide and atmospheric carbon dioxide have reached record levels. One path towards CO₂ reduction is to utilize renewable energy to produce electricity. Another, less explored path is to utilize renewable energy to produce societal staples such as metals, bleach, and fuels (including carbonaceous fuels) directly. Whereas solar-driven water splitting to generate hydrogen fuels has been extensively studied,^[1,2] there have been few studies of solar-driven carbon dioxide splitting, although recently we introduced a global process for solar thermal electrochemical production (STEP) of energetic molecules, including CO₂ splitting.^[3–8] “CO₂ is a highly stable, noncombustible molecule, and its thermodynamic stability makes its activation energy demanding and challenging.”^[9] In search of a solution for climate change associated with increasing levels of atmospheric CO₂, the field of carbon dioxide splitting (solar or otherwise), while young, is growing rapidly, and as with water splitting, includes the study

of photoelectrochemical, biomimetic, electrolytic, and thermal pathways of carbon dioxide splitting.^[10,11]

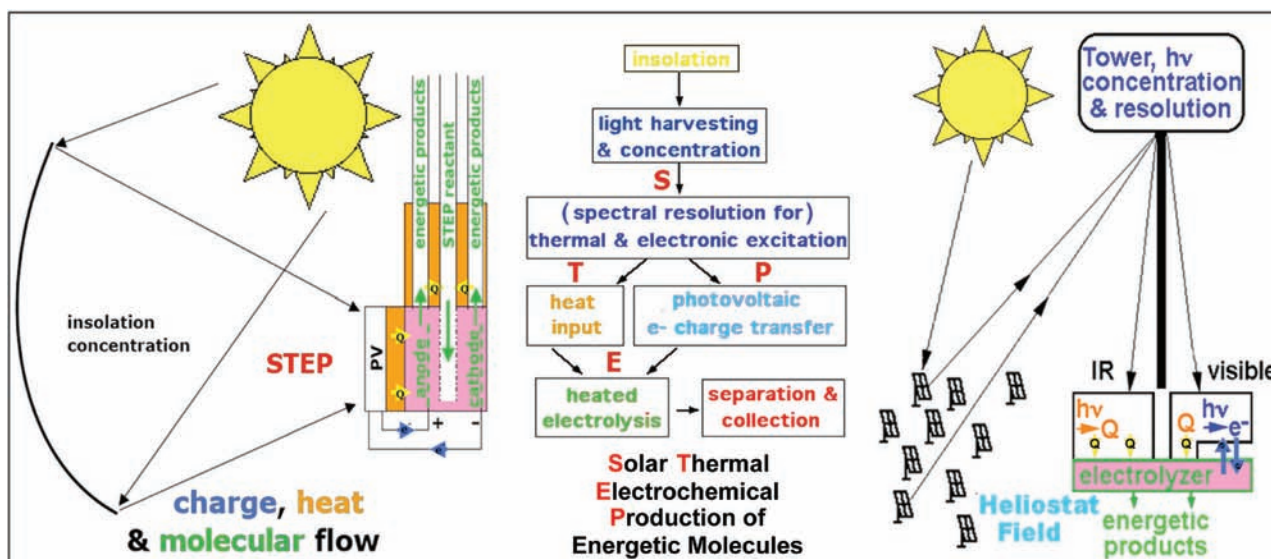
The direct thermal splitting of CO₂ requires excessive temperatures to drive any significant dissociation. As a result, lower temperature thermochemical processes using coupled reactions have recently been studied.^[12–16] The coupling of multiple reactions steps decreases the system efficiency. To date, such challenges, and the associated efficiency losses, have been an impediment to the implementation of the related, extensively studied field of thermochemical splitting of water.^[2] Photo-electrochemistry probes the energetics of illuminated semiconductors in an electrolyte, and provides an alternative path to solar fuel formation. Photoelectrochemical solar cells (PECs) can convert

solar energy to electricity,^[17–21] and with inclusion of an electrochemical storage couple, have the capability for internal energy storage to provide a level output despite variations in sunlight.^[22,23] Solar to photo-electrochemical energy can also be stored externally in chemical form, when it is used to drive the formation of energetically rich chemicals. With photochemical and photo-electrochemical splitting of carbon dioxide^[24–29] the selective production of specific fuel products has been demonstrated. Such systems function at low current density and efficiencies of ~1 percent, and as with photoelectrochemical water splitting face stability and bandgap challenges related to effective operation with visible light.^[21,30,31]

The electrically driven (nonsolar) electrolysis of dissolved carbon dioxide is under investigation at or near room temperature in aqueous, non-aqueous, and PEM media.^[32–41] These are constrained by the thermodynamic and kinetic challenges associated with ambient temperature, endothermic processes, of a high electrolysis potential, large overpotential, low rate and low electrolysis efficiency. High-temperature, solid-oxide electrolysis of carbon dioxide dates back to suggestions from the 1960s to use such cells to renew air for a space habitat,^[42–44] and the sustainable rate of the solid oxide reduction of carbon dioxide is improving rapidly.^[45–51] Molten-carbonate rather than solid-oxide fuel cells running in the reverse mode had also been studied to renew air in 2002.^[52] In a manner analogous to our 2002 high-temperature solar water-splitting studies (described below),^[53–55] we showed in 2009 that molten-carbonate cells

Prof. S. Licht
Department of Chemistry
George Washington University
Washington, DC 20052, USA
E-mail: slicht@gwu.edu

DOI: 10.1002/adma.201103198



Scheme 2. Global use of sunlight to drive the formation of energy rich molecules. Left: Charge and heat flow in STEP: heat flow (yellow arrows), electron flow (blue), & reagent flow (green). Right: Beam splitters redirect sub-bandgap sunlight away from the PV onto the electrolyzer. Modified with permission.^[3]

on tuning semiconductor bandgaps^[57] to provide a better match to the electrochemical potential (specifically, the water splitting potential), or by utilizing more complex, multiple bandgap structures using multiple photon excitation.^[58] Either of these structures are not capable of excitation beyond the bandedge and can not make use of longer wavelength sunlight. Photovoltaics are limited to super-bandgap sunlight, $h\nu > E_g$, precluding use of long wavelength radiation, $h\nu < E_g$. STEP instead directs this IR sunlight to heat electrochemical reactions, and uses visible sunlight to generate electronic charge to drive these electrolyses.

Rather than tuning the bandgap to provide a better energetic match to the electrolysis potential, the STEP process instead tunes the redox potential to match the bandgap. The right side of Scheme 1 presents the energy diagram of a STEP process. The high temperature pathway decreases the free energy requirements for processes whose electrolysis potential decreases with increasing temperature. STEP uses solar energy to drive, otherwise energetically forbidden, pathways of charge transfer. The process combines elements of solid state physics, insolation (solar illumination) and high temperature electrochemical energy conversion. Kinetics improve, and endothermic thermodynamic potentials, decrease with increasing temperature. The result is a synergy, making use of the full spectrum of sunlight, and capturing more solar energy. STEP is intrinsically more efficient than other solar energy conversion processes, as it utilizes not only the visible sunlight used to drive PVs, but also utilizes the previously detrimental (due to PV thermal degradation) thermal component of sunlight, for the electrolytic formation of chemicals.

The two bases for improved efficiencies using the STEP process are (i) excess heat, such as unused heat in solar cells, can be used to increase the temperature of an electrolysis cell, such as for electrolytic CO₂ splitting, while (ii) the product to

reactant ratio can be increased to favor the kinetic and energetic formation of reactants. With increasing temperature, the quantitative decrease in the electrochemical potential to drive a variety of electrochemical syntheses is well known, substantially decreasing the electronic energy (the electrolysis potential) required to form energetic products. The extent of the decrease in the electrolysis potential, E_{redox} , may be tuned by choosing the constituents and temperature of the electrolysis. The process distinguishes radiation that is intrinsically energy sufficient to drive PV charge transfer, and applies all excess solar thermal energy to heat the electrolysis reaction chamber.

Scheme 2 summarizes the charge, heat and molecular flow for the STEP process; the high temperature pathway decreases the potential required to drive endothermic electrolyses, and also facilitates the kinetics of charge transfer (i.e., decreases overpotential losses), which arise during electrolysis. This process consists of (i) sunlight harvesting and concentration, (ii) photovoltaic charge transfer driven by super-bandgap energy, (iii) transfer of sub-bandgap and excess super-bandgap radiation to heat the electrolysis chamber, (iv) high temperature, low energy electrolysis forming energy rich products, and (v) cycle completion by pre-heating of the electrolysis reactant through heat exchange with the energetic electrolysis products. As indicated on the right side of Scheme 2, the light harvesting can use various optical configurations; e.g. in lieu of parabolic, or Fresnel, concentrators, a heliostat/solar tower with secondary optics can achieve higher process temperatures (>1000 °C) with concentrations of ~2000 suns. Beam splitters can redirect sub-bandgap radiation away from the PV (minimizing PV heating) for a direct heat exchange with the electrolyzer.

Solar heating can decrease the energy to drive a range of electrolyses. Such processes can be determined using available entropy, S, and enthalpy, H, and free-energy, G, data,^[59b] and are identified by their negative isothermal temperature coefficient

of the cell potential.^[59a] This coefficient $(dE/dT)_{\text{isoth}}$ is the derivative of the electromotive force of the isothermal cell:

$$(dE/dT)_{\text{isoth}} = \Delta S/nF = (\Delta H - \Delta G)/nFT \quad (1)$$

The starting process of modeling any STEP process is the conventional expression of a generalized electrochemical process, in a cell which drives an n electron charge transfer electrolysis reaction, comprising “ x ” reactants, R_i , with stoichiometric coefficients r_i , and yielding “ y ” products, C_i , with stoichiometric coefficients c_i .

Electrode 1 | Electrolyte | Electrode 2

Using the convention of $E = E_{\text{cathode}} - E_{\text{anode}}$ to describe the positive potential necessary to drive a non-spontaneous process, by transfer of n electrons in the electrolysis reaction of reactants to products:

$$\sum_{i=1}^x r_i R_i \rightarrow \sum_{i=1}^y c_i C_i \quad (2)$$

At any electrolysis temperature, T_{STEP} , and at unit activity, the reaction has electrochemical potential, E°_T . This may be calculated from consistent, compiled unit activity thermochemical data sets, such as the NIST condensed phase and fluid properties data sets,^[59b] as:

$$\begin{aligned} E^\circ_T &= -\Delta G^\circ(T = T_{\text{STEP}})/nF; E^\circ_{\text{ambient}} \equiv E^\circ_T(T_{\text{ambient}}); \text{ here} \\ T_{\text{ambient}} &= 298.15 \text{ K} = 25^\circ\text{C}, \text{ and:} \\ \Delta G^\circ(T = T_{\text{STEP}}) &= \sum_{i=1}^y c_i (H^\circ(C_i, T) - TS^\circ(C_i, T)) \\ &\quad - \sum_{i=1}^x r_i (H^\circ(R_i, T) - TS^\circ(R_i, T)) \end{aligned} \quad (3)$$

Compiled thermochemical data are often based on different reference states, while a consistent reference state is needed to

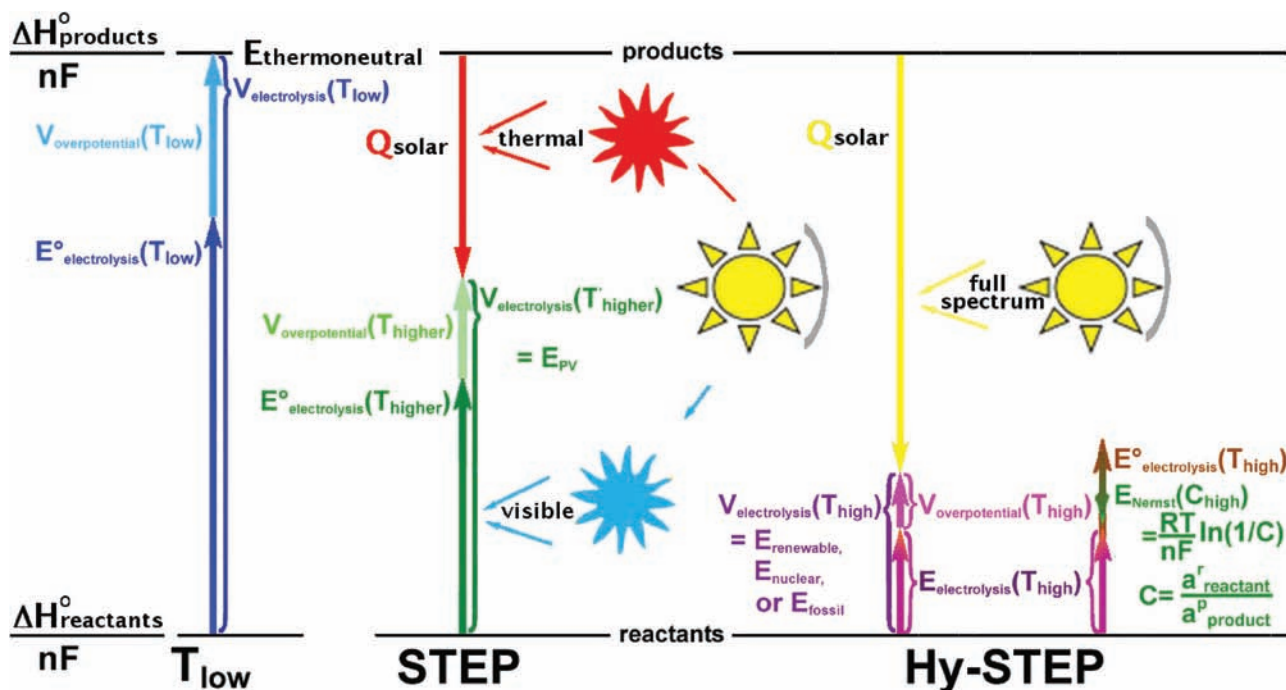
understand electrolysis limiting processes, including water.^[62,63] This challenge is overcome by modification of the unit activity ($a = 1$) consistent calculated electrolysis potential to determine the potential at other reagent and product relative activities via the Nernst equation.^[64,65] Electrolysis provides control of the relative amounts of reactant and generated product in a system. A substantial activity differential can also drive STEP improvement at elevated temperature, and will be derived. The potential variation with activity, a , of the Equation 2 reaction is given by: $\sum_{i=1}^x r_i R_i \rightarrow \sum_{i=1}^y c_i C_i$, is given by:

$$E_{T,a} = E^\circ_T - (RT/nF) \cdot \ln(\prod_{i=1}^x a(R_i)^{r_i} / \prod_{i=1}^y a(C_i)^{c_i}) \quad (4)$$

Electrolysis systems with a negative isothermal temperature coefficient tend to cool as the electrolysis products are generated. Specifically in endothermic electrolytic processes, the Equation 4 free-energy electrolysis potential, E_T , is less than the enthalpy based potential. This latter value is the potential at which the system temperature would remain constant during electrolysis. This thermoneutral potential, E_{tn} , is given by:

$$\begin{aligned} E_{\text{tn}}(T_{\text{STEP}}) &= -\Delta H(T)/nF; \Delta H(T_{\text{STEP}}) \\ &= \sum_{i=1}^y c_i H(C_i, T_{\text{STEP}}) - \sum_{i=1}^x r_i H(R_i, T_{\text{STEP}}) \end{aligned} \quad (5)$$

Two general STEP implementations are being explored. Both can provide the thermoneutral energy to sustain a variety of electrolyses. The thermoneutral potential, determined from the enthalpy of a reaction, describes the energy required to sustain an electrochemical process without cooling. For example, the thermoneutral potential we have calculated and reported for CO₂ splitting to CO and O₂ at unit activities, from Equation 5, is 1.46(±0.01) V over the temperature range of 25–1400 °C. As represented in Scheme 3 on the left, the standard electrolysis



Scheme 3. Comparison of solar energy utilization in STEP and Hy-STEP implementations of the solar thermal electrochemical production of energetic molecules.

potential at room temperature, E° , can comprise a significant fraction of the thermoneutral potential. The first STEP mode, energetically represented next to the room temperature process in the scheme, separates sunlight into thermal and visible radiation. The solar visible generates electronic charge which drives electrolysis charge transfer. The solar thermal component heats the electrolysis and decreases both the E° at this higher T , and the overpotential. The second mode, termed Hy-STEP (on the right) from “hybrid-STEP”, does not separate sunlight, and instead directs all sunlight to heating the electrolysis, generating the highest T and smallest E , while the electrical energy for electrolysis is generated by a separate source (such as by photovoltaic, solar thermal electric, wind turbine, hydro, nuclear or fossil fuel generated electronic charge). As shown on the right side, high relative concentrations of the electrolysis reactant (such as CO_2 or iron oxide will further decrease the electrolysis potential).

2.2. STEP Solar to Chemical Energy Conversion Efficiency

The Hy-STEP mode is being studied outdoors with either wind or solar CPV (concentrator photovoltaic) generated electricity to drive $E_{\text{electrolysis}}$. The STEP mode is experimentally more complex and is presently studied indoors under solar simulator illumination. Determination of the efficiency of Hy-STEP with solar electric is straightforward in the domain in which $E_{\text{electrolysis}} < E_{\text{thermoneutral}}$ and the coulombic efficiency is high. Solar thermal energy is collected at an efficiency of η_{thermal} to decrease the energy from $E_{\text{thermoneutral}}$ to $E_{\text{electrolysis}}$, and then electrolysis is driven at a solar electric energy efficiency of $\eta_{\text{solar-electric}}$:

$$\eta_{\text{Hy-STEPsolar}} = (\eta_{\text{thermal}}(E_{\text{thermoneutral}} - E_{\text{electrolysis}}) + \eta_{\text{solar-electric}} E_{\text{electrolysis}}) / E_{\text{thermoneutral}} \quad (6)$$

η_{thermal} is higher than $\eta_{\text{solar-electric}}$, and gains in efficiency occur in Equation 6 in the limit as $E_{\text{electrolysis}}$ approaches 0. $E_{\text{electrolysis}} = 0$ is equivalent to thermochemical, rather than electrolytic, production. As seen in Figure 1, at unit activity $F^{\text{CO}_2/\text{CO}}$ does not approach 0 until 3000 °C. Material constraints inhibit approach to this higher temperature, while electrolysis not only permits lower temperature, but also provides the advantage of spontaneous product separation. At lower temperature, small values of $E_{\text{electrolysis}}$ can occur at higher reactant and lower product activities, as described in Equation 4. In the present configuration sunlight is concentrated at 75% solar to thermal efficiency, heating the electrolysis to 950 °C, which decreases the high current density CO_2 splitting potential to 0.9V, and the electrolysis charge is provided by CPV at 37% solar to electric efficiency. The solar to chemical energy conversion efficiency is in accordance with Equation 6:

$$\eta_{\text{Hy-STEPsolar}} = (75\%(1.46\text{V} - 0.90\text{V}) + 37\% \cdot 0.90\text{V}) / 1.46\text{V} = 52\% \quad (7)$$

A relatively high concentration of reactants lowers the voltage of electrolysis via the Nernst term in Equation 4. With appropriate choice of high temperature electrolyte, this effect can be dramatic, for example both in STEP iron and in comparing the

benefits of the molten carbonate to solid oxide (gas phase) reactants for STEP CO_2 electrolytic reduction, sequestration and fuel formation. Fe(III) (as found in the common iron ore, hematite) is nearly insoluble in sodium carbonate, while it is soluble to over 10 m (molal) in lithium carbonate,^[6] and as discussed in Section 2.3, molten carbonate electrolyzer provides 10^3 to 10^6 times higher concentration of reactant at the cathode surface than a solid oxide electrolyzer.

In practice, for STEP iron or carbon capture, we simultaneously drive lithium carbonate electrolysis cells together in series, at the CPV maximum power point (Figure 2). Specifically, a Spectrolab CDO-100-C1MJ concentrator solar cell is used to generate 2.7 V at maximum power point, with solar to electrical energy efficiencies of 37% under 500 suns illumination. As seen in Figure 2, at maximum power, the 0.99 cm² cell generates 1.3 A at 100 suns, and when masked to 0.2 cm² area generates 1.4 A at 500 suns. Electrolysis electrode surface areas were chosen to match the solar cell generated power. At 950 °C at 0.9V, the electrolysis cells generate carbon monoxide at 1.3 to 1.5 A (the electrolysis current stability is shown at the bottom of Figure 2).

In accord with Equation 6 and Scheme 3, Hy-STEP efficiency improves with temperature increase to decrease overpotential and $E_{\text{electrolysis}}$, and with increase in the relative reactant activity. Higher solar efficiencies will be expected, both with more effective carbonate electrocatalysts (as morphologies with higher effective surface area and lower overpotential) are developed, and as also as PV efficiencies increase. Increases in solar to electric (both PV, CPV and solar thermal-electric) efficiencies continue to be reported, and will improve Equation 7 efficiency. For example, multijunction CPV have been reported improved to $\eta_{\text{PV}} = 40.7\%$.^[69]

Engineering refinements will improve some aspects, and decrease other aspects, of the system efficiency. Preheating the CO_2 , by circulating it as a coolant under the CPV (as we currently do in the indoor STEP experiment, but not outdoor, Hy-STEP experiments) will improve the system efficiency. In the present configuration outgoing CO and O_2 gases at the cathode and anode heat the incoming CO_2 . Isolation of the electrolysis products will require heat exchangers with accompanying radiative heat losses, and for electrolyses in which there are side reactions or product recombination losses, $\eta_{\text{Hy-STEP solar}}$ will decrease proportional to the decrease in coulombic efficiency. At present, wind turbine generated electricity is more cost effective than solar-electric, and we have demonstrated a Hy-STEP process with wind-electric, for CO_2 free production of iron (delineated in Section 3.3). Addition of long-term (overnight) molten salt insulated storage will permit continuous operation of the STEP process. Both STEP implementations provide a basis for practical, high solar efficiencies.

Components for STEP CO_2 capture and conversion to solid carbon are represented on the left side of Figure 2, and are detailed in references [4–7]. A 2.7 V CPV photopotential drives three in series electrolyses at 950°C. Fundamental details of the heat balance are provided in reference 4. The CPV has an experimental solar efficiency of 37%, and the 63% of insolation not converted to electricity comprises a significant heat source. The challenge is to direct a substantial fraction of this heat to the electrolysis. An example of this challenge is in the first stage of

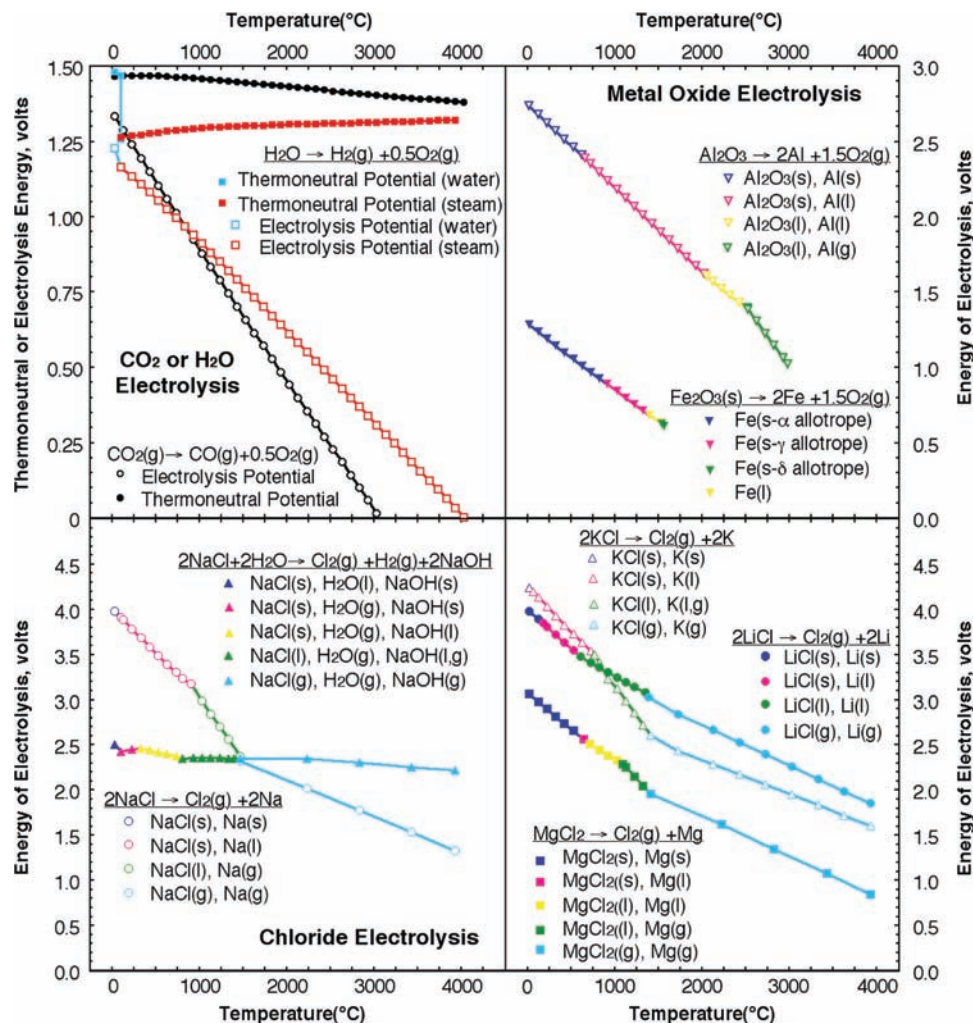


Figure 1. The calculated potential to electrolyze selected oxides (top) and chlorides (bottom). The indicated decrease in electrolysis energy, with increase in temperature, provides energy savings in the STEP process in which high temperature is provided by excess solar heat. Energies of electrolysis are calculated from Equation 3, with consistent thermochemical values at unit activity using NIST gas and condensed phase Shomate equations.^[55b] Note with water excluded, the chloride electrolysis decreases (in the lower left of the figure). All other indicated electrolysis potentials, including that of water or carbon dioxide, decrease with increasing temperature. Thermoneutral potentials are calculated with Equation 5. Modified with permission from [3].

heating, in which higher temperatures increases CO₂ preheat, but diminishes the CPV power. Heating of the reactant CO₂ is a three tier process in the current configuration: the preheating of room temperature CO₂ consists of either (1a) flow-through a heat exchange fixed to the back of the concentrator solar cell and/or (1b) preheating to simulate CO₂ extracted from an available heat source such as a hot smoke (flue) stack, (2) secondary heating consists of passing this CO₂ through a heat exchange with the outgoing products, (3) tertiary heat is applied through concentrated, split solar thermal energy (Figure 2).

An upper limit to the energy required to maintain a constant system temperature is given in the case in which neither solar IR, excess solar visible, nor heat exchange from the environment or products would be applied to the system. When an 0.90 V electrolysis occurs, an additional 0.56 V, over $E_{tn} = 1.46$ V, is required to maintain a constant system temperature. Hence, in the case of three electrolyses in series, as in Figure 2, an additional 3×0.56 V = 1.68 V will maintain

constant temperature. This is less than the 63% of the solar energy (equivalent to 4.6 V) not used in generating the 2.7 V of maximum power point voltage of electronic charge from the CPV in this experiment. Heating requirements are even less, when the reactant activity is maintained at a level that is higher than the product activity. For example, this is accomplished when products are continuously removed to ensure that the partial pressure of the products is lower than that of the CO₂. This lowers the total heat required for temperature neutrality to below that of the unit activity thermoneutral potential 1.46 V.

The STEP effective solar energy conversion efficiency, η_{STEP} , is constrained by both photovoltaic and thermal boost conversion efficiencies, η_{PV} and $\eta_{thermal-boost}$.^[8] Here, the CPV sustains a conversion efficiency of $\eta_{PV} = 37.0\%$. In the system, passage of electrolysis current requires an additional, combined (ohmic, anodic, and cathodic over-) potential above the thermodynamic potential. However, mobility and kinetics improve at higher temperature to decrease this overpotential. The generated CO

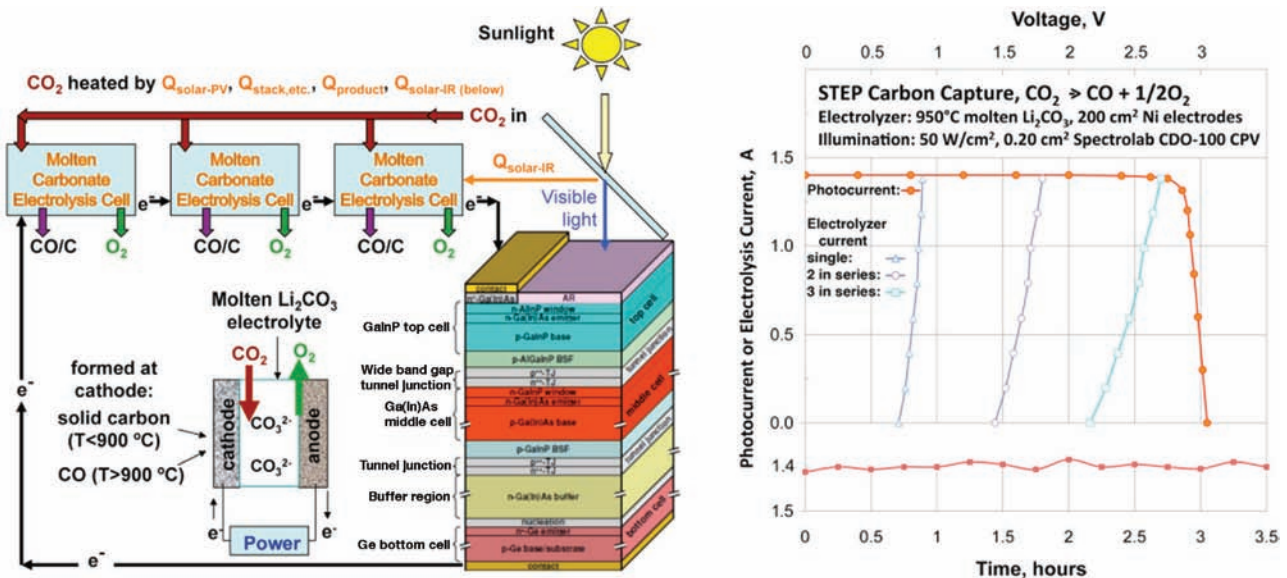


Figure 2. Left: STEP carbon capture in which three molten carbonate electrolysis in series are driven by a concentrator photovoltaic. Sunlight is split into two spectral regions; visible drives the CPV and thermal heats the electrolysis cell. In Hy-STEP (not shown) sunlight is not split and the full spectrum heats the electrolysis cell, and electronic charge is generated separately by solar, wind, or other source. Right: The maximum power point photovoltage of one Spectrolab CPV is sufficient to drive three in series carbon dioxide splitting 950 °C molten Li_2CO_3 electrolysis cells. Top: Photocurrent at 500 suns (masked (0.20 cm^2) Spectrolab CDO-100 CPV, or electrolysis current, versus voltage; electrolysis current is shown of one, two or three series 950 °C Li_2CO_3 electrolysis cells with 200 cm^2 Ni electrodes. Three in series electrolysis cells provide a power match at the 2.7 V maximum power point of the CPV at 950 °C; similarly (not shown), two 750 °C Li_2CO_3 electrolysis cells in series provide a power match at 2.7V to the CPV. Bottom: Stable carbon capture (with 200 cm^2 “aged” Ni electrodes at 750 °C; fresh electrodes (not shown) exhibit an initial fluctuation as carbon forms at the cathode and Ni oxide layer forms on the anode. The rate of solid carbon deposition gradually increases as the cathode surface area slowly increases in time. Modified with permission from [4].

contains an increase in oxidation potential compared to carbon dioxide at room temperature ($E_{\text{CO}_2/\text{CO}}(25\text{ °C}) = 1.33\text{ V}$ for $\text{CO}_2 \rightarrow \text{CO} + 1/2\text{O}_2$ in Figure 1), an increase of 0.43 V compared to the 0.90 V used to generate the CO. The electrolysis efficiency compares the stored potential to the applied potential, $\eta_{\text{thermal-boost}} = E^{\circ}_{\text{electrolysis}}(25\text{ °C})/V_{\text{electrolysis}}(T)$.^[4] Given a stable temperature electrolysis environment, the experimental STEP solar to CO carbon capture and conversion efficiency is the product of this relative gain in energy and the electronic solar efficiency:

$$\eta_{\text{STEP}} = \eta_{\text{PV}} \cdot \eta_{\text{thermal-boost}} = 37.0\% \cdot (1.33\text{ V}/0.90\text{ V}) = 54.7\% \quad (8)$$

Ohmic and overpotential losses are already included in the measured electrolysis potential. This 54.7% STEP solar conversion efficiency is an upper limit of the present experiment, and as with the Hy-STEP mode, improvements are expected in electrocatalysis and CPV efficiency. Additional losses will occur when beam splitter and secondary concentrator optics losses, and thermal systems matching are incorporated, but serves to demonstrate the synergy of this solar/photo/electrochemical/thermal process, leads to energy efficiency higher than that for solar generated electricity,^[69] or for photochemical,^[70] photoelectrochemical,^[21,27] solar thermal,^[71] or other CO_2 reduction processes.^[72]

The CPV does not need, nor function with, sunlight of energy less than that of the 0.67 eV bandgap of the multi-junction Ge bottom layer. From our previous calculations, this thermal energy comprises 10% of AM1.5 insolation, which will be further diminished by the solar thermal absorption efficiency

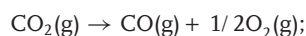
and heat exchange to the electrolysis efficiency,^[54] and under 0.5 MW m^{-2} of incident sunlight (500 suns illumination), yields $\sim 50\text{ kW m}^{-2}$, which may be split off as thermal energy towards heating the electrolysis cell without decreasing the CPV electronic power. The CPV, while efficient, utilizes less than half of the super-bandgap ($h\nu > 0.67\text{ eV}$) sunlight. A portion of this $> \sim 250\text{ kW m}^{-2}$ available energy, is extracted through heat exchange at the backside of the CPV. Another useful source for consideration as supplemental heat is industrial exhaust. The temperature of industrial flue stacks varies widely, with fossil fuel source and application, and ranges up to 650 °C for an open circuit gas turbine. The efficiency of thermal energy transfer will limit use of this available heat.

A lower limit to the STEP efficiency is determined when no heat is recovered, either from the CPV or remaining solar IR, and when heat is not recovered via heat exchange from the electrolysis products, and when an external heat source is used to maintain a constant electrolysis temperature. In this case, the difference between the electrolysis potential and the thermoneutral potential represents the enthalpy required to keep the system from cooling. In this case, our 0.9 V electrolysis occurs at an efficiency of $(0.90\text{ V}/1.46\text{ V}) \cdot 54.7\% = 34\%$. While the STEP energy analysis, detailed in Section 4.2 for example for CO_2 to CO splitting, is more complex than that of the Hy-STEP mode, more solar thermal energy is available including a PV's unused or waste heat to drive the process and to improve the solar to chemical energy conversion efficiency. We determine the STEP solar efficiency over the range from inclusion of no solar

thermal heat (based on the enthalpy, rather than free energy, of reaction) to the case where the solar thermal heat is sufficient to sustain the reaction (based on the free energy of reaction). This determines the efficiency range, as chemical flow out to the solar flow in (as measured by the increase in chemical energy of the products compared to the reactants), from 34% to over 50%.

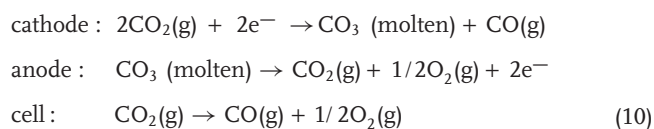
2.3. Identification of STEP Consistent Endothermic Processes

The electrochemical driving force for a variety of chemicals of widespread use by society will be shown to significantly decrease with increasing temperature. As calculated and summarized in the top left of Figure 1, the electrochemical driving force for electrolysis of either carbon dioxide or water, significantly decreases with increasing temperature. The ability to remove CO₂ from exhaust stacks or atmospheric sources, provides a response to linked environmental impacts, including global warming due to anthropogenic CO₂ emission. From the known thermochemical data for CO₂, CO and O₂, and in accord with Equation 1, CO₂ splitting can be described by:



$$E^\circ_{\text{CO}_2\text{split}} = (\text{G}^\circ_{\text{CO}} + 0.5\text{G}^\circ_{\text{O}_2} - \text{G}^\circ_{\text{CO}_2})/2F; E^\circ(25^\circ\text{C}) = 1.333 \text{ V} \quad (9)$$

As an example of the solar energy efficiency gains, this progress report focuses on CO₂ splitting potentials, and provides examples of other useful STEP processes. As seen in Figure 1, CO₂ splitting potentials decrease more rapidly with temperature than those for water splitting, signifying that the STEP process may be readily applied to CO₂ electrolysis. Efficient, renewable, non-fossil fuel energy rich carbon sources are needed, and the product of Equation 9, carbon monoxide is a significant industrial gas with a myriad of uses, including the bulk manufacturing of hydrocarbon fuels, acetic acid and aldehydes (and detergent precursors), and for use in industrial nickel purification.^[66] To alleviate challenges of fossil-fuel resource depletion, CO is an important syngas component and methanol is formed through the reaction with H₂. The ability to remove CO₂ from exhaust stacks or atmospheric sources, also limits CO₂ emission. Based on our original analogous experimental photo-thermal electrochemical water electrolysis design,^[55] the first CO₂ STEP process consists of solar driven and solar thermal assisted CO₂ electrolysis. In particular, in a molten carbonate bath electrolysis cell, fed by CO₂.

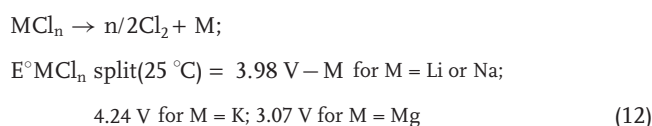


Molten alkali carbonate electrolyte fuel cells typically operate at 650 °C. Li, Na or K cation variation can affect charge mobility and operational temperatures. Sintered nickel often serves as the anode, porous lithium doped nickel oxide often as the cathode, while the electrolyte is suspended in a porous, insulating, chemically inert LiAlO₂ ceramic matrix.^[67]

Solar thermal energy can be used to favor the formation of products for electrolyses characterized by a negative isothermal temperature coefficient, but will not improve the efficiency of heat neutral or exothermic reactions. An example of this restriction occurs for the electrolysis reaction currently used by industry to generate chlorine. During 2008, the generation of chlorine gas (principally for use as bleach and in the chlor-alkali industry) consumed approximately 1% of the world's electricity,^[68] prepared in accord with the industrial electrolytic process:



In the lower left portion of Figure 1, the calculated electrolysis potential for this industrial chlor-alkali reaction exhibits little variation with temperature, and hence the conventional generation of chlorine by electrolysis would not benefit from the inclusion of solar heating. This potential is relatively invariant, despite a number of phase changes of the components (indicated on the figure and which include the melting of NaOH or NaCl). However, as seen in the figure, the calculated potential for the anhydrous electrolysis of chloride salts is endothermic, including the electrolyses to generate not only chlorine, but also metallic lithium, sodium and magnesium, and can be greatly improved through the STEP process:



The calculated decrease for the anhydrous chloride electrolysis potentials are on the order of volts per 1000 °C temperature change. For example, from 25 °C up to the MgCl₂ boiling point of 1412 °C, the MgCl₂ electrolysis potential decreases from 3.07 V to 1.86 V. This decrease provides a theoretical basis for significant, non CO₂ emitting, non-fossil fuel consuming processes for the generation of chlorine and magnesium, to be delineated in Section 3.4, and occurring at high solar efficiency analogous to the similar CO₂ STEP process.

In Section 3.2 the STEP process will be derived for the efficient solar removal/ recycling of CO₂. In addition, thermodynamic calculation of metal and chloride electrolysis rest potentials identifies electrolytic processes which are consistent with endothermic processes for the formation of iron, chlorine, aluminum, lithium, sodium and magnesium, via CO₂-free pathways. As shown, the conversion and replacement of the conventional, aqueous, industrial alkali-chlor process, with an anhydrous electrosynthesis, results in a redox potential with a calculated decrease of 1.1 V from 25 to 1000 °C.

As seen in the top right of Figure 1, the calculated electrochemical reduction of metal oxides can exhibit a sharp, smooth decrease in redox potential over a wide range of phase changes. These endothermic process provide an opportunity for the replacement of conventional industrial processes by the STEP formation of these metals. In 2008, industrial electrolytic processes consumed ~5% of the world's electricity, including for aluminum (3%), chlorine (1%), and lithium, magnesium and sodium production. This 5% of the global 19 × 10¹² kWh of electrical production, is equivalent to the emission

of 6×10^8 metric tons of CO_2 .^[68] The iron and steel industry accounts for a quarter of industrial direct CO_2 emissions. Currently, iron is predominantly formed through the reduction of hematite with carbon, emitting CO_2 :



A non- CO_2 emitting alternative is provided by the STEP driven electrolysis of Fe_2O_3 :



As seen in the top right of Figure 1, the calculated iron generating electrolysis potentials drops 0.5 V (a 38% drop) from 25 °C to 1000 °C, and as with the CO_2 analogue, will be expected to decrease more rapidly with high iron oxide activity conditions. Conventional industrial processes for these metals and chlorine, along with CO_2 emitted from power and transportation, are responsible for the majority of anthropogenic CO_2 release. The STEP process, to efficiently recover carbon dioxide and in lieu of these industrial processes, can provide a transition beyond the fossil fuel-electric grid economy.

The top left of Figure 1 includes calculated thermoneutral potentials for CO_2 and water splitting reactions. At ambient temperature, the difference between E_{th} and E_{T} does not indicate an additional heat requirement for electrolysis, as this heat is available via heat exchange with the ambient environment. At ambient temperature, $E_{\text{th}} - E_{\text{T}}$ for CO_2 or water is respectively 0.13 and 0.25 V, is calculated (not shown) as 0.15 ± 0.1 V for Al_2O_3 and Fe_2O_3 , and 0.28 ± 0.3 V for each of the chlorides.

We find that molten electrolytes present several fundamental advantages compared to solid oxides for CO_2 electrolysis. (i) Molten carbonate electrolyzer provides 10^3 to 10^6 times higher concentration of reactant at the cathode surface than a solid oxide electrolyzer. Solid oxides utilize gas phase reactants, whereas carbonates utilize molten phase reactants. Molten carbonate contains 2×10^{-2} mol reducible tetravalent carbon/ cm^3 . The density of reducible tetravalent carbon sites in the gas phase is considerably lower. Air contains 0.03% CO_2 , equivalent to only 1×10^{-8} mol of tetravalent carbon/ cm^3 , and flue gas (typically) contains 10-15% CO_2 , equivalent to 2×10^{-5} mol reducible C(IV)/ cm^3 . Carbonate's higher concentration of active, reducible tetravalent carbon sites, logarithmically decreases the electrolysis potential, and can facilitate charge transfer at low electrolysis potentials. (ii) Molten carbonates can directly absorb atmospheric CO_2 , whereas solid oxides require an energy consuming pre-concentration process. (iii) Molten carbonates electrolyses are compatible with both solid and gas phase products. (iv) Molten processes have an intrinsic thermal buffer not found in gas phase systems. Sunlight intensity varies over a 24-hour cycle, and more frequently with variations in cloud cover. This disruption to other solar energy conversion processes is not necessary in

molten salt processes. For example as discussed in Section 4.3, the thermal buffer capacity of molten salts has been effective for solar to electric power towers to operate 24/7. These towers concentrate solar thermal energy to heat molten salts, which circulate and via heat exchange boil water to drive conventional mechanical turbines.

3. Demonstrated STEP Processes

3.1. STEP Hydrogen

STEP occurs at both higher electrolysis and higher solar conversion efficiencies than conventional room temperature photovoltaic (PV) generation of hydrogen. Experimentally, we demonstrated a sharp decrease in the water splitting potential in an unusual molten sodium hydroxide medium, Figure 3, and as shown in Figure 4, three series connected Si CPVs efficiently driving two series molten hydroxide water splitting cells at 500 °C to generate hydrogen.^[55]

Recently we have considered the economic viability of solar hydrogen fuel production. That study provided evidence that the STEP system is an economically viable solution for the production of hydrogen.^[55]

3.2. STEP Carbon Capture

In this process carbon dioxide is captured directly, without the need to pre-concentrate dilute CO_2 , using a high temperature electrolysis cell powered by sunlight in a single step. Solar thermal energy decreases the energy required for the endothermic

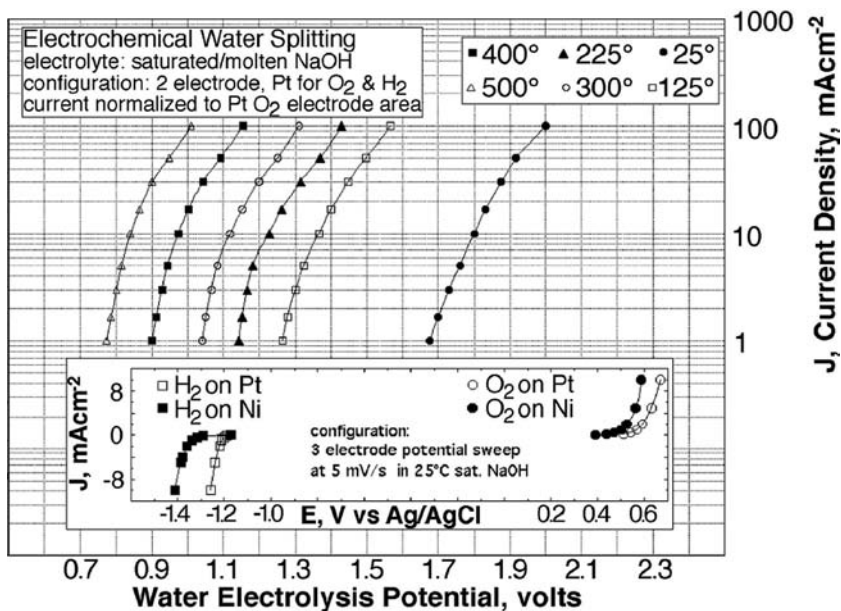


Figure 3. Water electrolysis potential, measured in aqueous saturated or molten NaOH, at 1 atm. Steam is injected in the molten electrolyte. The O_2 anode is 0.6 cm^2 Pt foil. IR and polarization losses are minimized by sandwiching 5 mm from each side of the anode, oversized Pt gauze cathode. Inset: At 25 °C, 3 electrode values comparing Ni and Pt working electrodes and with a Pt gauze counterelectrode at 5 mV/s.

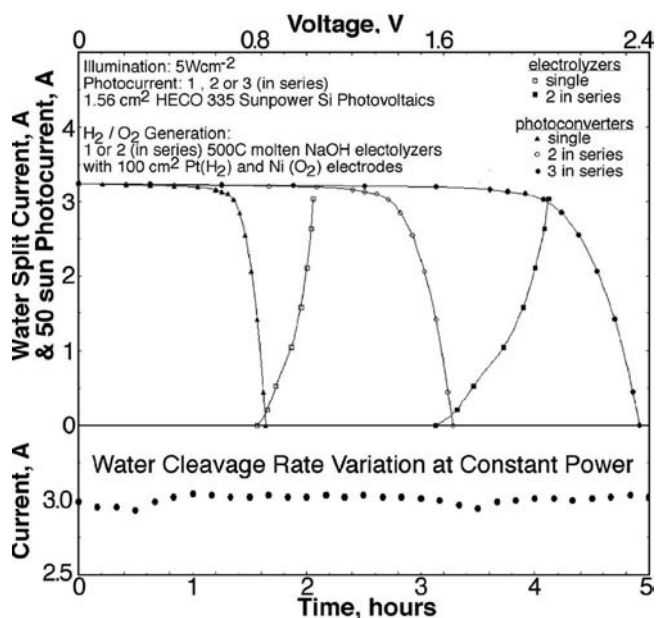


Figure 4. Photovoltaic and electrolysis charge transfer of STEP hydrogen using Si CPV's driving molten NaOH water electrolysis. The photocurrent is shown for 1, 2, or 3 1.561 cm² HECO 335 Sunpower Si photovoltaics in series at 50 suns. The CPVs drive 500 °C molten NaOH steam electrolysis using Pt gauze electrodes. Left inset: electrolysis current stability.

conversion of carbon dioxide and kinetically facilitates electrochemical reduction, while solar visible generates electronic charge to drive the electrolysis. CO₂ can be captured as solid

carbon and stored, or used as carbon monoxide to feed chemical or synthetic fuel production. Thermodynamic calculations are used to determine, and then demonstrate, a specific low energy, molten carbonate salt pathway for carbon capture.

Prior investigations of the electrochemistry of carbonates in molten salts tended to focus on reactions of interest to fuel cells,^[67] rather than the (reverse) electrolysis reactions of relevance to the STEP reduction of carbon dioxide, typically in alkali carbonate mixtures. Such mixtures substantially lower the melting point compared to the pure salts, and would provide the thermodynamic maximum voltage for fuel cells. However, the electrolysis process is maximized in the opposite temperature domain of fuel cells, that is at elevated temperatures which decrease the energy of electrolysis, as schematically delineated in Scheme 1. These conditions provide a new opportunity for effective CO₂ capture.

CO₂ electrolysis splitting potentials are calculated from the thermodynamic free energy components of the reactants and products^[3,4,59b] as $E = -\Delta G(\text{reaction})/nF$, where $n = 4$ or 2 for the respective conversion of CO₂ to the solid carbon or carbon monoxide products. As calculated using the available thermochemical enthalpy and entropy of the starting components, and as summarized in the left side of **Figure 5**, molten Li₂CO₃, via a Li₂O intermediate, provides a preferred, low energy route compared to Na₂CO₃ or K₂CO₃ (via Na₂O or K₂O), for the conversion of CO₂. High temperature is advantageous as it decreases the free energy necessary to drive the STEP endothermic process. The carbonates, Li₂CO₃, Na₂CO₃ and K₂CO₃, have respective melting points of 723, 851, and 891 °C. Molten Li₂CO₃ not only requires lower thermodynamic electrolysis energy, but in addition has higher conductivity

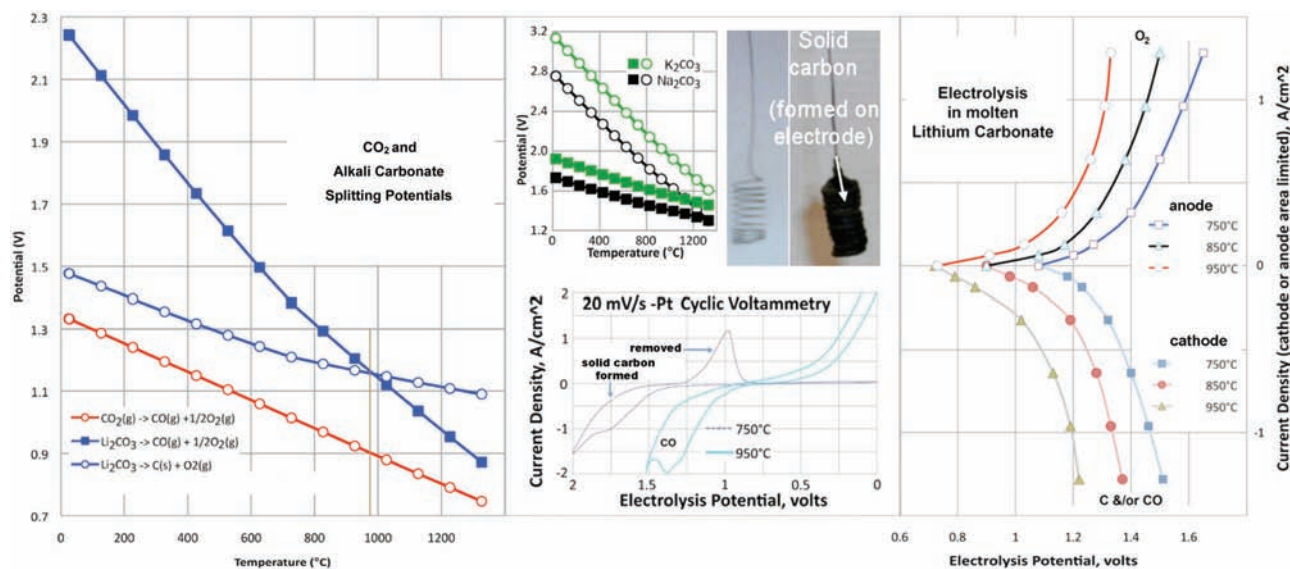
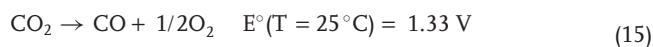


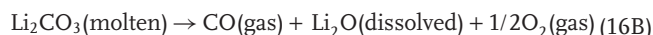
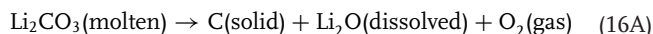
Figure 5. The calculated (left) and measured (right) electrolysis of CO₂ in molten carbonate. Left: The calculated thermodynamic electrolysis potential for carbon capture and conversion in Li₂CO₃ (main figure), or Na₂CO₃ or K₂CO₃ (left middle); squares refer to M₂CO₃ → C + M₂O + O₂ and circles to a M₂CO₃ → CO + M₂O + 1/2 O₂. To the left of the vertical brown line, solid carbon is the thermodynamically preferred (lower energy) product. To the right of the vertical line, CO is preferred. Carbon dioxide fed into the electrolysis chamber is converted to solid carbon in a single step. Photographs: coiled platinum cathode before (left), and after (right), CO₂ splitting to solid carbon at 750 °C in molten carbonate with a Ni anode. Right: The electrolysis full cell potential is measured, under anode or cathode limiting conditions, at a platinum electrode for a range of stable anodic and cathodic current densities in molten Li₂CO₃. Lower middle: cathode size restricted full cell cyclic voltammetry, CV, of Pt electrodes in molten Li₂CO₃. Modified with permission from [4].

(6 S cm⁻¹) than that of Na₂CO₃ (3 S cm⁻¹) or K₂CO₃ (2 S cm⁻¹) near the melting point.^[73] Higher conductivity is desired as it leads to lower electrolysis ohmic losses. Low carbonate melting points are achieved by a eutectic mix of alkali carbonates (T_{mp}, Li_{1.07}Na_{0.93}CO₃: 499 °C; Li_{0.85}Na_{0.61}K_{0.54}CO₃: 393°C). Mass transport is also improved at higher temperature; the conductivity increases from 0.9 to 2.1 S cm⁻¹ with temperature increase from 650 to 875 °C for a 1:1:1 by mass mixture of the three alkali carbonates.^[74]

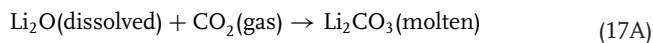
In 2009 we showed that molten carbonate electrolyzers can provide an effective media for solar splitting of CO₂ at high conversion efficiency. In 2010 Lubormirsky, et al, and our group separately reported that molten lithiated carbonates provide a particularly effective medium for the electrolysis reduction of carbon dioxide.^[4,75] As we show in the photograph in Figure 5, at 750 °C, carbon dioxide is captured in molten lithium carbonate electrolyte as solid carbon by reduction at the cathode at low electrolysis potential. It is seen in the cyclic voltammetry, CV, that a solid carbon peak that is observed at 750 °C is not evident at 950 °C. At temperatures less than ~900 °C in the molten electrolyte, solid carbon is the preferred CO₂ splitting product, while carbon monoxide is the preferred product at higher temperature. As seen in the main portion of the figure, the electrolysis potential is <1.2V at either 0.1 or 0.5 A/cm², respectively at 750 or 850 °C. Hence, the electrolysis energy required at these elevated, molten temperatures is less than the minimum energy required to split CO₂ to CO at 25 °C:



The observed experimental carbon capture correlates with:

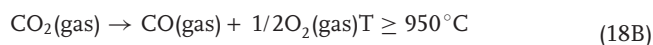
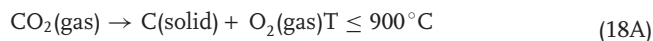


When CO₂ is bubbled in, a rapid reaction back to the original lithium carbonate is strongly favored:



In the presence of carbon dioxide, reaction 17A is strongly favored (exothermic), and the rapid reaction back to the original lithium carbonate occurs while CO₂ is bubbled into molten lithium carbonate containing the lithium oxide.

The carbon capture reaction in molten carbonate, combines Equations 16 and 17:



The electrolysis of carbon capture in molten carbonates can occur at lower experimental electrolysis potentials than the unit activity potentials calculated in Figure 5. A constant influx of carbon dioxide to the cell maintains a low concentration of Li₂O, in accord with reaction 23. The activity ratio, Θ , of the carbonate reactant to the oxide product in the electrolysis chamber, when

high, decreases the cell potentials with the Nernst concentration variation of the potential in accord with Equation 16, as:

$$E_{\text{CO}_2/X}(T) = E_{\text{CO}_2/X}^\circ(T) - 0.0592 \text{ V} \cdot T(K) / (n \cdot 298 \text{ K}) \cdot \log(\Theta);$$

$$n = 4 \text{ or } 2, \text{ for } X = \text{C}_{\text{solid}} \text{ or } \text{CO}_{\text{product}} \quad (19)$$

For example from Equation 19, the expected cell potential at 950 °C for the reduction to the CO product is $E_{\text{CO}_2/\text{CO}} = 1.17 \text{ V} (0.243/2) \cdot 4 = 0.68 \text{ V}$, with a high $\Theta = 10\,000$ carbonate/oxide ratio in the electrolysis chamber. As seen in the Figure 5 photo, CO₂ is captured in 750 °C Li₂CO₃ as solid carbon by reduction at the cathode at low electrolysis potential. The carbon formed in the electrolysis in molten Li₂CO₃ at 750 °C is in quantitative accord with the 4 e⁻ reduction of Equation 16A, as determined by (i) mass, at constant 1.25 A for both 0.05 and 0.5 A/cm² (large and small electrode) electrolyses (the carbon is washed in a sonicator, and dried at 90 °C), by (ii) ignition (furnace combustion at 950 °C) and by (iii) volumetric analysis in which KIO₃ is added to the carbon, converted to CO₂ and I₂ in hot phosphoric acid (5C + 4KIO₃ + 4H₃PO₄ → 5CO₂ + 2I₂ + 2H₂O + 4KH₂PO₄), the liberated I₂ is dissolved in 0.05 M KI and titrated with thiosulfate using a starch indicator. We also observe the transition to the carbon monoxide product with increasing temperature. Specifically, while at 750 °C the molar ratio of solid carbon to CO-gas formed is 20:1, at 850° in molten Li₂CO₃, the product ratio is a 2:1, at 900 °C, the ratio is 0.5:1, and at 950 °C the gas is the sole product. Hence, in accord with Figure 2, switching between the C or CO product is temperature programmable.

We have replaced Pt, with Ni, nickel alloys (inconel and monel), Ti and carbon, and each are effective carbon capture cathode materials. Solid carbon deposits on each of these cathodes at similar overpotential in 750 °C molten Li₂CO₃. For the anode, both platinum and nickel are effective, while titanium corrodes under anodic bias in molten Li₂CO₃. As seen in the right side of Figure 5, electrolysis anodic overpotentials in Li₂CO₃ electrolysis are comparable, but larger than cathodic overpotentials, and current densities of over 1A cm⁻² can be sustained. Unlike other fuel cells, carbonate fuel cells are resistant to poisoning effects,^[67] and are effective with a wide range of fuels, and this appears to be the same for the case in the reverse mode (to capture carbon, rather than to generate electricity). Molten Li₂CO₃ remains transparent and sustains stable electrolysis currents after extended (hours/days) carbon capture over a wide range of electrolysis current densities and temperatures.

As delineated in Section 2.3, in practice, either STEP or Hy-STEP modes are useful for efficient solar carbon capture. CO₂ added to the cell is split at 50% solar to chemical energy conversion efficiency by series coupled lithium carbonate electrolysis cells driven at maximum power point by an efficient CPC. Experimentally, we observe the facile reaction of CO₂ and Li₂O in molten Li₂CO₃. We can also calculate the thermodynamic equilibrium conditions between the species in the system, Equation 3B. Using the known thermochemistry of Li₂O, CO₂ and Li₂CO₃,^[59b] we calculate the reaction free-energy of Equation 1, and from this calculate the thermodynamic equilibrium constant as a function of temperature. From this equilibrium constant, the area above the curve on the left side of

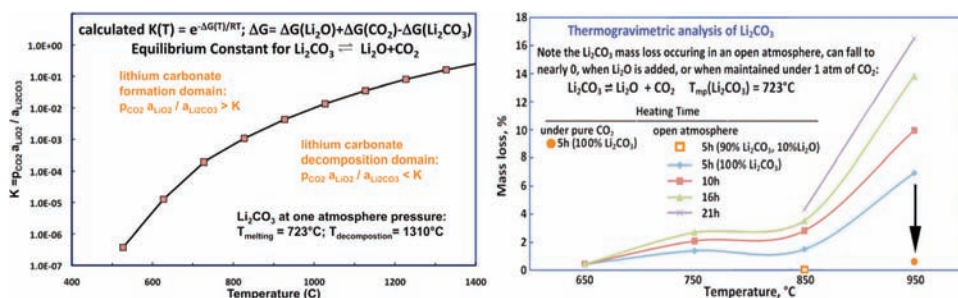


Figure 6. Left: Species stability in the lithium carbonate, lithium oxide, carbon dioxide system, as calculated from Li_2CO_3 , Li_2O , and CO_2 thermochemical data. Right: Thermogravimetric analysis of lithium carbonate. The measured mass loss in time of Li_2CO_3 . Not shown: The Li_2CO_3 mass loss rate also decreases with an increasing ratio of Li_2CO_3 mass to the surface area of the molten salt exposed to the atmosphere. This increased ratio, may increase the released partial pressure of CO_2 above the surface, increase the rate of the back reaction ($Li_2O + CO_2 \rightarrow Li_2CO_3$), and therefore result in the observed decreased mass loss. Hence, under an open atmosphere at $950^\circ C$, the mass loss after 5 hours falls from 7% to 4.7%, when the starting mass of pure Li_2CO_3 in the crucible is increased from 20 to 50 g. Under these latter conditions (open atmosphere, $950^\circ C$, 50 g total electrolyte), but using a 95% Li_2CO_3 , 5% Li_2O mix, the rate of mass loss is only 2.3%. Modified with permission from [8].

Figure 6 presents the wide domain (above the curve) in which Li_2CO_3 dominates, that is where excess CO_2 reacts with Li_2O such that $p_{CO_2} \cdot a_{Li_2O} < a_{Li_2CO_3}$. This is experimentally verified when we dissolve Li_2O in molten Li_2CO_3 , and inject CO_2 (gas). Through the measured mass gain, we observe the rapid reaction to Li_2CO_3 . Hence, CO_2 is flowed into a solution of 5% by weight Li_2O in molten Li_2CO_3 at $750^\circ C$, the rate of mass gain is only limited by the flow rate of CO_2 into the cell (using an Omega FMA 5508 mass flow controller) to react one equivalent of CO_2 per dissolved Li_2O . As seen in the measured thermogravimetric analysis on the right side of Figure 6, the mass loss in time is low in lithium carbonate heated in an open atmosphere ($\sim 0.03\% CO_2$) up to $850^\circ C$, but accelerates when heated to $950^\circ C$. However the $950^\circ C$ mass loss falls to nearly zero, when heated under pure (1 atm) CO_2 . Also in accord with Equation 1 added Li_2O shifts the equilibrium to the left. As seen in the figure in an open atmosphere, there is no mass loss in a 10% Li_2O , 90% Li_2CO_3 at $850^\circ C$, and the Li_2O containing electrolyte absorbs CO_2 (gains mass) at $750^\circ C$ to provide for the direct carbon capture of atmospheric CO_2 , without a CO_2 pre-concentration stage. This consists of the absorption of atmospheric CO_2 (in molten Li_2CO_3 containing Li_2O , to form Li_2CO_3), combined with a facile rate of CO_2 splitting due to the high carbonate concentration, compared to the atmospheric concentration of CO_2 , and the continuity of the steady-state of concentration Li_2O , as Li_2CO_3 is electrolyzed in Equation 16.

3.3. STEP of Iron

A fundamental change in the understanding of iron oxide thermochemistry, can open a facile, new CO_2 -free route to iron production. Along with the control of fire, iron production is one of the founding technological pillars of civilization, but is a major source of CO_2 emission. In industry, iron is still produced by the carbothermal greenhouse gas intensive reduction of iron oxide by carbon-coke, and a carbon dioxide free process to form this staple is needed.

The earliest attempt at electrowinning iron (the formation of iron by electrolysis) from carbonate appears to have been in 1944 in the unsuccessful attempt to electrodeposit iron from

a sodium carbonate, peroxide, metaborate mix at $450\text{--}500^\circ C$, which deposited sodium and magnetite (iron oxide), rather than iron.^[76,77] Other attempts^[77] have focused on iron electrodeposition from molten mixed halide electrolytes, which has not provided a successful route to form iron,^[78,79] or aqueous iron electrowinning^[80–83] that is hindered by the high thermodynamic potential ($E^\circ = 1.28 V$) and diminished kinetics at low temperature.

We present a novel route to generate iron metal by the electrolysis of dissolved iron oxide salts in molten carbonate electrolytes, unexpected due to the reported insolubility of iron oxide in carbonates. We report high solubility of lithiated iron oxides, and facile charge transfer that produces the staple iron at high rate and low electrolysis energy, and can be driven by conventional electrical sources, but is also demonstrated with STEP processes that decreases or eliminates a major global source of greenhouse gas emission.^[3,4]

As recently as 1999, the solubility of ferric oxide, Fe_2O_3 , in $650^\circ C$ molten carbonate was reported as very low, a $10^{-4.4}$ mole fraction in lithium/potassium carbonate mixtures, and was reported as invariant of the fraction of Li_2CO_3 and K_2CO_3 .^[84] Low solubility, of interest to the optimization of molten carbonate fuel cells, had likely discouraged research into the electrowinning of iron metal from ferric oxide in molten lithium carbonate. Rather than the prior part per million reported solubility, we find higher $Fe(III)$ solubilities, on the order of 50% in carbonates at $950^\circ C$. The CV of a molten Fe_2O_3 Li_2CO_3 mixture presented in **Figure 7**, and exhibits a reduction peak at $-0.8 V$, on Pt (gold curve); which is more pronounced at an iron electrode (light gold curve). At constant current, iron is clearly deposited. The cooled deposited product contains pure iron metal and trapped salt, and changes to rust color with exposure to water (figure photo). The net electrolysis is the redox reaction of ferric oxide to iron metal and O_2 , Equation 14. The deposit is washed, dried, and is observed to be reflective, grey metallic, responds to an external magnetic field, and consists of dendritic iron crystals.

The two principle natural ores of iron are hematite (Fe_2O_3) and the mixed valence $Fe^{2+/3+}$ magnetite (Fe_3O_4). We observe that, Fe_3O_4 is also highly soluble in molten Li_2CO_3 , and may also be reduced to iron with the net electrolysis reaction:

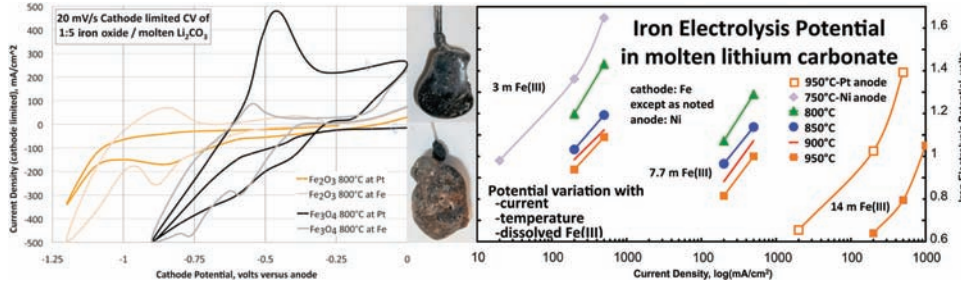


Figure 7. Middle: Photographs of electrolysis products from 20% Fe₂O₃ or Fe₃O₄ by mass in 800 °C Li₂CO₃: following extended 0.5A electrolysis at a coiled wire (Pt or Fe) cathode with a Ni anode. Left: cathode restricted CV in Li₂CO₃, containing 1:5 by weight of either Fe₂O₃ or Fe₃O₄. Right: The measured iron electrolysis potentials in molten Li₂CO₃, as a function of the temperature, current density, and the concentration of dissolved Fe(III). Modified with permission from [5].



Fe₃O₄ electrolysis potentials run parallel, but ~0.06 V higher, than those of Fe₂O₃ in Figure 1. The processes are each endothermic; the required electrolysis potential decreases with increasing temperature. For Fe₃O₄ in Figure 7, unlike the single peak evident for Fe₂O₃, two reduction peaks appear in the CV at 800 °C. Following the initial cathodic sweep (indicated by the left arrow), the CV exhibits two reduction peaks, again more pronounced at an iron electrode (grey curve), which appear to be consistent with the respective reductions of Fe²⁺ and Fe³⁺. In either Fe₂O₃, or Fe₃O₄, the reduction occurs at a potential before we observe any reduction of the molten Li₂CO₃ electrolyte, and at constant current, iron is deposited. Following 1 hour of electrolysis at either 200 or 20 mA/cm² of iron deposition, as seen in the Figure 7 photographs, and as with the Fe₂O₃ case, the extracted cooled electrode, following extended electrolysis and iron formation, contains trapped electrolyte. Following washing, the product weight is consistent with the eight electron per Fe₃O₄ coulombic reduction to iron.

The solid products of the solid reaction of Fe₂O₃ and Li₂CO₃ had been characterized.^[85,86] We prepare and probe the solubility of lithiated iron oxide salts in molten carbonates, and report high Fe(III) solubilities, on the order of 50% in molten carbonates, are achieved via the reaction of Li₂O with Fe₂O₃, yielding an effective method for CO₂ free iron production.

Lithium oxide, as well as Fe₂O₃ or Fe₃O₄, each have melting points above 1460 °C. Li₂O dissolves in 400–1000 °C molten carbonates. We find the solubility of Li₂O in molten Li₂CO₃ increases from 9 to 14 m from 750 to 950 °C. Following preparation of specific iron oxide salts, we add them to molten alkali carbonate. The resultant Fe(III) solubility is similar when either LiFeO₂, or LiFeO₂ as Fe₂O₃ + Li₂O, is added to the Li₂CO₃. As seen in the left side of Figure 8, the solubility of LiFeO₂ is over 12 m above 900 °C in Li₂CO₃.

The solid reaction of Fe₂O₃ and Na₂CO₃ produces both NaFeO₂ and NaFe₅O₈ products.^[87] As seen in Figure 8, unlike the high solubility of iron oxide in molten Li₂CO₃, Na₂CO₃ or K₂CO₃, exhibit <<1 wt% iron oxide solubility, even at 950 °C. However, the solubility of (Li₂O + Fe₂O₃) is high in the alkali carbonate eutectic, Li_{0.87}Na_{0.63}K_{0.50}CO₃, and is approximately proportional to the Li fraction in the pure Li₂CO₃ electrolyte. The solubility of this lithiated ferric oxide in the Li_xNa_yK_zCO₃ mixes provides an alternative molten media for iron production, which compared to pure lithium carbonate, has the disadvantage of lower conductivity,^[5] but the advantage of even greater availability, and a wider operating temperature domain range (extending several hundred degrees lower than the pure lithium system).

Fe₂O₃ or LiFe₅O₈ dissolves rapidly in molten Li₂CO₃, but reacts with the molten carbonate as evident in a mass loss, which evolves one equivalent of CO₂ per Fe₂O₃, to form a

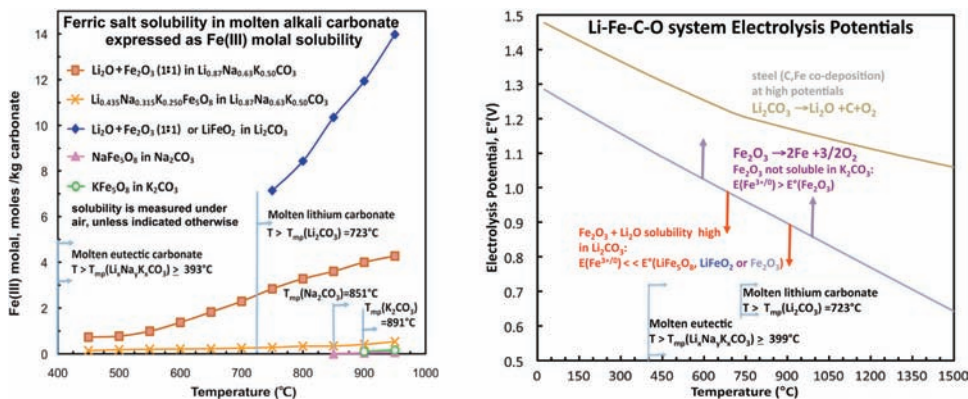
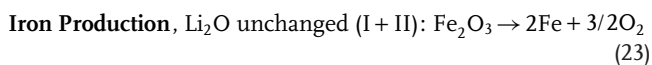
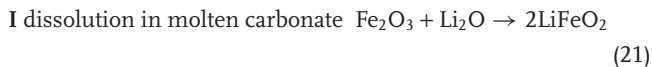


Figure 8. Left: Measured ferric oxides solubilities in alkali molten carbonates. Right: Calculated unit activity electrolysis potentials of LiFe₅O₈, Fe₂O₃ or Li₂CO₃. Vertical arrows indicate Nernstian shifts at high or low Fe(III). Modified with permission from [5].

steady state concentration of LiFeO_2 in accord with the reaction of Equation 21 (but occurring in molten carbonate).^[6] However, 1 equivalent of Li_2O and 1 equivalent of Fe_2O_3 , or LiFeO_2 , dissolves without the reactive formation of CO_2 . This is significant for the electrolysis of Fe_2O_3 in molten carbonate. As LiFeO_2 is reduced Li_2O is released, Equation 22, facilitating the continued dissolution of Fe_2O_3 without CO_2 release or change in the electrolyte. More concisely, iron production via hematite in Li_2CO_3 is given by I and II:



As indicated in Figure 6, a molar excess, of greater than 1:1 of Li_2O to Fe_2O_3 in molten Li_2CO_3 , will further inhibit the Equation 1 disproportionation of lithium carbonate. The right side of Figure 8 summarizes the thermochemical calculated potentials constraining iron production in molten carbonate. Thermodynamically it is seen that at higher potential, steel (iron containing carbon) may be directly formed via the concurrent reduction of CO_2 , which we observe in the Li_2CO_3 at higher electrolysis potential, as $\text{Li}_2\text{CO}_3 \rightarrow \text{C} + \text{Li}_2\text{O} + \text{O}_2$, followed by carbonate regeneration via Equation 3, to yield by electrolysis in molten carbonate:



From the kinetic perspective, a higher concentration of dissolved iron oxide improves mass transport, decreases the cathode overpotential and permits higher steady-state current densities of iron production, and will also substantially decrease the thermodynamic energy needed for the reduction to iron metal. In the electrolyte Fe(III) originates from dissolved ferric oxides, such as LiFeO_2 or LiFe_5O_8 . The potential for the $3e^-$ reduction to iron varies in accord with the general Nerstian expression, for a concentration $[\text{Fe(III)}]$, at activity coefficient, α :

$$E_{\text{Fe(III)/0}} = E^\circ_{\text{Fe(III)/0}} + (RT/nF)\log(\alpha_{\text{Fe(III)}}[\text{Fe(III)}])^{1/3} \quad (25)$$

This decrease in electrolysis potential is accentuated by high temperature and is a ~ 0.1 V per decade increase in Fe(III) concentration at 950°C . Higher activity coefficient, $\alpha_{\text{Fe(III)}} > 1$, would further decrease the thermodynamic potential to produce iron. The measured electrolysis potential is presented on the right of Figure 7 for dissolved Fe(III) in molten Li_2CO_3 , and is low. For example 0.8V sustains a current density of 500 mA cm^{-2} in 14 m Fe(III) in Li_2CO_3 at 950°C . Higher temperature, and higher concentration, lowers the electrolysis voltage, which can be considerably less than the room potential required to convert Fe_2O_3 to iron and oxygen. When an external source of heat, such as solar thermal, is available then the energy savings over room temperature iron electrolysis are considerable.

Electrolyte stability is regulated through control of the CO_2 pressure and/or by dissolution of excess Li_2O . Electrolyte mass change was measured in 7 m LiFeO_2 and $3.5\text{ m Li}_2\text{O}$ in molten

Li_2CO_3 after 5 hours. Under argon there is a 1, 5, or 7 wt% loss at 750 , 850 , or 950°C , respectively), through CO_2 evolution. Little loss occurs under air (0.03% CO_2), while under pure CO_2 the electrolyte gains 2–3 wt% (external CO_2 reacts with dissolved Li_2O to form Li_2CO_3).

The endothermic nature of the new synthesis route, that is the decrease in iron electrolysis potential with increasing temperature, provides a low free energy opportunity for the STEP process. In this process, solar thermal provides heat to decrease the iron electrolysis potential, Figure 7, and solar visible generates electronic charge to drive the electrolysis. A low energy route for the carbon dioxide free formation of iron metal from iron ores is accomplished by the synergistic use of both visible and infrared sunlight. This provides high solar energy conversion efficiencies, Figure 2, when applied to Equations 14 and 20 in a molten carbonate electrolytes. We again use a 37% solar energy conversion efficient concentrator photovoltaic (CPV) as a convenient power source to drive the low electrolysis energy iron deposition without CO_2 formation in Li_2CO_3 ,^[3] as schematically represented in Figure 9.

A solar/wind hybrid solar thermal electrochemical production (Hy-STEP) iron electrolysis process is also demonstrated.^[6] In lieu of solar electric, electronic energy can be provided by alternative renewables, such as wind. As shown on the right side of Figure 9, in this Hy-STEP example, the electronic energy is driven by a wind turbine and concentrated sunlight is only used to provide heat to decrease the energy required for iron splitting. In this process, sunlight is concentrated to provide effective heating, but is not split into separate spectral regions as in our alternative implementation. Hy-STEP iron production is measured with a $31.5'' \times 44.5''$ Fresnel lens (Edmund Optics) which concentrates sunlight to provide temperatures of over 950°C , and a Sunforce-44444 400 W wind turbine provides electronic charge, charging series nickel metal hydride, MH, cells at 1.5V). Each MH cell, provides a constant discharge potential of $1.0\text{--}1.3\text{ V}$, which are each used to drive one or two series connected iron electrolysis cells as indicated in the right side of Figure 9, containing 14 m Fe(III) molten Li_2CO_3 electrolysis cells. Electrolysis current is included in the lower right of Figure 9. Iron metal is produced. Steel (iron containing carbon) may be directly formed via the concurrent reduction of CO_2 , as will be delineated in an expanded study.

3.4. STEP Chlorine and Magnesium Production (Chloride Electrolysis)

The predominant salts in seawater (global average $3.5 \pm 0.4\%$ dissolved salt by mass) are NaCl (0.5 M) and MgCl_2 (0.05 M). The electrolysis potential for the industrial chlor-alkali reaction exhibits little variation with temperature, and hence the conventional generation of chlorine by electrolysis, Equation 11, would not benefit from the inclusion of solar heating.^[3] However, when confined to anhydrous chloride splitting, as exemplified in the lower portion of Figure 1, the calculated potential for the anhydrous electrolysis of chloride salts is endothermic for the electrolyses, which generate a chlorine and metal product. The application of excess heat, as through the STEP process, decreases the energy of electrolysis and can improve the

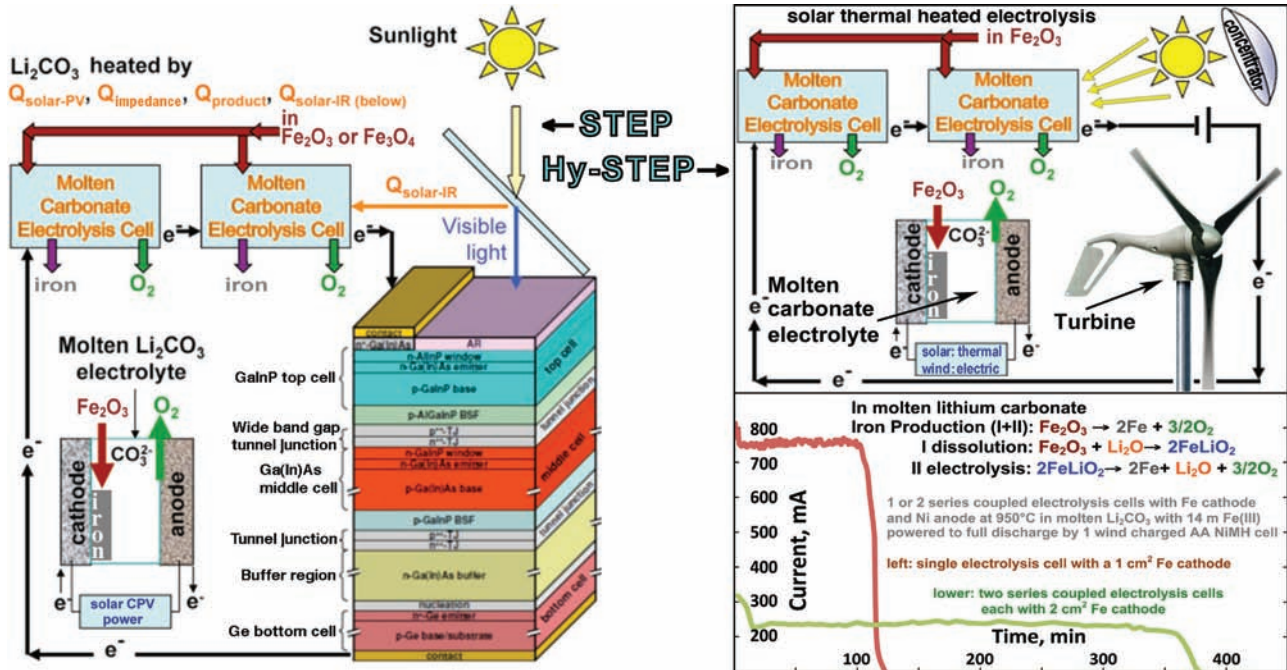


Figure 9. STEP and (wind) Hy-STEP iron. Left: STEP iron production in which two molten carbonate electrolysis in series are driven by a concentrator photovoltaic. The 2.7 V maximum power of the CPV can drive either two 1.35 V iron electrolyses at 800 °C (schematically represented), or three 0.9 V iron electrolyses at 950 °C. At 0.9V, rather than at $E^{\circ}(25\text{ }^{\circ}\text{C}) = 1.28\text{V}$, there is a considerably energy savings, achieved through the application of external heat, including solar thermal, to the system. Right: The Hy-STEP solar thermal/wind production of CO₂ free iron. Concentrated sunlight heats, and wind energy drives electronic transfer into the electrolysis chamber. The required wind powered electrolysis energy is diminished by the high temperature and the high solubility of iron oxide. Bottom: Iron is produced at high current density and low energy at an iron cathode and with a Ni anode in 14 m Fe₂O₃ + 14 m Li₂O dissolved in molten Li₂CO₃. Modified with permission from [6].

kinetics of charge transfer for the equation 12 range of chloride splitting processes. The thermodynamic electrolysis potential for the conversion of NaCl to sodium and chlorine decreases, from 3.24 V at the 801 °C melting point, to 2.99 V at 1027 °C.^[3] Experimentally, at 850 °C in molten NaCl, we observe the expected, sustained generation of yellow-green chlorine gas at a platinum anode and of liquid sodium (mp 98 °C) at the cathode. Electrolysis of a second chloride salt, MgCl₂, is also of particular interest. The magnesium, as well as the chlorine, electrolysis products are significant societal commodities. Magnesium metal, the third most commonly used metal, is generally produced by the reduction of calcium magnesium carbonates by ferrosilicons at high temperature,^[88] which releases substantial levels of carbon dioxide contributing to the anthropogenic greenhouse effect. However, traditionally, magnesium has also been produced by the electrolysis of magnesium chloride, using steel cathodes and graphite anodes, and alternative materials have been investigated.^[89]

Of significance, here to the STEP process, is the highly endothermic nature of anhydrous chloride electrolysis, such as for MgCl₂ electrolysis, in which solar heat will also decrease the energy (voltage) needed for the electrolysis. The rest potential for electrolysis of magnesium chloride decreases from 3.1 V, at room temperature, to 2.5 V at the 714 °C melting point. As seen in **Figure 10**, the calculated thermodynamic potential for the electrolysis of magnesium chloride continues to decrease with increasing temperature, to ~2.3 V at 1000 °C. The 3.1 V energy

stored in the magnesium and chlorine room temperature products, when formed at 2.3 V, provide an energy savings of 35%, if sufficient heat applied to the process can sustain this lower formation potential. Figure 10 also includes the experimental decrease in the MgCl₂ electrolysis potential with increasing temperature in the lower right portion. In the top portion of the figure, the concurrent shift in the cyclic voltammogram is evident, decreasing the potential peak of magnesium formation, with increasing temperature from 750 °C to 950 °C. Sustained electrolysis and generation of chlorine at the anode and magnesium at the cathode (Figure 10, photo inset) is evident at platinum electrodes. The measured potential during constant current electrolysis at 750 °C in molten MgCl₂ at the electrodes is included in the figure.

In the magnesium chloride electrolysis cell, nickel electrodes yield similar results to platinum, and can readily be used to form larger electrodes. The nickel anode sustains extended chlorine evolution without evident deterioration; the nickel cathode may slowly alloy with deposited magnesium. The magnesium product forms both as the solid and liquid (Mg mp 649 °C). The liquid magnesium is less dense than the electrolyte, floats upwards, and eventually needs to be separated and removed to prevent an inter-electrode short, or to prevent a reaction with chlorine that is evolved at the anode. In a scaled up cell configuration (not shown in Figure 10, a larger Ni cathode (200 cm² cylindrical nickel sheet (McMaster 9707K35) was employed, sandwiched between two coupled cylindrical Ni sheet anodes

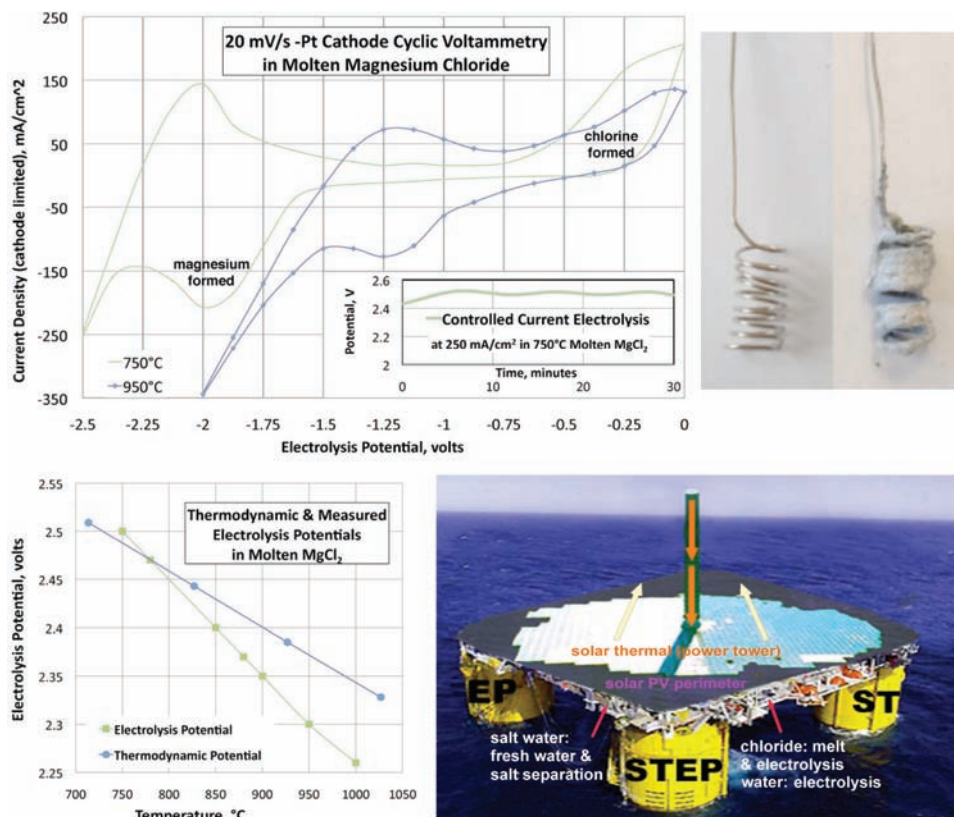


Figure 10. Photograph lower left: coiled platinum before (left), and after (right), MgCl₂ electrolysis forming Mg metal on the cathode (shown) and evolving chlorine gas on the anode. Main figure: cathode size restricted cyclic voltammetry of Pt electrodes in molten MgCl₂. Inset: The measured full cell potential during constant current electrolysis at 750 °C in molten MgCl₂. Lower right: Thermodynamic and measured electrolysis potentials in molten MgCl₂ as a function of temperature. Electrolysis potentials are calculated from the thermodynamic free energies components of the reactants and products as $E = -\Delta G(\text{reaction})/2F$. Measured electrolysis potentials are stable values on Pt at 0.250 A/cm² cathode.^[8] Lower right: A schematic representation of a separate (i) solar thermal and (ii) photovoltaic field to drive both water purification, hydrogen generation, and the endothermic electrolysis of the separated salts to useful products. Modified with permission from [8].

(total 200 cm², of area across from the cathode) in a 250 mL alumina (Adavalue) crucible, and sustains multi-ampere currents. The potential at constant current is initially stable, but this cell configuration leads to electrical shorts, unless liquid magnesium is removed.

One salt source for the STEP generation of magnesium and chlorine from MgCl₂ are via chlorides extracted from salt water, with the added advantage of the generation of less saline water as a secondary product. In the absence of effective heat exchanger, concentrator photovoltaics heat up to over 100 °C, which decreases cell performance. Heat exchange with the (non-illuminated side of) concentrator photovoltaics can vaporize seawater for desalination and simultaneously prevent overheating of the CPV. The simple concentrator STEP mode (coupling super-bandgap electronic charge with solar thermal heat) is applicable when sunlight is sufficient to both generate electronic current for electrolysis and sustain the electrolysis temperature. In cases, requiring both the separation of salts from aqueous solution followed by molten electrolysis of the salts, a single source of concentrated sunlight can be insufficient, to both drive water desalination, and to also heat and drive electrolysis of the molten salts. Figure 10 includes a

schematic representation of a Hy-STEP process with separate (i) solar thermal and (ii) photovoltaic field to drive both desalination and the endothermic carbon dioxide-free electrolysis of the separated salts, or water splitting, to useful products. As illustrated, the separate thermal and electronic sources may each be driven by insolation, or alternatively, can be (i) solar thermal and (ii) (not illustrated) wind, water, nuclear or geothermal driven electronic transfer.

4. STEP Constraints

4.1. STEP Limiting Equations

As illustrated on the left side of Scheme 2, the ideal STEP electrolysis potential incorporates not only the enthalpy needed to heat the reactants to T_{STEP} from T_{ambient}, but also the heat recovered via heat exchange of the products with the inflowing reactant. In this derivation it is convenient to describe this combined heat in units of voltage via the conversion factor nF:

$$Q_T \equiv \sum_i H_i(R_i, T_{\text{STEP}}) - \sum_i H_i(R_i, T_{\text{ambient}}) - \sum_i H_i(C_i, T_{\text{STEP}}) + \sum_i H_i(C_i, T_{\text{ambient}}); E_Q(V) = -Q_T(J) \text{ mol} / nF \quad (26)$$

The energy for the process, incorporates E_T , E_Q , and the non-unit activities, via inclusion of Equation 26 into Equation 4, and is termed the STEP potential, E_{STEP} :

$$E_{\text{STEP}}(T, a) = [-\Delta G^\circ(T) - Q_T - RT \cdot \ln(\prod_{i=1 \text{ to } x} a(R_i)^{r_i} / \prod_{i=1 \text{ to } y} a(P_i)^{p_i})] / nF; E_{\text{STEP}}^\circ(a=1) = E_T^\circ + E_Q \quad (27)$$

In a pragmatic electrolysis system, product(s) can be drawn off at activities that are less than that of the reactant(s). This leads to large activity effects in Equation 27 at higher temperature,^[3-6,8,53-55] as the RT/nF potential slope increases with T (e.g., increasing three-fold from 0.0592V/n at 25 °C to 0.183V/n at 650 °C).

The STEP factor, A_{STEP} is the extent of improvement in carrying out a solar driven electrolysis process at T_{STEP} , rather than at T_{ambient} . For example, when applying the same solar energy, to electronically drive the electrochemical splitting of a molecule which requires only two thirds the electrolysis potential at a higher temperature, then $A_{\text{STEP}} = (2/3)^{-1} = 1.5$. In general, the factor is given by:

$$A_{\text{STEP}} = E_{\text{STEP}}(T_{\text{ambient}}, a) / E_{\text{STEP}}(T_{\text{STEP}}, a); \text{ e.g. } T_{\text{ambient}} = 298 \text{ K} \quad (28)$$

The STEP solar efficiency, η_{STEP} , is constrained by both photovoltaic and electrolysis conversion efficiencies, η_{PV} and $\eta_{\text{electrolysis}}$, and the STEP factor. In the operational process, passage of electrolysis current requires an additional, combined (anodic and cathodic) overpotential above the thermodynamic potential; that is $V_{\text{redox}} = (1+z)E_{\text{redox}}$. Mobility and kinetics improve at higher temperature and $\xi(T > T_{\text{ambient}}) < \xi(T_{\text{ambient}})$.^[63,67] Hence, a lower limit of $\eta_{\text{STEP}}(V_T)$ is given by $\eta_{\text{STEP-ideal}}(E_T)$. At T_{ambient} , $A_{\text{STEP}} = 1$, yielding $\eta_{\text{STEP}}(T_{\text{ambient}}) = \eta_{\text{PV}} \cdot \eta_{\text{electrolysis}}$. η_{STEP} is additionally limited by entropy and black body constraints on maximum solar energy conversion efficiency. Consideration of a black body source emitted at the sun's surface temperature and collected at ambient earth temperature, limits solar conversion to 0.933 when radiative losses are considered,^[90] which is further limited to $\eta_{\text{PV}} < \eta_{\text{limit}} = 0.868$ when the entropy limits of perfect energy conversion are included.^[91] These constraints on $\eta_{\text{STEP-ideal}}$ and the maximum value of solar conversion, are imposed to yield the solar chemical conversion efficiency, η_{STEP} :

$$\eta_{\text{STEP-ideal}}(T, a) = \eta_{\text{PV}} \eta_{\text{electrolysis}} A_{\text{STEP}}(T, a) \\ \eta_{\text{STEP}}(T, a) \equiv \eta_{\text{PV}} \eta_{\text{electrolysis}}(T_{\text{ambient}}, a) A_{\text{STEP}}(T, a); \\ (\eta_{\text{STEP}} < 0.868) \quad (29)$$

As calculated from Equation 3 and the thermochemical component data^[59b] and as presented in Figure 1, the electrochemical driving force for a variety of chemicals of widespread use by society, including aluminium, iron, magnesium and chlorine, significantly decreases with increasing temperature.

4.2. Predicted STEP Efficiencies for Solar Splitting of CO₂

The global community is increasingly aware of the climate consequences of elevated greenhouse gases. A solution to rising carbon dioxide levels is needed, yet carbon dioxide is a highly stable, noncombustible molecule, and its thermodynamic stability makes its activation energy demanding and challenging. The most challenging stage in converting CO₂ to useful products and fuels is the initial activation of CO₂, for which energy is required. It is obvious that using traditional fossil fuels as the energy source would completely defeat the goal of mitigating greenhouse gases. A preferred route is to recycle and reuse the CO₂ and provide a useful carbon resource. We limit the non-unit activity examples of CO₂ mitigation in Equation 15 to the case when CO and O₂ are present as electrolysis products, which yields $a_{\text{O}_2} = 0.5a_{\text{CO}}$, and upon substitution into Equation 27:

$$E_{\text{STEP}}(T, a) = E_{\text{STEP}}^\circ(T) - (RT/2F) \cdot \ln(N); E^\circ(25^\circ\text{C}) \\ = 1.333 \text{ V}; N = \sqrt{2} a_{\text{CO}_2} a_{\text{CO}}^{-3/2} \quad (30)$$

The example of $E_{\text{STEP}}(T, a \neq 1)$ on the left side of Figure 11 is derived when $N = 100$, and results in a substantial drop in the energy to split CO₂ due to the discussed influence of $RT/2F$. Note at high temperature conditions in the figure, $E_{\text{STEP}} < 0$ occurs, denoting the state in which the reactants are spontaneously formed (without an applied potential). This could lead to the direct thermochemical generation of products, but imposes substantial experimental challenges. To date, analogous direct water splitting attempts, are highly inefficient due to the twin challenges of high temperature material constraints and the difficulty in product separation to prevent back reaction upon cooling.^[92] The STEP process avoids this back reaction through the separation of products, which spontaneously occurs in the electrochemical, rather than chemical, generation of products at separate anode and cathode electrodes.

The differential heat required for CO₂ splitting, E_Q , and the potential at unit activity, E_{STEP}° , are calculated and presented in the top of Figure 11. E_Q has also been calculated and is included. E_Q is small (comprising tens of millivolts or less) over the entire temperature range. Hence from Equation 27, E_{STEP}° does not differ significantly from the values presented for E_T° for CO₂ in Figure 2. $\text{ECO}_2\text{split}(25^\circ\text{C})$ yields $A_{\text{STEP}}(T) = 1.333\text{V}/E_{\text{STEP}}^\circ(T)$ with unit activity, and $A_{\text{STEP}}(T) = 1.197\text{V}/E_{\text{STEP}}^\circ(T)$ for the $N = 100$ case. Large resultant STEP factors are evident in the left of Figure 11. This generates substantial values of solar to chemical energy conversion efficiency for the STEP CO₂ splitting to CO and O₂.

A STEP process operating in the $\eta_{\text{PV}} \cdot \eta_{\text{electrolysis}}$ range of 0.20 to 0.40 includes the range of contemporary 25% to 45% efficient concentrator photovoltaics,^[69] and electrolysis efficiency range of 80% to 90%. From these, the CO₂ solar splitting efficiencies are derived from Equations 29 and 30, and are summarized on the right side of Figure 11. The small values of $E_{\text{STEP}}(T)$ at higher T , generate large STEP factors, and result in high solar to chemical energy conversion efficiencies for the splitting of CO₂ to CO and O₂. As one intermediate example from Equation 30, we take the case of an electrolysis efficiency of 80% and a 34% efficient photovoltaic ($\eta_{\text{PV}} \cdot \eta_{\text{electrolysis}} = 0.272$). This will drive STEP solar CO₂ splitting at molten carbonate temperatures (650 °C)

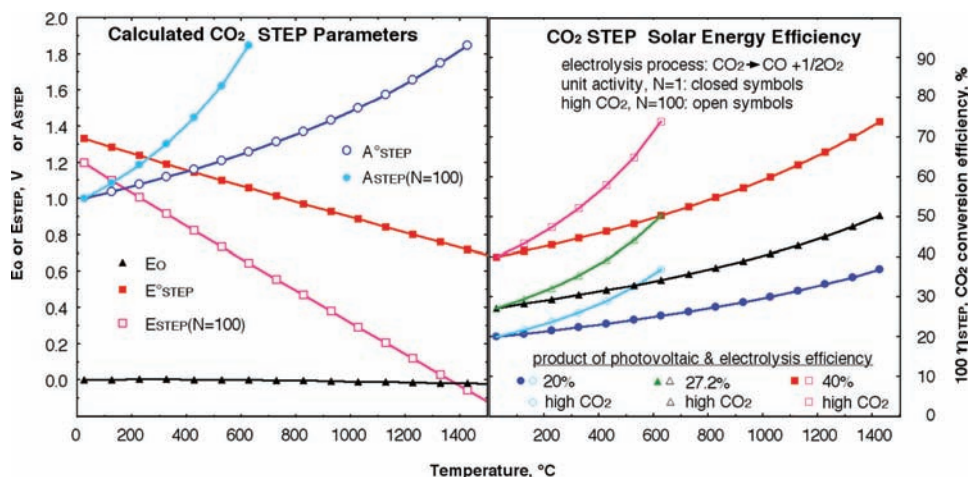


Figure 11. Top: Calculated STEP parameters for the solar conversion of CO₂. Bottom: Solar to chemical conversion efficiencies calculated through Equation 29 for the conversion of CO₂ to CO and O₂. In the case in which the product of the photovoltaic and electrolysis efficiency is 27.2% ($\eta_{PV} \cdot \eta_{\text{electrolysis}} = 0.272$), the STEP conversion efficiency at unit activity is 35%, at the 650 °C temperature consistent with molten carbonate electrolysis, rising to 40% at the temperature consistent with solid oxide electrolysis (1000 °C). Non-unit activity calculations presented are for the case of $\sqrt{2} a_{\text{CO}_2} a_{\text{CO}}^{-3/2} = 100$. A solar conversion efficiency of 50% is seen at 650 °C when $N = 100$ (the case of a cell with 1 bar of CO₂ and ~58 mbar CO). Modified with permission from [3].

at a solar conversion efficiency of 35% in the unit activity case, and at 50% when $N = 100$ (the case of a cell with 1 bar of CO₂ and ~58 mbar CO).

4.3. Scalability of STEP Processes

STEP can be used to remove and convert carbon dioxide. As with water splitting, the electrolysis potential required for CO₂ splitting falls rapidly with increasing temperature (Figure 1), and we have shown here (Figure 2) that a photovoltaic, converting solar to electronic energy at 37% efficiency and 2.7 V, may be used to drive three CO₂ splitting, lithium carbonate electrolysis cells, each operating at 0.9 V, and each generating a 2 electron CO product. The energy of the CO product is 1.3V (Equation 1), even though generated by electrolysis at only 0.9V due to synergistic use of solar thermal energy. As seen in Figure 5, at lower temperature (750 °C, rather than 950 °C), carbon, rather than CO, is the preferred product, and this 4 electron reduction approaches 100% Faradaic efficiency.

The CO₂ STEP process consists of solar driven and solar thermal assisted CO₂ electrolysis. Industrial environments provide opportunities to further enhance efficiencies; for example fossil-fueled burner exhaust provides a source of relatively concentrated, hot CO₂. The product carbon may be stored or used, and the higher temperature product carbon monoxide can be used to form a myriad of industrially relevant products including conversion to hydrocarbon fuels with hydrogen (which is generated by STEP water splitting in Section 3.1), such as smaller alkanes, dimethyl ether, or the Fischer Tropsch generated middle-distillate range fuels of C11-C18 hydrocarbons including synthetic jet, kerosene and diesel fuels.^[93] Both STEP and Hy-STEP represent new solar energy conversion processes to produce energetic molecules. Individual components used in the process are rapidly maturing technologies

including wind electric,^[94] molten carbonate fuel cells,^[67] and solar thermal technologies.^[95–100]

It is of interest whether material resources are sufficient to expand the process to substantially impact (decrease) atmospheric levels of carbon dioxide. The buildup of atmospheric CO₂ levels from a 280 to 392 ppm occurring over the industrial revolution comprises an increase of 1.9×10^{16} mole (8.2×10^{11} metric tons) of CO₂,^[101] and will take a comparable effort to remove. It would be preferable if this effort results in usable, rather than sequestered, resources. We calculate below a scaled up STEP capture process can remove and convert all excess atmospheric CO₂ to carbon.

In STEP, 6 kWh m⁻² of sunlight per day, at 500 suns on 1 m² of 38% efficient CPV, will generate 420 kWh at 2.7 V to drive three series connected molten carbonate electrolysis cells to CO, or two series connected series connected molten carbonate electrolysis cells to form solid carbon. This will capture 7.8×10^3 moles of CO₂ day⁻¹ to form solid carbon (based on 420 kWh·2 series cells/ 4 Faraday mol⁻¹ CO₂). The CO₂ consumed per day is three fold higher to form the carbon monoxide product (based on 3 series cells and 2 F mol⁻¹ CO₂) in lieu of solid carbon. The material resources to decrease atmospheric carbon dioxide concentrations with STEP carbon capture, appear to be reasonable. From the daily conversion rate of 7.8×10^3 moles of CO₂ per square meter of CPV, the capture process, scaled to 700 km² of CPV operating for 10 years can remove and convert all the increase of 1.9×10^{16} mole of atmospheric CO₂ to solid carbon. A larger current density at the electrolysis electrodes, will increase the required voltage and would increase the required area of CPVs. While the STEP product (chemicals, rather than electricity) is different than contemporary concentrated solar power (CSP) systems, components including a tracker for effective solar concentration are similar (although an electrochemical reactor, replaces the mechanical turbine). A variety of CSP installations, which include molten salt heat

storage, are being commercialized, and costs are decreasing. STEP provides higher solar energy conversion efficiencies than CSP, and secondary losses can be lower (for example, there are no grid-related transmission losses). Contemporary concentrators, such as based on plastic Fresnel or flat mirror technologies, are relatively inexpensive, but may become a growing fraction of cost as concentration increases.^[100] A greater degree of solar concentration, for example 2000 suns, rather than 500 suns, will proportionally decrease the quantity of required CPV to 175 km², while the concentrator area will remain the same at 350 000 km², equivalent to 4% of the area of the Sahara desert (which averages ~6 kWh m⁻² of sunlight per day), to remove anthropogenic carbon dioxide in ten years.

A related resource question is whether there is sufficient lithium carbonate, as an electrolyte of choice for the STEP carbon capture process, to decrease atmospheric levels of carbon dioxide. 700 km² of CPV plant will generate 5×10^{13} A of electrolysis current, and require ~2 million metric tonnes of lithium carbonate, as calculated from a 2 kg/l density of lithium carbonate, and assuming that improved, rather than flat, morphology electrodes will operate at 5 A/cm² (1000 km²) in a cell of 1 mm thick. Thicker, or lower current density, cells will require proportionally more lithium carbonate. Fifty, rather than ten, years to return the atmosphere to pre-industrial carbon dioxide levels will require proportionally less lithium carbonate. These values are viable within the current production of lithium carbonate. Lithium carbonate availability as a global resource has been under recent scrutiny to meet the growing lithium battery market. It has been estimated that the current global annual production of 0.13 million tonnes of LCE (lithium carbonate equivalents) will increase to 0.24 million tonnes by 2015.^[102] Potassium carbonate is substantially more available, but as noted in the main portion of the paper can require higher carbon capture electrolysis potentials than lithium carbonate.

5. Conclusions

To mitigate the consequences of rising atmospheric carbon dioxide levels and its effect on global climate change, there is a drive to replace conventional fossil fuel driven electrical production by renewable energy driven electrical production. In addition to the replacement of the fossil fuel economy by a renewable electrical economy, we suggest that a renewable chemical economy is also warranted. Solar energy can efficiently be used, as demonstrated with the STEP process, to form the chemicals needed by society without carbon dioxide emission directly and efficiently. Iron, a basic commodity, currently accounts for the release of one quarter of worldwide CO₂ emissions by industry, which may be eliminated by replacement with the STEP iron process. The unexpected solubility of iron oxides in lithium carbonate electrolytes, coupled with facile charge transfer and a sharp decrease in iron electrolysis potentials with increasing temperature, provides a new route for iron production. Iron is formed without an extensive release of CO₂ in a process compatible with the predominant naturally occurring iron oxide ores, hematite, Fe₂O₃, and magnetite, Fe₃O₄. STEP can also be used in direct carbon capture, and the efficient solar generation of hydrogen and other fuels.

In addition to the removal of CO₂, the STEP process is shown to be consistent with efficient solar generation from a variety of metals, as well as chlorine via endothermic electrolyses. Commodity production and fuel consumption processes are responsible for the majority of industry based CO₂ release, and their replacement by STEP processes provides a path to end the root cause of anthropogenic global warming, as a transition beyond the fossil fuel, electrical, or hydrogen economy, to a renewable chemical economy based on the direct formulation of the materials needed by society. An expanded understanding of electrocatalysis and materials will advance the efficient electrolysis of STEP's growing portfolio of energetic products.

Acknowledgements

The author is grateful to Baohui Wang and Hongun Wu for excellent experimental contributions to references 4 and 5.

Received: August 18, 2011

Revised: September 13, 2011

Published online:

- [1] *On Solar Hydrogen & Nanotechnology*, (Ed: L. Vayssieres), John Wiley and Sons, Weinheim, Germany 2009.
- [2] *The Solar Generation of Hydrogen: Towards a Renewable Energy Future* (Eds: K. Rajeshwar, S. Licht, R. McConnell), Springer, New York, USA 2008.
- [3] S. Licht, *J. Phys. Chem. C* 2009, 113, 16283.
- [4] S. Licht, B. Wang, S. Ghosh, H. Ayub, D. Jiang, J. Ganely, *J. Phys. Chem. Lett.* 2010, 1, 2363.
- [5] S. Licht, B. Wang, *Chem. Commun.* 2010, 46, 7004.
- [6] S. Licht, H. Wu, Z. Zhang, H. Ayub, *Chem. Commun.* 2011, 47, 3081.
- [7] S. Licht, O. Chityat, H. Bergmann, A. Dick, S. Ghosh, H. Ayub, *Int. J. Hyd. Energy* 2010, 35, 10867.
- [8] S. Licht, B. Wang, H. Wu, *J. Phys. Chem. C* 2011, 115, 11803.
- [9] G. Ohla, P. Surya, S. Licht, N. Jackson, *Reversing Global Warming: Chemical Recycling and Utilization of CO₂*. Report of the National Science Foundation sponsored 7-2008 Workshop, 17 pages 2009; full report available at: <http://www.usc.edu/dept/chemistry/loker/ReversingGlobalWarming.pdf>
- [10] C. Graves, S. Ebbesen, M. Mogensen, K. Lackner, *Renewable Sustainable Energy Rev.* 2011, 15, 1.
- [11] J. Barber, *Chem. Soc. Rev.* 2009, 38, 185.
- [12] A. Stamatou, P. G. Loutzenhiser, A. Steinfeld, *Energy Fuels* 2010, 24, 2716.
- [13] S. Abanades, M. Chambon, *Energy Fuels* 2010, 24, 6677.
- [14] L. J. Venstrom, J. H. Davidson, *J. Solar Energy Eng. Chem.* 2010, 133, 011017–011021.
- [15] W. Chueh, S. Haile, *Phil. Trans. Roy. Soc. A* 2010, 368, 3269.
- [16] J. Miller, M. Allendorf, R. Diver, L. Evans, N. Siegel, J. Stueker, *J. Mater. Sci.* 2008, 43, 4714.
- [17] S. Licht, *Nature* 1987, 330, 148.
- [18] S. Licht, D. Peramunage, *Nature* 1990, 345, 330.
- [19] B. Oregan, M. Gratzel, *Nature* 1991, 353, 737.
- [20] S. Licht, *J. Phys. Chem.* 1998, 90, 1096.
- [21] *Semiconductor Electrodes and Photoelectrochemistry*, (Ed: S. Licht), Wiley-VCH, Weinheim, Germany 2002.
- [22] S. Licht, G. Hodes, R. Tenne, J. Manassen, *Nature* 1987, 326, 863.
- [23] S. Licht, B. Wang, T. Soga, M. Umeno, *Appl. Phys. Lett.* 1999, 74, 4055.
- [24] S. Yan, L. Wan, Z. Li, Z. Zou, *Chem. Commun.* 2011, 47, 5632.

- [25] H. Zhou, T. Fan, D. Zhang, *ChemCatChem* **2011**, *3*, 513.
- [26] R. Huchinson, E. Holland, B. Carpenter, *Nat. Chem.* **2011**, *3*, 301.
- [27] E. E. Barton, D. M. Rampulla, A. B. Bocarsly, *J. Am. Chem. Soc.* **2008**, *130*, 6342.
- [28] S. Kaneco, H. Katsumata, T. Suzuki, K. Ohta, *Chem Eng. J.* **2006**, *92*, 363.
- [29] P. Pan, Y. Chen, *Catal. Commun.* **2007**, *8*, 1546.
- [30] A. B. Murphy, *Solar Energy Mater.* **2008**, *116*, 227.
- [31] A. Currao, *Chimia* **2007**, *61*, 815.
- [32] a) S. R. Narayanan, B. Haines, J. Soler, T. I. Valdez, *J. Electrochem. Soc.* **2011**, *158*, A167; b) C. Delacourt, J. Newman, *J. Electrochem. Soc.* **2010**, *157*, B1911.
- [33] E. Dufek, T. Lister, M. McIlwain, *J. Appl. Electrochem.* **2011**, *41*, 623.
- [34] M. Gangeri, S. Perathoner, S. Caudo, G. Centi, J. Amadou, D. Begin, C. Pham-Huu, M. Ledoux, J. Tessonnier, D. Su, R. Schlögl, *Catalysis Today* **2009**, *143*, 4714.
- [35] B. Innocent, D. Liaigre, D. Pasquier, F. Ropital, J. Leger, K. Kokoh, *J. Appl. Electrochem.* **2009**, *39*, 227.
- [36] A. Wang, W. Liu, S. Cheng, D. Xing, J. Zhou, B. Logan, *Int. J. Hydrogen Energy* **2009**, *39*, 3653.
- [37] N. Dong-fang, X. Cheng-tian, L. Yi-wen, Z. Li, L. Jiz-xing, *Chem. Res. Chinese U.* **2009**, *34*, 708.
- [38] D. Chu, G. Qin, X. Yuan, M. Xu, P. Zheng, J. Lu, *ChemSusChem* **2008**, *1*, 205.
- [39] J. Yano, T. Morita, K. Shimano, Y. Nanmi, S. Yamsaki, *J. Sol. State Electrochem.* **2007**, *11*, 554.
- [40] Y. Hori, H. Konishi, T. Futamura, A. Murata, O. Koga, H. Sakuri, K. Oguma, *Electrochim. Acta* **2005**, *50*, 5354.
- [41] K. Ogura, H. Yano, T. Tanaka, *Catalysis Today* **2004**, *98*, 414.
- [42] a) H. Chandler, F. Pollara, *AIChE Chem. Eng. Prog. Ser.: Aerospace Life Support* **1966**, *62*, 38; b) L. Elikan, D. Archer, R. Zahradnik, *ibid* **28**.
- [43] a) M. Stancati, J. Niehoff, W. Wells, R. Ash, *AIAA* **1979**, 79-0906, 262; b) R. Richter, *ibid* **1981**, 82-2275, 1.
- [44] a) J. Mizusaki, H. Tagawa, Y. Miyaki, S. Yamauchi, K. Fueki, I. Koshiro, *Solid State Ionics* **1992**, *126*, 53; b) G. Tao, K. Sridhar, C. Chan, *ibid* **2004**, *175*, 615; c) R. Green, C. Liu, S. Adler, *ibid* **2008**, *179*, 647.
- [45] C. Meyers, N. Sullivan, H. Zhu, R. Kee, *J. Electrochem. Soc.* **2011**, *158*, B117.
- [46] P. Kim-Lohsoontorn, N. Laosiripojana, J. Bae, *Current Appl. Phys.* **2011**, *11*, 5223.
- [47] S. Ebbesen, C. Graves, A. Hausch, S. Jensen, M. Mogensen, *J. Electrochem. Soc.* **2010**, *157*, B1419.
- [48] S. Jensen, X. Sun, S. Ebbesen, R. Knibbe, M. Mogensen, *Int. J. Hydrogen Energy* **2010**, *35*, 9544.
- [49] Q. Fu, C. Mabilat, M. Zahid, A. Brisse, L. Gautier, *Energy Environ. Sci.* **2010**, *3*, 1382.
- [50] C. M. Stoops, J. E. O'Brien, K. G. Condie, J. Hartvigsen, *Int. J. Hydrogen Energy* **2010**, *35*, 4861.
- [51] Q. Fu, C. Mabilat, M. Zahid, A. Brisse, L. Gautier, *Energy Environ. Sci.* **2010**, *3*, 1382.
- [52] D. Lueck, W. Buttner, J. Surma, *Fluid System Technologies* **2002**, at: <http://rtreport.ksc.nasa.gov/techreports/2002report/600%20Fluid%20Systems/609.html>.
- [53] S. Licht, *Electrochem. Commun.* **2002**, *4*, 789.
- [54] S. Licht, *J. Phys. Chem. B* **2003**, *107*, 4253.
- [55] S. Licht, L. Halperin, M. Kalina, M. Zidman, N. Halperin, *Chem. Commun.* **2003**, 2003, 3006; S. Licht, *Chem. Commun.* **2005**, 2005, 4623.
- [56] A. Fujishima, K. Honda, *Nature* **1972**, *238*, 37.
- [57] Z. Zou, Y. Ye, K. Sayama, H. Arakawa, *Nature* **2001**, *414*, 625.
- [58] a) S. Licht, B. Wang, S. Mukerji, T. Soga, M. Umento, H. Tributsh, *J. Phys. Chem. B* **2000**, *104*, 8920; b) S. Licht, *J. Phys. Chem. B* **2001**, *105*, 6281.
- [59] a) A. J. deBethune, T. S. Licht, *J. Electrochem. Soc.* **1959**, *106*, 616; b) M. W. Chase, *J. Phys. Chem. Ref. Data* **1998**, *9*, 1; data available at: <http://webbook.nist.gov/chemistry/form-ser.html>
- [60] W. E. Wentworth, E. Chen, *Solar Energy* **1976**, *18*, 205.
- [61] J. O'M. Bockris, *Energy Options*, Halsted Press, NY **1980**.
- [62] T. S. Licht, S. Licht, A. C. Bevilacqua, *Electrochem. Solid State Lett.* **2005**, *8*, E16.
- [63] T. S. Licht, S. Licht, *Anal. Chem.* **1987**, *59*, 2327.
- [64] S. Licht, *Anal. Chem.* **1985**, *57*, 514.
- [65] S. Licht, K. Longo, D. Peramunage, F. Forouzan, *J. Electroanal. Chem.* **1991**, *318*, 119.
- [66] C. Elschenbroich, A. Salzer (*Organometallics*, 2nd Ed., Wiley-VCH, Weinheim,) Germany **1992**.
- [67] K. Sunmacher, *Molten Carbonate Fuel Cells*, Wiley-VCH, Weinheim, Germany **2007**.
- [68] J. L. Pellegrino, *Energy & Environmental Profile of the U.S. Chemical Industry* **2000**, available online at: http://www1.eere.energy.gov/industry/chemicals/tools_profile.html
- [69] a) R. R. King, D. C. Law, K. M. Edmonson, C. M. Fetzer, G. S. Kinsey, H. Yoon, R. A. Sherif, N. H. Karam, *Appl. Phys. Lett.* **2007**, *90*, 183516; b) M. Green, K. Emery, Y. Hishikawa, W. Warata, *Prog. Photovoltaics* **2011**, *19*, 84.
- [70] J. E. Miller, M. D. Allendorf, R. B. Diver, L. R. Evans, N. P. Siegel, J. N. Stuecker, *J. Mater. Sci.* **2008**, *43*, 4714.
- [71] Y. Woolerton, Y. W. Sheard, S. Reinsner, E. Pierce, S. W. Ragsdale, F. A. Armstrong, *J. Am. Chem. Soc.* **2010**, *132*, 2132.
- [72] E. Benson, C. P. Kubiak, A. J. Sathrum, J. M. N. Smieja, *Chem. Soc. Rev.* **2009**, *38*, 89.
- [73] *Principles and Applications of Molten Salt Electrochemistry*, (Eds: Z. Zhang, Z. Wang) Chemical Industry Press, Beijing **2006**, p. 191.
- [74] T. Kojima, Y. Miyazaki, K. Nomura, K. Tanimoto, K. Density, *J. Electrochem. Soc.* **2008**, *155*, F150.
- [75] V. Kaplan, E. Wachtel, K. Gartsman, Y. Feldman, I. Lubormirsky, *J. Electrochem. Soc.* **2010**, *157*, B552.
- [76] L. Andrieux, G. Weiss, *Comptes Rendu* **1944**, *217*, 615.
- [77] G. M. Haarberg, E. Kvalheim, S. Rolseth, T. Murakami, S. Pietrzyk, S. Wang, *ECS Transactions* **2007**, *3*, 341.
- [78] S. Wang, G. M. Haarberg, E. Kvalheim, *J. Iron Res. Int.* **2008**, *15*, 48.
- [79] G. M. Li, D. H. Wang, Z. Chen, *J. Mater. Sci. Tech.* **2009**, *25*, 767.
- [80] B. Y. Yuan, O. E. Kongstein, G. M. Haarberg, *J. Electrochem. Soc.* **2009**, *156*, D64.
- [81] W. Palmar, J. A. Brinell, *Chem. Metall. Eng.* **1913**, *11*, 197.
- [82] F. A. Eustis, *Chem. Metall. Eng.* **1922**, *27*, 684.
- [83] E. Mostad, S. Rolseth, S. Thonstad, *J. Hydrometallurgy* **2008**, *90*, 213.
- [84] L. Qingeng, F. Borum, I. Petrushina, N. J. Bjerrum, *J. Electrochem. Soc.* **1999**, *146*, 2449.
- [85] R. Collongues, G. Chaudron, *Compt. Rend.* **1950**, *124*, 143.
- [86] A. Wijayasinghe, B. Bergman, C. Lagergren, *J. Electrochem. Soc.* **2003**, *150*, A558.
- [87] A. Lykasov, M. Pavlovskaya, *Inorg. Mater.* **2003**, *39*, 1088.
- [88] H. Q. Li, S. S. Xie, *J. Rare Earths* **2005**, *23*, 606.
- [89] G. Demirci, I. Karakaya, *J. Alloys Compd.* **2008**, *465*, 255.
- [90] C. S. Solanki, G. Beaucarne, *Advanced Solar Cell Concepts*, AER India-2006, **2006**, 256.
- [91] A. Luque, A. Marti, *Handbook of Photovoltaic Sci. & Eng.*, (Eds: A. Luque, S. Haegedus), Wiley-VCH, Weinheim, Germany **2003**, 113.
- [92] A. Kogan, *Int. J. Hydrogen Energy* **1998**, *23*, 89.
- [93] A. Andrews, J. Logan, Fischer-Tropsch Fuels from Coal, Natural Gas, and Biomass: Background and Policy. *Congressional Research Service Report for Congress* **2008**, RL34133, (March 27, 2008); available at: http://assets.opencrs.com/rpts/RL34133_20080327.pdf.
- [94] E. Barbier, *Nature* **2010**, *464*, 832.

- [95] Power tower solar technologies are described at: brightsourceenergy.com; ausra.com, esolar.com; bengoasolar.com/corp/web/en/our_projects/solana/.
- [96] Siemens to build molten salt solar thermal test facility in Portugal, siemens.com, 2011, at: http://www.siemens.com/press/pool/de/pressemitteilungen/2011/renewable_energy/ERE201102037e.pdf.
- [97] See: solarreserve.com, 2011, at: <http://www.solarreserve.com/projects.html>.
- [98] Parabolic solar concentrator technologies are described at: stirlinenergy.com.
- [99] Fresnel solar concentrator technologies are described at: amonix.com, energy innovations.com/sunflower.
- [100] R. Pitz-Paal, in *Solar Energy Conversion and Photoenergy Systems*, (Eds. J. B. Galvez, S. M. Rodriguez) EOLSS Publishers, Oxford, UK 2007.
- [101] P. Tans, An accounting of the observed increase in oceanic and atmospheric CO₂ and an outlook for the future. *Oceanography* 2009, 22, 26.
- [102] W. Tahlil, "The Trouble with Lithium 2; Under the Microscope", Meridan International Research, Martainsville, France, 2008, 54.
-

Cite this: *Chem. Commun.*, 2012, **48**, 6019–6021

www.rsc.org/chemcomm

STEP cement: Solar Thermal Electrochemical Production of CaO without CO₂ emission†

Stuart Licht,* Hongjun Wu,‡ Chaminda Hettige, Baohui Wang,‡ Joseph Asercion, Jason Lau and Jessica Stuart

Received 22nd February 2012, Accepted 5th April 2012

DOI: 10.1039/c2cc31341c

New molten salt chemistry allows solar thermal energy to drive calcium oxide production without any carbon dioxide emission. This is accomplished in a one pot synthesis, and at lower projected cost than the existing cement industry process, which after power production, is the largest contributor to anthropogenic greenhouse gas emissions.

Cement production accounts for 5–6% of all anthropogenic CO₂ emissions. Society consumes over 3×10^{12} kg of cement annually, and the cement industry releases 9 kg of CO₂ for each 10 kg of cement produced. The majority of CO₂ emissions occurs during the decarbonation of limestone (CaCO₃) to lime (CaO) described in eqn (1), and the remainder (30 to 40%) from burning fossil fuels, such as coal, to heat the kiln reactors to ~ 900 °C, eqn (2):^{1–3}

ClimateCentral.org recently wrote that no other sector has such a high potential for drastic emission reductions, and while other processes are being explored to sequester cement's CO₂, none eliminate it. In forming CaO, solar thermal reactors have been studied as replacements to the fossil fuel heat in eqn (2).⁴ However, the majority of the CO₂ emissions still occurs (as decarbonation in eqn (1)) in the conventional decarbonation of limestone to lime:

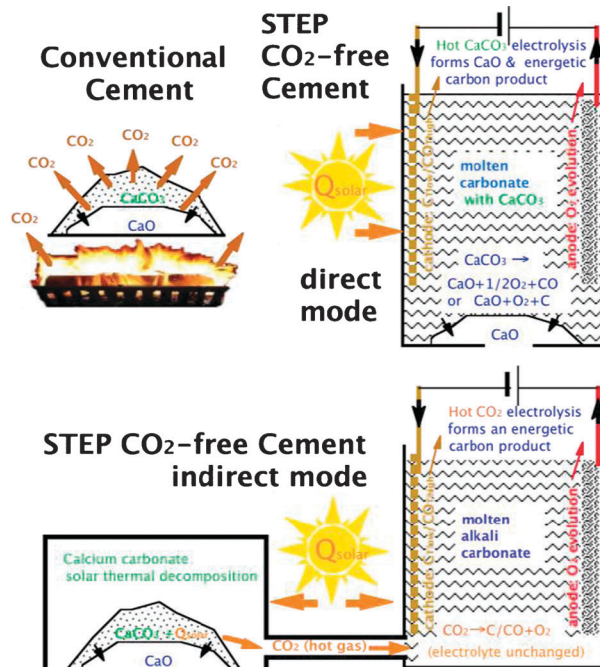


Here we show a new thermal chemistry, based on anomalies in oxide solubilities, to generate CaO, without CO₂ emission, in a high throughput, cost effective, environment conducive to the formation of cement. The aqueous solubility of CaCO₃ (6×10^{-5} m, where molal \equiv moles per kg solvent) is 3 orders of magnitude less than the 2×10^{-2} m solubility of calcium oxide, dissolving as calcium hydroxide. Surprisingly, this situation is reversed at high temperatures in molten carbonates,

which allows the endothermic, electrolytic one pot synthesis, and precipitation of CaO.

Conducive to our new solar process,^{5,6} electrolysis of molten carbonates forms oxides, which precipitate as calcium oxide when mixed with calcium carbonate. Thus no CO₂ is formed, to eliminate cement's greenhouse gas contribution to anthropogenic climate change.

In STEP cement limestone undergoes low energy electrolysis to produce (i) lime, (ii) O₂ and (iii) reduced carbonate without carbon dioxide emission. Alternative configurations of the electrolysis component of this STEP (Solar Thermal Electrochemical Production) are represented in Scheme 1. Compared to the



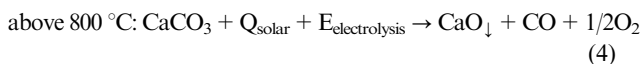
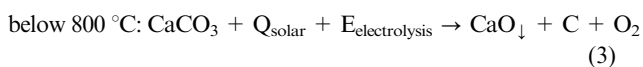
Scheme 1 Conventional thermal decomposition production of lime (top left) versus STEP direct solar conversion of calcium carbonate to calcium oxide (top right) eliminating CO₂. Carbonate electrolysis is endothermic requiring lower potential at higher temperature or carbonate concentration. Solar thermal energy provides the heat to lower this $E_{\text{electrolysis}}$. When this solar heated electrolysis energy is generated by a non-fossil fuel electricity source the process is fully carbon dioxide free. Bottom: the indirect mode of STEP cement as delineated in the ESI.†

Department of Chemistry, George Washington University, Ashburn, Virginia 20147, USA. E-mail: slicht@gwu.edu; Tel: 703 726 8215

† Electronic supplementary information (ESI) available: Expanded experimental details, stability, solubility and product analyses, economic assessment, STEP theory overview, STEP efficiencies and supplementary references. See DOI: 10.1039/c2cc31341c

‡ Present address: Northeast Petroleum Univ., Daqing, P. R. China.

conventional cement thermochemical process (top left), in the STEP cement direct electrolysis configuration (top right), solar thermal heated molten carbonates are electrolyzed forming oxides, which in the presence of calcium carbonate precipitate as lime:



Heat significantly decreases the required electrolysis potentials needed to split calcium carbonate and to drive eqn (3) and (4), to below the electrolysis potential required at room

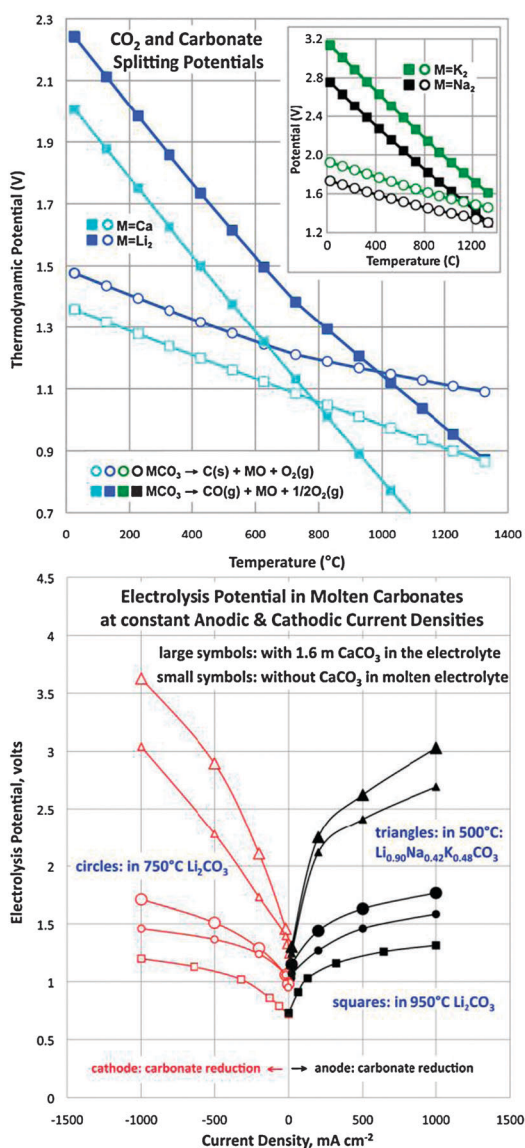


Fig. 1 CO₂ and carbonate splitting potentials. Top: The low thermodynamic potential to electrolyze calcium carbonate in the CO₂-free production of lime. Bottom: The measured full electrolysis potential as a function of current density in either Li₂CO₃ at 750 or 950 °C, or eutectic molten carbonates at 500 °C. At negative currents, the cathode is iron wire, and at positive current, the anode is either nickel or iridium wire (both yield similar electrolysis potentials).

temperature. Our calculated values are summarized on the top of Fig. 1. The unit activity thermodynamic electrolysis potential is lower for CaCO₃ than for lithium, sodium or potassium carbonate electrolyses. The high ratio of molten carbonate reactant to product is expected to further decrease the electrolysis potential.⁵⁻⁷ Below 800 °C in the top figure, the energetically preferred (lower potential) carbon electrolysis product of CaCO₃ is solid carbon, while above that temperature CO is produced.

While calcium hydroxide is water soluble, calcium carbonate is highly insoluble in water, which leads to seashell stability. This situation is reversed at high temperatures in molten carbonates. Fig. 2, top, compares our measured solubility of oxides or calcium carbonate, in either molten lithium carbonate (squares) or a molten alkali carbonate mix (circles), to that of lithium oxide (triangles).

As measured in Fig. 2, at each temperature in either a eutectic mix of carbonates or in pure lithium carbonate, the solubility of calcium oxide is low, and ranges from 30 to 100 times less than the solubility of calcium carbonate, and 50 times less soluble than that of Li₂O. Beyond this low

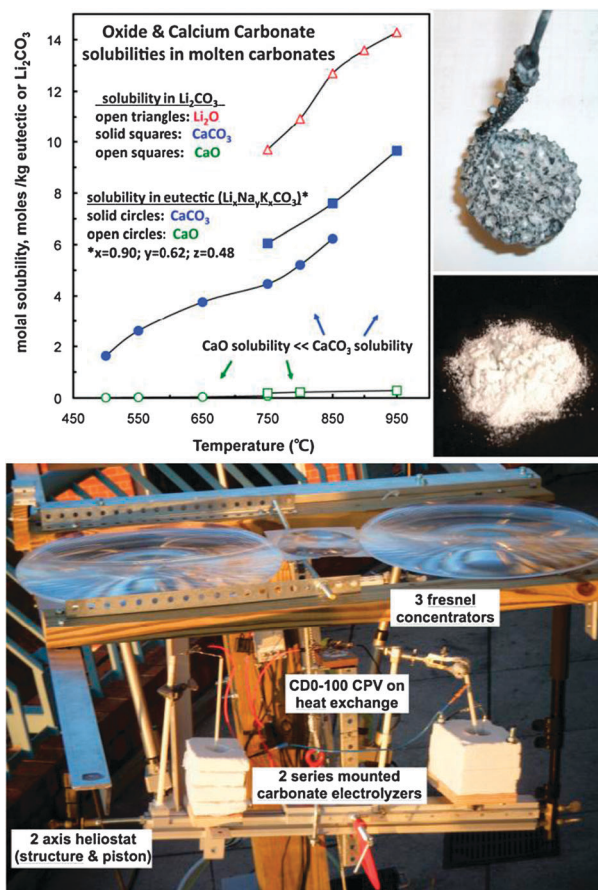


Fig. 2 The low solubility of calcium oxide, compared to calcium carbonate and lithium oxide solubility in molten carbonates (top) facilitates the electrolysis and precipitation of calcium oxide. STEP cement (bottom) with carbonate electrolyzers (detailed in the Electronic Supplementary Information (ESI[†])), CPV and Fresnel concentrators mounted on a Suntura dual axis heliostat. Photographs of 5 h, 1 A 750 °C molten electrolysis products, upper: C and CaO from Li₂CO₃, lower: CaO from Li₂CO₃ containing 1 m Li₂O.

solubility of CaO, when molten carbonates undergo electrolysis to form oxides, added CaCO₃ will precipitate the desired CaO product for extraction, and the added carbonate replenishes the electrolyte for ongoing CaO production.

In 2009 we introduced the STEP theory of an efficient solar chemical process, based on a synergy of solar thermal and endothermic electrolyses.⁵ Solar heat and high molten reactant concentration, substantially decreases the electrolysis energy.⁶ As delineated in the ESI, experimentally, STEP can synthesize chemicals at solar efficiencies of 50%, as demonstrated with CO₂-free production of metals, fuels, and bleach.^{6,7}

STEP cement, the direct CO₂-free synthesis of CaO from calcium carbonate is described and introduced in Scheme 1. In addition to the desired calcium oxide product, lower temperature electrolysis favors the dense storage of captured CO₂ as solid carbon (eqn (3)) at the cathode, while higher temperature electrolysis has the advantage of a lower electrolysis potential, and forms carbon monoxide at the cathode, a useful industrial reagent. The bottom of Fig. 1 summarizes the electrolysis potential measured in molten carbonates during the production of oxide. The indicated 1 A cm⁻² is a high reaction rate, and higher rate, at even lower potential occurs with textured, or porous, rather than flat electrodes such as reticulated (spongy) Ni or iron. The oxide is formed at low energy (low electrolysis potential) and at high rate (high current densities), which is necessary to maintain production for commodities. For example aluminum is commercially produced at 0.8 A cm⁻² in contemporary industrial plants.

Fig. 1 includes the measured full electrolysis potentials in a system constrained by either the anode or cathode surface area. Nickel and iridium are effective anode materials; CaO can improve nickel stability and decrease oxidative attack.^{8,9} Steel is an effective cathode material in this system.

The electrolysis of carbonates is endothermic, which provides the opportunity to add a significant portion of the required energy to drive the process as solar thermal heat. A two axis Suntura heliostat provides orthonormal orientation to sun. Details of the 20 cm² steel cathode and 40 cm² nickel anode cathode electrolysis cell are included in the Electronic Supplementary Information (ESI†). As seen in the bottom of Fig. 2, concentrators direct sunlight to the CPV and electrolysis cells, and within minutes melt the electrolyte.

Electrolysis electrode surface areas were chosen to match the solar cell generated power, and the 2.7 V, 3.5 W drives two electrolysis cells in series at 750 °C and three in series at 950 °C. A Spectrolab CDO-100-C1MJ concentrator solar photovoltaic cell is used to generate 2.7 V at maximum power point, with solar to electrical energy efficiencies of 37% under 500 suns illumination. At maximum power, the 0.99 cm² cell generates 1.3 A at 100 suns, and when masked to 0.2 cm² area generates 1.4 A at 500 suns. Molten salt heat storage, as currently used in concentrator solar power CSP electricity plants, can be adapted to the STEP process. This will facilitate continuous operation independent of the sunlight variation, but has not yet

been incorporated into this outdoor STEP calcium oxide generator. Intermittent and variable sunlight incident on this STEP configuration limits temperature and electric control, and long duration (5 h) electrolyses are conducted indoor at constant temperature and current. Indoors, the measured electrolysis potential is steady throughout the electrolysis. In pure, molten Li₂CO₃ the 0.1 A electrolysis occurs at 1.2 V, and at 1 A occurs at 1.6 V, or 0.9 V, respectively at 750 °C, or 950 °C. At 750 °C and 1 A, the addition of 1 m Li₂O lowers the observed potential to 1.5 V, and the addition of 1 to 6 m CaCO₃ increases the electrolysis potential to 1.8 V.

Constant current Li₂CO₃ electrolysis reduces carbonate, and produces Li₂O, which with the addition of CaCO₃ precipitates CaO (Fig. 2 photo), while oxygen evolves from the anode as oxygen solubility is low.^{10,11} The precipitate is separately identified as CaO by FTIR, XRD, and AA analysis.† The products are CaO, C and oxygen without carbon dioxide evolution. The photo in Fig. 2 shows the carbon and CaO deposited after a 5 h electrolysis at 1 A, resulting in 0.56 g of carbon, 1.5 g of O_{2(gas)} and 2.6 g of lime in quantitative accord with the 5 Ah, 4 electron splitting of carbonate.

This study presents a new chemistry of energy efficient, CO₂-free lime production, and the challenge of system scale-up awaits. It should be noted that the carbonate product is readily removed (dropping cleanly from the extracted steel wire cathode when it is uncoiled, or at higher temperature as a simple evolved gas CO), oxygen evolution is confined to the vicinity of the anode, and the high density calcium oxide product does not decompose in the molten carbonate and forms a slurry at the bottom of the vessel where it may be removed by tap in the same manner in which molten iron is removed from conventional iron production kilns.

In the present study new molten salt chemistry is found which allows solar thermal energy to drive CO₂-free lime production, in a one-pot synthesis, at lower projected cost than the existing cement industry process (details in ESI). After power production, the cement industry is largest single contributor to anthropogenic greenhouse gas emissions.

This work has been partially supported by NSF award 1006568.

References

- 1 Y. Liu, Y. Kuang, N. Huang, Z. Wu and C. Wang, *Int. J. Environ. Pollut.*, 2009, **37**, 369.
- 2 J. Allwood, J. Cullen and R. Milford, *Environ. Sci. Technol.*, 2010, **44**, 1888.
- 3 S. Haselbach, *J. Environ. Eng.*, 2009, **135**, 465.
- 4 A. Meier, E. Bonald, G. Cella, W. Lipinski and D. Wullemmin, *Sol. Energy*, 2006, **80**, 1355.
- 5 S. Licht, *J. Phys. Chem. C*, 2009, **113**, 16283.
- 6 S. Licht, *Adv. Mater.*, 2011, **23**, 5592.
- 7 S. Licht and H. Wu, *J. Phys. Chem. C*, 2011, **115**, 25138.
- 8 H. Yin, *et al.*, *Electrochim. Acta*, 2011, **56**, 3296.
- 9 Y. Yang, I. Sommerville and A. McLean, *Trans. Ind. Met.*, 2006, **59**, 655.
- 10 S. Scaccia and S. Frangini, *J. Mol. Liq.*, 2006, **129**, 133.
- 11 S. Scaccia and S. Frangini, *J. Mol. Liq.*, 2009, **146**, 39.

Electronic Supplementary Information (ESI)

**STEP Cement: Solar Thermal Electrochemical Production of CaO
without CO₂ emission (Chemical Communications)**

Stuart Licht,^{*,a} Hongjun Wu,^{a,b} Chaminda Hettige,^a Baohui Wang,^{a,b} Joseph Asercion,^a Jason Lau,^a
5 Jessica Stuart^a

*CORRESPONDING AUTHOR EMAIL ADDRESS: slicht@gwu.edu

^a Department of Chemistry, George Washington University, Washington, DC 20052, USA.

^b Present address: Northeast Petroleum University, Daqing, P. R. China

10

Content

Expanded experimental details:

Thermodynamic calculations

15 Chemicals, materials, electrolysis configurations

Carbonate stability

Solubility analyses and calcium oxide product analyses

Economic assessment

Addendum: STEP theoretical background

20 Addendum: STEP solar to chemical energy conversion efficiency

Supplementary References

Cement production accounts for 5-6% of all anthropogenic CO₂ emissions. Massive CO₂ emissions also
25 occur with the CaO formed from CaCO₃ for purifying iron and aluminum, for agriculture, glass, paper,
sugar, calcium carbide, and acetylene production, to scrub SO₂ from smoke stacks, to soften water or to
remove phosphates from sewerage.^{12,13} ClimateCentral.org recently wrote that no other sector has such a
high potential for drastic emission reductions, and while other processes are being explored to sequester
cement's CO₂, none eliminate it. Society consumes over 3x10¹² kg of cement annually, and the cement
30 industry releases 9 kg of CO₂ for each 10 kg of cement produced. An alternative to this CO₂ intensive
process is needed. The majority of CO₂ emissions occurs during the decarbonation of limestone (CaCO₃) to
lime (CaO) described in equation 1, and the remainder (30 to 40%) from burning fossil fuels, such as coal,
to heat the kiln reactors to ~900°C, eq. 2:¹⁻³

35 In this Chemical Communications and Electronic Supplementary Information, we show a new thermal
chemistry, based on anomalies in oxide solubilities, to generate CaO, without CO₂ emission, in a high
throughput, cost effective, environment conducive to the formation of cement.

40 **Expanded experimental details:**

Thermodynamic calculations

Electrolysis potentials are calculated from the thermochemical enthalpies and entropies of the reactants.^{14,15}

Chemicals, materials, electrolysis configurations

45 Lithium carbonate was utilized (Li₂CO₃, Alfa Aesar, 99%), lithium oxide (Li₂O (99.5%, Alfa Aesar), sodium
carbonate (Na₂CO₃, Avantor 99.5%), potassium carbonate (K₂CO₃, Avantor 99%), Ni foil (pure Ni 200
McMaster 9707K59), Ni wire (1 mm diameter, 99.5%, Alfa Aesar), steel wire (14 gauge), 25 and 75 μm nickel
and steel sheet (McMaster 95481, 97057), and various crucibles: nickel (Alfa Aesar 35904), steel (VWR
82027), and high purity alumina (99.6% AdValue Technology); crucibles were encased in high temperature
50 foam insulation (McMaster 9353).



Figure 3. Configurations and components used in the STEP electrolysis experiments. Left side: three electrolyses in series, with lithium carbonate using thin planar nickel and steel electrodes, prior to the melt, and prior to addition of external insulation. Middle: high surface area nickel electrode prepared by folding a single rectangle of pure nickel (25 μm or 75 μm thick), connected by spot welded nickel wire (99.5%, 1.0 mm) situated above a cathode for carbon deposition prepared by coiling steel wire, and is shown prior to insertion in the alumina crucible and prior to carbonate addition. Gas evolved from the central electrode can be directed with a large circumference alumina tube (not shown). Right side, high temperature configuration: coiled steel wire cathode in a nickel crucible, which acts both as the cell case and the anode, and is shown prior to the addition of the internal carbonate and external insulation.

Molten carbonate electrolytic synthesis operates in the reverse mode of molten carbonate fuel cells (MCFC); where rather than fuel injection with electricity as a product, electrical energy is supplied and energetic chemical products are generated. MCFC systems have been studied in greater depth than carbonate electrolysis systems. In one MCFC study, the addition of 10 mol% of CaCO_3 to molten carbonate (either $\text{Li}_{1.04}\text{Na}_{0.96}\text{CO}_3$ with 30 mol% CaCO_3 , or $\text{Li}_{1.24}\text{Na}_{0.76}\text{CO}_3$ with 10 mol% CaCO_3) led to a decrease of 50mV in the 150 mA cm^{-2} cell potential at 600 to 700 °C.¹⁷

Configurations and components used in the STEP electrolysis experiments are shown in Figure 3. Effective anodes include the inner submerged walls (28 cm^2) of a 20 ml straight walled nickel crucible, coiled pure nickel wire, and pure, nickel sheet. Steel in various shapes is effective as a cathode including coiled steel wire, and steel, and the inner submerged walls of a straight walled steel crucible. Electrolysis measurements at constant cathodic current density are made with a nickel crucible whose inner walls (with surface area ~60 fold larger than the anode) contact the electrolyte and serve as the anode counter electrode. The constant anodic current density measurements are made with a steel crucible whose inner walls in contact with the electrolyte serve as the cathode counter electrode. These measurements are made with an oversized counter electrode (28 cm^2 cathode for the 0.5 cm^2 anode measurements, and a 28 cm^2 anode for the 0.5 cm^2 cathode current density measurements). Unlike steel, pure nickel as a cathode exhibits a potential shift until coated with electrodeposited carbon, and therefore steel was used as a cathode. While highly stable in lithium carbonate electrolytes, nickel anodes tend to corrode into sodium and potassium carbonate, observable as a green coloration developing in the electrolyte during extended electrolyses. This corrosion decreases when calcium carbonate is in the electrolyte. In molten CaCl_2 it was previously found that NiO solubility decreased with up to 4 mol% CaO concentration, and Ni coated with NiO had much higher stability during anodic polarization.¹² In general the strength of an oxide in melts to donate an electron pair (Lewis basicity) decreases in the order: $\text{K}_2\text{O} > \text{Na}_2\text{O} > \text{Li}_2\text{O} > \text{BaO} > \text{CaO} > \text{MgO} > \text{Fe}_2\text{O}_3 > \text{Al}_2\text{O}_3 > \text{TiO}_2 > \text{B}_2\text{O}_3 > \text{SiO}_2 > \text{P}_2\text{O}_5$.¹³ Ni is a useful cell or electrode candidate material in MCFCs, but slowly degrades via a soluble nickel oxide overlayer. Cassir *et al.* report the of addition of 10% CaCO_3 to 650 °C $\text{Li}_{1.04}\text{Na}_{0.96}\text{CaCO}_3$ is useful to decrease the solubility of NiO from 150 to 100 μmolal in the carbonate mix.¹⁸

We find that iridium is remarkably stable for the oxygen evolution reaction (OER) with no evidence of mass loss or oxidation after hundreds of hours of anode operation over a wide range of current densities, even at higher temperatures even as high as 950 °C in molten lithium carbonate).⁹ In comparison, nickel, is less stable, but also suitable, and develops a protective oxide overlayer with the onset of anodic current, which is effective for facile charge transfer in the OER. In the calcium containing 750°C molten lithium carbonate electrolytes, thin (25 µm) sheet pure nickel (Ni 200, McMaster 97057K51) maintains structural integrity, with no visible signs of corrosion, as a high current anode. The right portion of Figure summarizes measured 1 cathode (open symbols) and anode (closed symbols) constrained electrolysis potentials. In this high carbonate activity media, at low current densities the electrolysis potentials are seen to be less than the unit activity thermodynamic values calculated on the right side of the figure. The addition of calcium carbonate increases the electrolysis potential at high current density, and as recently presented (not shown in Figure 1) the addition of lithium oxide decreases the electrolysis potential.⁹

In the anode constrained measurements portion of Figure 1 (solid symbols), it is seen that electrolysis can be sustained at very high current densities, and that in this high current density domain, the dissolution of 1.6 m calcium carbonate in the carbonate eutectic increases the electrolysis potential by ~400 mV. The electrolysis potential is similar with either a 0.5 cm² nickel or iridium anode, but is marginally (not shown) higher when measured with a 0.5 cm² platinum anode. The right side of Figure 1 also summarizes cathode constrained electrolysis potentials (open symbols) made with steel, an effective cathode for the electrolysis in either the eutectic carbonate or the lithium carbonate. At 500 or 750°C the cathode product, solid carbon, forms readily from molten carbonates, and at higher temperature the cathode product switches to carbon monoxide formation.

Among the pure alkali carbonates, Li₂CO₃ has the lowest melting point at 723°C. Mixed alkali carbonate melting points can be low, including 399°C for the Li_{0.90}Na_{0.62}K_{0.48}CO₃ mix used in Figure 2, and 695°C for the Na_{1.23}K_{0.77}CO₃ eutectic salts. CaCO₃, as aragonite, decomposes at 825 °C, and as calcite melts at 1339 °C.¹⁹ A variety of molten carbonates have been characterized with, and without, added calcium carbonates.^{14-15,20-23} The addition of calcium carbonate can decrease the melting point of a carbonate mix. The sodium/lithium carbonate eutectic, Li_{1.07}Na_{0.93}CO₃, has a melting point of 499°C, but decreases to below 450°C if 2 to 10 mol% equimolar CaCO₃ and BaCO₃ is added.¹⁵

Measurements of electrolyte stability (next section) and certain electrolyses are conducted in pure alumina, rather than metal crucibles. In the highest temperature (950°C) domain, the alumina crucible slowly reacts with concentrated Li₂O to form soluble lithium aluminate. In working electrolysis cells, we avoid this oxidative attack by using stainless steel cases, which are maintained under cathodic bias, and externally encased in high temperature foam insulation; nickel crucibles are also moderately stable under these conditions.

Carbonate stability

Today CaO for cement is made by the thermal decomposition of solid CaCO₃ at 900°C in accord with equation 1. At low temperatures, such as for a 500°C eutectic, molten carbonates are highly stable. With increasing temperature molten metal carbonates will chemically decompose, releasing carbon dioxide and forming the metal oxide, such as for lithium carbonate:



When exposed to atmospheric CO₂, carbonate electrolytes can decompose at higher temperatures. This is prevented with oxide addition, or increase in the CO₂ concentration as the equilibrium in equation 5 is shifted to the left. For example exposed to air, a 750 °C Li₂CO₃ with 5 m Li₂O readily gains mass in time. This is significant as it eliminates the need to pre-concentrate CO₂, and provides a path for the direct absorption (and STEP removal) of atmospheric carbon dioxide.^{8,9}

We have previously calculated the variation of equilibrium equation 5 as a function of temperature and the available thermochemical data (7). The addition of either Li₂O (dissolved) or CO₂ (by replacing air, with pure CO₂ above the melt, displaces the reaction to the left and prevents decomposition of the carbonate melt (7). Our experimental thermogravimetric analyses of carbonates under various conditions are summarized in the Table 1. As seen in the top row, and comparable to the conventional cement process, 97.5% of the initial solid calcium carbonate decomposes via release of CO₂ after 5 hours of heating at 900°C. At 750°C this value falls to 16.0%. Lithium carbonate is molten at 750°C and loses only 1.8 mol % under the same conditions. Dissolved CaCO₃ decomposes at a rate intermediate to pure molten Li₂CO₃ and pure solid CaCO₃. 12 g (6m) of CaCO₃ dissolved in 20 g of Li₂CO₃ exhibits 3.2% decomposition at 750°C. As expected, lowering the temperature (to 735°C) and lowering the concentration of dissolved calcium carbonate to 5 m decreases the observed decomposition (to 3.0%). Air contains 0.03% CO₂. From this CO₂, a molten Li₂CO₃ mix with 5 m Li₂O actually gains mass in time via the back reaction of equation 5, evident as a 1.6 mol% gain in carbonate in the table. This is significant as it eliminates the need to pre-concentrate CO₂, and provides a path for the direct absorption (and STEP removal) of atmospheric carbon dioxide. The measurement is quiescent; the molten mix is exposed directly to air. The rate of direct CO₂ absorption increases with stirring or when air is bubbled into the molten mix.

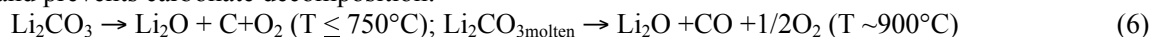
Oxide addition suppresses carbon dioxide emission from molten carbonates, even those containing high concentrations of calcium carbonate, such as 6 m (12 g) CaCO₃ in Li₂CO₃ at 750°C in Table 1. CaO is substantially less soluble than Li₂O in molten carbonates. Conditions are probed in an electrolyte containing a slight excess of CaO to recreate calcium oxide production precipitating (beyond saturation) conditions. Compared to the negligible loss with 5 m Li₂O, and the mol loss of 3.2 % carbonate loss without oxide, the addition of 0.1 m (0.06 g) Li₂O or CaO (0.11 g), respectively decreases the mol loss to 2.3 or 2.0%. These are measured under 1 atmosphere of air. However, if the concentration of carbon dioxide is increased, or if lithium oxide concentration is increased, then equilibrium equation 5 is shifted to the left (back towards the carbonate).

Table 1. Carbonate thermal gravimetry, mass change after heating. mil-mol = millimoles, T = temperature, t = heating time. Note, mass changes are relative, and will also depend on the surface area exposed to the air (rate of mass change will decrease with decreasing surface area).

Car bon ate mil- mol	Mass, g						T °C	t h	Phase	Mass change, g, after heating	CO ₂ milli- moles	Δmole carbon- ate after heating mole %
	CaCO ₃	Li ₂ CO ₃	Na ₂ CO ₃	K ₂ CO ₃	CaO	Li ₂ O						
200	20.003	0	0	0	0	0	900	5	solid	-8.58	-195.	-97.5%
200	20.003	0	0	0	0	0	750	5	solid	-1.40	-31.9	-16.0%
271	0	20.007	0	0	0	0	750	5	molten	-0.21	-4.79	-1.8%
391	12.001	20.001	0	0	0	0	750	5	molten	-0.56	-12.7	-3.2%
371	10.002	20.000	0	0	0	0	735	5	molten	-0.48	-11.0	-3.0%
200	0	20.003	0	0	0	3.044	750	2	molten	+0.14	+3.26	+1.6%
391	12.001	20.003			0	3.030	750	2	molten	-0.020	-0.44	-0.11%
391	12.000	20.002			0	0.061	750	5	molten	-0.40	-9.07	-2.3%
391	12.000	20.002			0.113	0	750	5	molten	-0.35	-7.85	-2.0%
253	6.932	0	9.439	13.126	0	0	750	5	molten	-0.11	-2.56	-1.0%
252	6.905	0	9.403	13.076	0	0	850	5	molten	-0.47	-10.6	-4.2%

30

In the presence of CaCO₃, molten Li₂CO₃ electrolysis forms low solubility CaO. In the absence of this limestone, Li₂CO₃ electrolysis forms highly soluble Li₂O. This electrolysis occurs at lower potential (Fig. 1 right), and prevents carbonate decomposition:



5

At higher temperature, electrolyte decomposition is prevented during the electrolysis of calcium carbonate by electrolysis under CO₂, or by the addition of Li₂O. In the latter case, CaO will be formed when CaCO₃ is added at a rate to maintain a steady state concentration of Li₂O. Above, the low, saturation concentration, CaO precipitates when this limestone is added:



Solubility analyses and calcium oxide product analyses

15 Solubility is determined from multiple measurements including compositions, both approaching saturation, and also in compositions containing excess salts. Solubility was determined redundantly by (i) visible observation, (ii) calcium atomic absorption analysis, (iii) fourier transform infrared (FTIR with a Perkin Elmer Spectrum 100) and (iv) X-ray powder diffraction analysis (XRD powder diffraction data were collected on a Rigaku Miniflex diffractometer and analyzed with the Jade software package.²⁴ Elemental analysis was measured with 20 an AAnalyst 100 Atomic Absorption Spectrometer from Perkin Elmer with a 4 standard point calibration curve being performed at 1ug/mL, 4 ug/mL, 8 ug/mL and 16ug/mL with a J.T. Baker 1000 ug/mL Calcium Standard in 5% Nitric Acid. The measurements, to determine calcium in the electrolyte and products, were performed in 0.540 M HCl with 0.02% Lanthanum Chloride added. As with, XRD, FTIR was determined from a sample of molten electrolyte cooled to room temperature, and compared to spectra we measure of the pure salts. FTIR is 25 measured as a pressed pellet formed by solid mix of the sample with KBR with a fixed mass percentage of barium sulfate. In a methodology we have previously developed, the barium sulfate provides an internal non-reactive standard to quantify other salt concentrations in the sample.²⁵

When oxide is formed by electrolysis in a calcium-free, lithium containing carbonate electrolyte, the 30 oxide is soluble and disperses away from the cathode to the bulk electrolyte. When a concentration of calcium carbonate is then added to the electrolyte which is less than that of the dissolved lithium oxide in the molten carbonate, this calcium carbonate is converted to calcium oxide which precipitates from the bulk electrolyte. The calcium oxide naturally precipitates downward, as represented in Scheme 1, as it is denser than the carbonate electrolyte. The room temperature density of CaO (3.35 g/cm³) is greater than that of Li₂CO₃ (2.11 g/cm³), 35 Na₂CO₃ (2.54 g/cm³), K₂CO₃ (2.29 g/cm³), or CaCO₃ (2.81 (aragonite) or 2.71 (calcite) g/cm³). However, when oxide is formed by electrolysis in a calcium-containing carbonate electrolyte, the oxide is less soluble and tends to form on the cathode, where at low temperature it will be mixed with the solid carbon product. Starting with lithium oxide in the carbonate electrolyte, and sequentially adding calcium carbonate at the rate at which oxide is formed during the electrolysis, insures bulk, rather than cathode, precipitation of CaO. The calcium oxide 40 product is more readily extracted when it precipitates downward from the bulk electrolyte, rather than when it forms at the cathode.

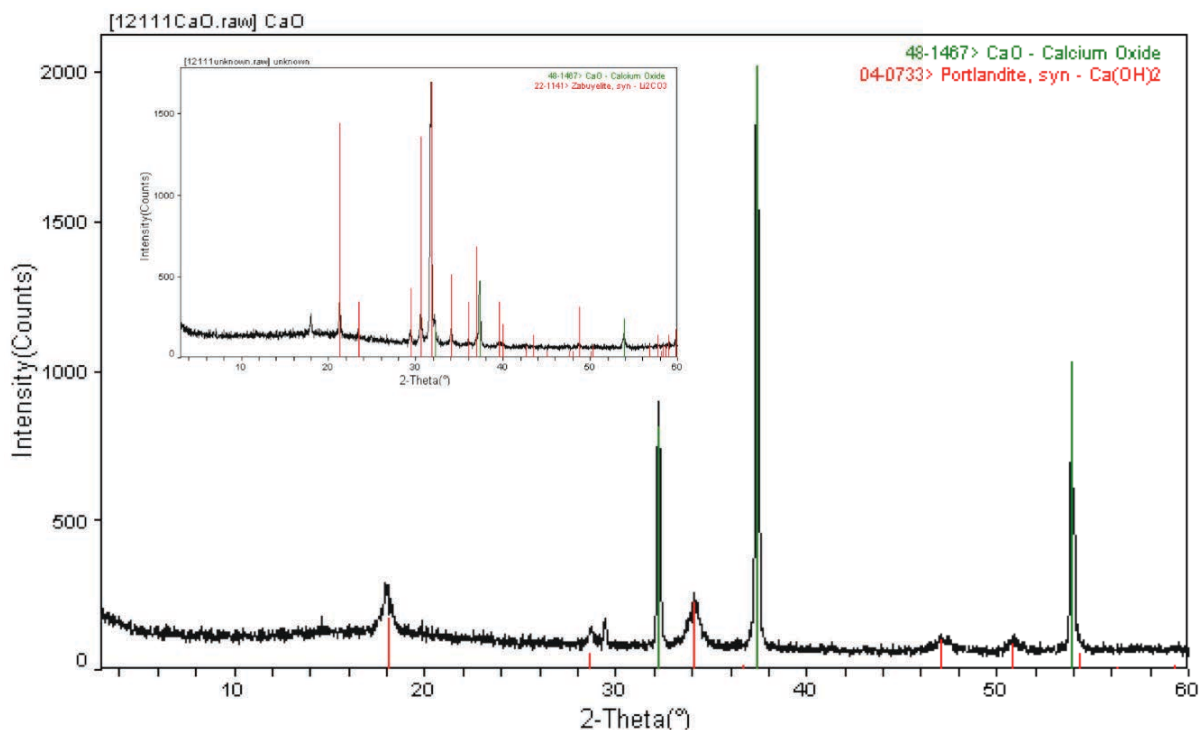


Figure 4. XRD of CaO during bulk electrolysis of carbonate. Inset: CaO STEP product removed nearer to the electrolyte interface additionally carries clean electrolyte (Li_2CO_3), following a 5 hour 1 A electrolysis in 750°C Li_2CO_3 . Library reference spectra for CaO, $\text{Ca}(\text{OH})_2$ and Li_2CO_3 are indicated as vertical lines.

5

As shown by XRD in Figure 4, the CaO precipitating from the bulk electrolyte is highly pure, with some evidences of a small $\text{Ca}(\text{OH})_2$ formation due to air exposure. CaO product removed closer to the molten carbonate interface additionally carries clean electrolyte, Li_2CO_3 as evidenced by XRD in the figure inset. The cathode is steel wire, which has been coiled into a spiral disk. After electrolysis, when the cathode wire is uncoiled at room temperature the carbon product readily drops off the wire for analysis; the steel wire used as the cathode does not exhibit any corrosion. When molten carbonate with dissolved limestone (Li_2CO_3 with CaCO_3) is electrolyzed instead without excess dissolved lithium oxide, the calcium oxide is tends to form near the oxide generating cathode, rather than in the bulk, and for example, can be removed along with the deposited carbon.

15

Analysis of coprecipitated (along with reduced carbon) calcium oxide at the cathode electrolysis is a greater challenge than when calcium oxide is formed in the bulk electrolyte. Even this more challenging analysis is readily accomplished with FTIR. As shown in the upper photograph in the middle of Figure 2, the sample, containing both calcium oxide and solid carbon, is removed as a deposit on the cathode wire along with some frozen electrolyte (in this case lithium carbonate). The sample is removed by uncoiling the wire and analyzed as a pressed KBr pellet. Carbon induces a simple broad general absorption corrected from the FTIR by baseline subtraction. As shown in Figure 5, the resultant FTIR exhibits the strong absorption of CaO. At longer and shorter wavelengths, the broader spectra exhibits the distinctive Li_2CO_3 absorption in the 3645 and 1400 cm^{-1} windows due to the solidified electrolyte, and no absorption in the Li_2O absorption window of 2900 or 3700 cm^{-1} , nor the strong CaCO_3 absorption in the vicinity of 1800 cm^{-1} .

25

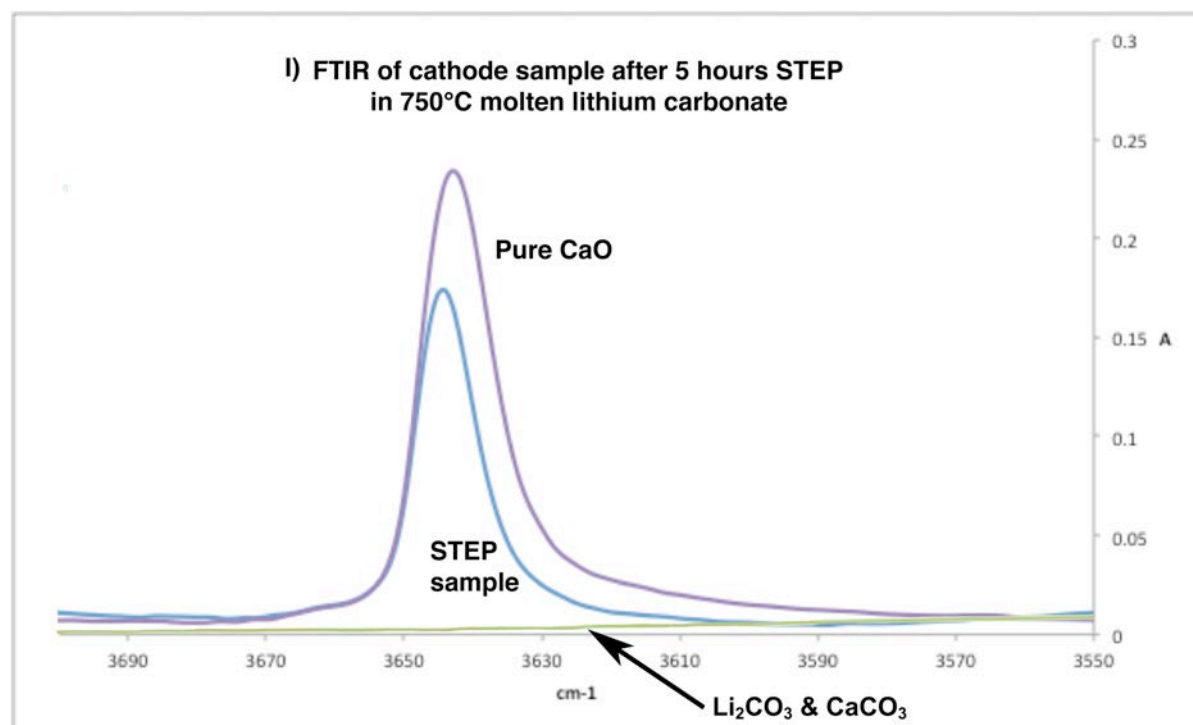


Figure 5. STEP CaO FTIR absorption spectrum of cathode deposited sample following a 5 hour 1 A electrolysis in 750°C Li_2CO_3 , and following base line correction to remove broad band carbon absorption.

5

Economic assessment

Cement production accounts for 5-6% of all anthropogenic carbon dioxide emissions. Society consumes over 3×10^{12} kg of cement annually, and the cement industry releases ~ 9 kg of CO_2 for each 10 kg of cement produced. An alternative to this CO_2 intensive process is needed. The majority of the CO_2 emissions occurs during the decarbonation of calcium carbonate, CaCO_3 , to lime, CaO , $\sim 60\%$ from equation 1 and the remainder from burning fossil fuels, such as coal, to heat the kiln reactors to about 900°C , eq. 2.^{4,26} As with cement production, massive CO_2 emissions are associated with the CaO formed from CaCO_3 for purifying iron and aluminum, for agriculture, glass, paper, sugar, calcium carbide, and acetylene production, to scrub SO_2 from smoke stacks, to soften water or to remove phosphates from sewerage.^{27,28}

15

STEP cement, in addition to forming lime without any emission of carbon dioxide, cogenerates a more valuable product than cement. The solar thermal electrolytically cogenerated product, such as CO , is produced at below current market values, and is in addition to the CaO and O_2 products. The low cost of the cogenerated product is due to the endothermic, reactive nature of the available hot carbonate from the limestone, which as demonstrated in this study, is easily reduced at high activity/low energy in the molten state to carbon or carbon monoxide. CO is an energetic industrial reagent used to produce fuels, purify nickel, and to form plastics and other hydrocarbons.

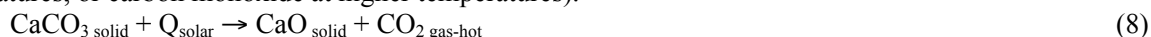
In the STEP cement process, solar thermal energy is used both for the enthalpy of calcium oxide formation from calcium carbonate and to decrease the required electrolysis potential. STEP cement can produce lime at less cost than that of conventional industry cement processes. Approximately 50% of the existing cost of the conventional carbothermal production of lime, that is \$35 per ton, is for energy and \$35 for materials production cost other than energy.^{4,16} The projected cost of the produced calcium oxide is decreased by the value of the byproduct, either solid carbon or CO . For this analysis we explore the low voltage case (0.9 V), which generates the CO product. CO is an energetic industrial reagent used to produce fuels, purify nickel, and to form plastics and other hydrocarbons. Prices for CO are \sim \$600 per ton and vary with purity.²⁹ The CO price is intermediate to

the current value of solid carbon as either coal (\$130 per ton) or graphite (\$2000 per ton). The principal electrolyte Li_2CO_3 is not consumed in the production process, and is readily available (see below). Sodium and potassium carbonates are less expensive alternatives, but require further optimization for STEP cement..

Both STEP and Hy-STEP represent new solar energy conversion processes to produce energetic molecules. Individual components used in the process are rapidly maturing technologies including wind electric, (Barbier 2010) molten carbonate fuel cells (Sunmacher 2007), and solar thermal technologies (BrightSource 2012, AREVA 2012, Siemens 2011, Solar Reserve 2012, Amonix 2012, Energy Innovations 2012, Pitz-Paul 2007).

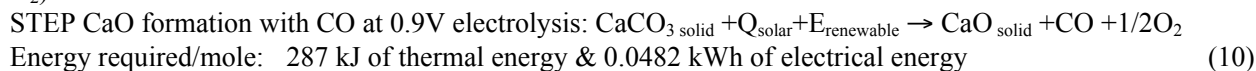
A large scale concentrator solar power (CSP) plant, including the molten salts for heat storage, is in commercial operation,³⁹ albeit for electrical, rather than chemical, production, and others are following,⁴⁰ with a generated electricity cost expected to decrease from its 2010 cost of value of \$0.12 to \$0.09 kWh^{-1} by 2014, and equal to $\$2.5 \times 10^{-5}$ per kJoule.⁴¹ This latter value is the global, cost of CSP generated electrical power including infrastructure, costs of the solar concentration, heat storage and electrical generation. This value decreases to an upper limit of $\$1.2 \times 10^{-5}$ per kJ when the heat energy is intercepted and used prior to the Carnot and friction losses of over 50% which occur in the conventional mechanical turbine of a CSP plant.

For ease of economic assessment an indirect STEP cement configuration is considered in which the same global process is simplified into known and new components. In this alternative configuration, as illustrated in the bottom portion of Scheme 1, concentrated solar thermal heats solid calcium carbonate to over 900°C producing calcium oxide and releasing hot carbon dioxide at $T \sim 900^\circ\text{C}$. As in conventional limestone to lime production, solid CaCO_3 is heated, albeit by solar thermal rather than fossil fuels, and the CaO is extracted as the solid emits hot CO_2 . However in this indirect STEP mode, rather than being released, the hot CO_2 is electrolyzed in molten carbonate to oxygen and a carbon reduction product. The electrolyte is unchanged in the course of the electrolysis, and forms a useful, and/or storable carbon product (solid carbon at lower temperatures, or carbon monoxide at higher temperatures).



Combined, eqs. 8 and 9 yield the same CO_2 -free CaO production as eqs. 3 & 4. The carbonate reduction product, C or CO, is controlled by the composition and temperature of the molten carbonate.

The enthalpy required to produce CaO in equation 8, as calculated by the enthalpy of the individual components is 179 kJ/mole. For the C or CO products, the enthalpy to carbon dioxide splitting, equation 9, is respectively 394 or 283 kJ/mole. The latter is equivalent to 1.47 V, which is the thermoneutral potential. Hence for example, when CO_2 is split to CO by STEP electrolysis at 0.9 V and at 52% solar efficiency as previously described,⁸ an additional $0.57 \text{ V} = 108 \text{ kJ/mole}$ of heat will sustain the process at constant temperature. In this case, the STEP reaction of one mole of CaCO_3 requires 287 (179 + 108) kJ/mole of thermal energy and = 0.0482 kWh (converting 2 Faraday x 0.9V) of electrical energy to cogenerate one mole of CaO and CO (as well as 0.5 moles O_2).



From equation 10, the enthalpy required to drive the formation of 1 ton of CaO (17,832 moles) and 0.50 ton (17,832 moles) of CO, at 0.9V by either the indirect or direct STEP cement process in Scheme 1 is or 5.1×10^6 kJ heat and 860 kWh of electricity. The simultaneous production cost of forming both one ton of CaO and 0.50 ton of CO is the existing \$35 for materials production of lime from limestone, plus the solar thermal heat cost ($5.1 \times 10^6 \text{ kJ heat} \times \$1.2 \times 10^{-5} \text{ per kJ heat} = \61) plus the electricity cost (860 kWh x $\$0.09 \text{ kWh}^{-1} = \77) for a CO production cost of \$173 per ton of CaO produce. The total cost per ton cost of CaO with STEP cement, is decreased by the value added of the CO byproduct.

$$\begin{aligned}\text{CO value generated} &= \text{CO production cost} - \text{CO market value} \\ &= \$173 \text{ per ton of CaO} - 0.50 \text{ ton CO} \times \$600 \text{ ton}^{-1} \text{ CO} \\ &= -\$127 \text{ ton}^{-1} \text{ CaO}\end{aligned}$$

⁵ This negative cost (-\$127 ton⁻¹ CaO) indicates CaO is formed as a free byproduct to the CO product, and the CO is produced at a cost below current market value. This terse analysis is not comprehensive, but is provided as a strong indicator of the cost benefit of STEP cement (even without factoring in the elimination of the carbon dioxide emission). A lower temperature STEP process (<800°C) produces graphite, which is also a valued
¹⁰ added product. This will also decrease the cost of STEP cement, and unlike the higher temperature CO product, can be stored without container as a dense (2.25g/cm³) solid. This terse analysis utilizes the assumption that the electrolysis unit will have a comparable cost to the conventional steam turbine electrical generator and energy distribution system that it replaces in a CSP with molten storage system, and has not included the additional
¹⁵ considerable, societal value that the CaO is generated without CO₂ emission. The coupling of molten salt storage will permit a 24/7 operation that is independent of fluctuations in sunlight or day/night conditions. Related heat, as well as optical, coupling losses will increase system costs, while efficiency improvements, such as textured, higher surface area electrodes to decrease electrolysis voltage will decrease system costs. As previously noted, this STEP technology is applicable also to carbon dioxide utilization (carbon dioxide capture).

²⁰ In summary, STEP cement is based on an unusual technology and new solubility chemistry, is cost effective and is free of CO₂ emissions, with CO or graphite cogenerated at below market cost. A related resource question is whether there is sufficient lithium carbonate, as an electrolyte of choice for the STEP carbon capture process, to produce the global CaO society consumes. Lithium carbonate availability as a global resource has been under recent scrutiny to meet the growing lithium battery market. Lithium carbonate is used,
²⁵ but not consumed in the STEP process (it is not a reoccurring cost). 5x10¹³ moles of CaO annually will require 10¹⁴ Faraday (mole) via STEP cement, or 3x10¹¹ A per year. This requires 0.1 million metric tonnes of lithium carbonate, as calculated from a 2 kg/l density of lithium carbonate, and assuming that improved, rather than flat, morphology electrodes will operate at 3 A/cm² in an 0.5 cm thick cell. Thicker, or lower current density, cells will require proportionally more lithium carbonate. These values are viable within the current production of
³⁰ lithium carbonate. It has been estimated that the current global annual production of 0.13 million tons of LCE (lithium carbonate equivalents) will increase to 0.24 million tons by 2015.⁴² Sodium or potassium carbonates are even more available, but will require further study as STEP cement electrolytes.

³⁵ **Addendum, copied with permission from: S. Licht. *Adv. Mat.* 2011, 47, 5592.**

STEP theoretical background

Light driven water splitting was originally demonstrated with TiO₂ (a semiconductor with a bandgap, E_g > 3.0 eV).⁴³ However, only a small fraction of sunlight has sufficient energy to drive TiO₂ photoexcitation.
⁴⁰ Studies had sought to tune (lower) the semiconductor bandgap to provide a better match to the electrolysis potential.⁴⁴ In 2000, we used external multiple bandgap PVs (photovoltaics) to generate H₂ by splitting water at 18% solar energy conversion efficiency.^{45,46} However, that room temperature process does not take advantage of additional, available thermal energy.

An alternative to tuning a semiconductor bandgap to provide a better match to the solar spectrum, is an
⁴⁵ approach to tune (lower) the electrolysis potential.^{47,48} In 2002 we introduced a photo electrochemical thermal water splitting theory,⁴⁹ which was verified by experiment in 2003, for H₂ generation at over 30% solar energy conversion efficiency, and providing the first experimental demonstration that a semiconductor, such as Si (E_g = 1.1eV), with bandgap lower than the standard water splitting potential (E^o_{H₂O}(25°C) = 1.23 V), can directly drive hydrogen formation.⁴⁷ With increasing temperature, the quantitative decrease in the electrochemical potential to
⁵⁰ split water to hydrogen and oxygen had been well known by the 1950's.^{50,51} As early as 1980 it was noted that thermal energy could decrease the necessary energy for the generation of H₂ by electrolysis.⁵² However, the process combines elements of solid state physics, insolation and electrochemical theory, complicating rigorous theoretical support of the process. Our photo electrochemical thermal water splitting model for solar/H₂ by this

References

12. E. Worrell, L. Price, N. Martin. *Ann. Rev. Energy Environ.* 2001, **26**, 303.
13. T. West, A. McBride. *Agr. Ecosys. Environ.* 2005, **108**, 145.
14. NIST-CHEMWeb Thermochemical Data., *J. Phys. Chem. Ref. Data*, 1998; data interactively
5 available at:
<http://webbook.nist.gov/chemistry/form-ser.html>.
15. Glenn Research Center NASA, *ThermoBuild access to NASA Glenn thermodynamic CEA
database*, 2006; data available at:
<http://www.grc.nasa.gov/WWW/CEAWeb/ceaThermoBuild.htm>
- 10 16. T. Oates, Lime and Limestone, *Kirk-Othmer Enc Chem Tech.*, 1-53, Wiley online library, 2010 as DOI:
10.1002/0471238961.1209130507212019.a01.pub3.
17. K. Tanimoto, *et al.* Cell performance of molten-carbonate fuel-cell with alkali and alkaline-earth carbonate
mixtures. *J. Pow. Sources* 1992, **39**, 285-297.
18. M. Cassir, M. Olivery, V. Albin, B. Malinowska & J. Devynck, J. Thermodynamic and electrochemical
15 behavior of nickel in molten $\text{Li}_2\text{CO}_3\text{-Na}_2\text{CO}_3$ modified by addition of calcium carbonate. *J. Electroanal.
Chem.* 1998, **452**, 127-137.
19. M. Roli, *Bull. Soc. Chim. Fr.*, 1964, 2104.
20. A. Navrotsky, R. Putnam, C. Winbo, & E. Rosen, Thermochemistry of double carbonates in the $\text{K}_2\text{CO}_3\text{-}$
 CaCO_3 system. *Amer. Mineralogist*, 1997, **82**, 546-8.
- 20 21. C. Winbo, E. Rosen & M. Heim, Thermal analytical study of the decomposition of $\text{K}_2\text{Ca}_2(\text{CaO}_3)_3$. *Acta
Chemica Scand.* 1998, **52**, 431-4.
22. A. Cooper, J. Gittins & O. Tuttle, System $\text{Na}_2\text{CO}_3\text{-K}_2\text{CO}_3\text{-CaCO}_3$ at 1 kilobar and its significance in
carbonatite petrogenesis. *Amer. J. Sci.*, 1975, 534-560.
23. S. Frangini & S. Scaccia, Sensitive Determination of Oxygen Solubility in Alkali Carbonate Melts. *J.
25 Electrochem. Soc.*, 2004, **151**, A1251-A1256.
24. JADE, 6.1; Materials Data, Inc: Livermore, CA, 2002.
25. S. Licht, *et al.* Analysis of Ferrate(VI) compounds and Super-Iron Fe(VI) Battery Cathodes. FTIR, XRD,
UV/Vis, ICP, Electrochemical and Chemical, Characterization. *J Power Sources*, 2001, **101**, 167-176.
26. N. Mahasanen, S. Smith & K. Humphreys, "The Cement Industry and Global Climate Change: Current and
30 Potential Future Cement Industry CO_2 Emissions". *Greenhouse Gas Control Technologies – 6th
International Conference*. Oxford: Pergamon. 2003, pp. 995–1000. ISBN 9780080442761. Retrieved 2008-
04-09.
27. Iron and steel, IEA ETASP Tech Brief, 102, May 2010, at:
<http://www.iea-etsap.org/web/E-TechDS/PDF/I02-Iron&Steel-GS-AD-gct.pdf>
- 35 28. T. West & A. McBride, The contribution of agricultural lime to carbon dioxide emissions in the United
States: dissolution, transport, and net emissions. *Agr. Ecosys. Environ.* 2005, **108**, 145-154.
29. C. George, Carbon Monoxide. *Kirk-Othmer Enc Chem Tech.*, 2001, **5**, 1, Wiley online library (2001) as
DOI: 10.1002/0471238961.0301180216090518.a02.pub2
30. E. Barbier, E. How is the global green deal going?. *Nature*, 2010. **464**. 832.
- 40 31. K. Sunmacher, K. *Molten Carbonate Fuel Cells*, 2007. Weinheim: Wiley-VCH.
32. BrightSource. 2012. at: <http://brightsourceenergy.com>
33. AREVA. 2012. at: <http://www.areva.com/EN/solar-220/areva-solar.html>
34. Siemens. 2011. at:
[http://www.siemens.com/press/pool/de/pressemitteilungen/2011/renewable_energy/ERE20110203
7e.pdf](http://www.siemens.com/press/pool/de/pressemitteilungen/2011/renewable_energy/ERE20110203
45 7e.pdf)
35. SolarReserve. 2012. at: <http://www.solarreserve.com/>
36. Amonix. 2012. at: <http://www.amonix.com/>
37. Energy Innovations. 2012. at: <http://www.energyinnovations.com/>
38. R. Pitz -Paal, 2007. High Temperature Solar Concentrators. *Solar Energy Conversion and*

Photoenergy Systems, Eds. Galvez, J. B.; Rodriguez, S. M. Oxford: EOLSS Publishers.

39. Gemasolar, Torresol Energy, Gemasolar CSP at:
<http://www.torresolenergy.com/TORRESOL/Press/gemasolar-wil-be-the-main-project-presented-by-torresol-energy-in-solar-power-internacional-2011>
- 5 40. Brightsource and SolarReserve at CSO at: <http://www.greentechmedia.com/articles/read/brightsource-energy-files-for-250m-ipo-an-analysis/>
41. B. Prior, Cost and LCOE by Generation Technology, 2009-2020, GTM research, Nov. 2011, at:
<http://www.greentechmedia.com/images/wysiwyg/research-blogs/GTM-LCOE-Analysis.pdf>
42. W. Tahil, "The Trouble with Lithium 2; Under the Microscope", 2008, 54 pages, Meridan International
10 Research, Martainsville, France.
43. A. Fujishima, K. Honda, *Nature*, 1972, **238**, 37.
44. Z. Zou, Y. Ye, K. Sayama, H. Arakawa, *Nature*, 2001, **414**, 625.
45. S. Licht, B. Wang, S. Mukerji, T. Soga, M. Umento, H. Tributsh, *J. Phys. Chem. B*, 2000, **104**,
8920.
- 15 46. S. Licht, *J. Phys. Chem. B*, **2001**, *105*, 6281.
47. S. Licht, L. Halperin, M. Kalina, M. Zidman, N. Halperin, *Chem. Comm.* 2003, **2003**, 3006.
48. S. Licht, *Chem. Comm.* 2005, **2005**, 4623.
49. S. Licht, *Electrochem. Comm.* 2002, **4**, 789.
50. A. J. deBethune, T. S. Licht, *J. Electrochem. Soc.*, 1959, **106**, 616.
- 20 51. M. W. Chase; b) *J. Phys. Chem. Ref. Data*, 1998, **9**, 1.
52. J. O'M. Bockris, *Energy Options*, Halsted Press, NY, 1980.
53. S. Licht, *Electrochem. Comm.* 2002, **4**, 789.
54. S. Licht, *J. Phys. Chem. B*, 2003, **107**, 4253.
55. T. S. Light, S. Licht, A. C. Bevilacqua, *Electrochem & Sol State Lett.*, 2005, **8**, E16.
- 25 56. T. S. Light, S. Licht, *Anal. Chem.*, 1987, **59**, 2327.
57. S. Licht, *Anal. Chem.*, 1985, **57**, 514.
58. S. Licht, K. Longo, D. Peramunage, F. Forouzan, *J. Electroanal. Chem.*, 1991, **318**, 119.
59. S. Licht. B. Wang, S. Ghosh, H. Ayub, D. Jiang, J. Ganely, *J. Phys. Chem. Lett.* **2010**, *1*, 2363.
60. R.R. King, D. C. Law, K. M. Edmonson, C. M. Fetzer, G. S. Kinsey, H. Yoon, R. A. Sherif, N. H.
30 Karam, *Appl. Phys. Lett.* **2007**, *90*, 183516.
61. M. Green, K. Emery, Y. Hishikawa, W. Warata, *Prog. Photovoltaics*, **2011**, *19*, 84.
62. S. Licht, B. Wang, H. Wu, *J. Phys. Chem., C* **2011**, *115*, 11803.
63. J. E. Miller, J. E.; Allendorf, M. D.; Diver, R. B.; Evans, L. R.; Siegel, N. P.; Stuecker, J. N. *J. Mat. Sci.* **2008**, *43*, 4714.
- 35 64. *Semiconductor Electrodes and Photoelectrochemistry*, (Ed: S. Licht), Wiley-VCH, Weinheim, Germany **2002**.
65. E. E. Barton, D. M. Rampulla, and A. B. Bocarsly, *J. Am. Chem. Soc.*, **2008**, *130*, 6342.
66. Y. Woolerton, Y., W.; Sheard, S.; Reisner, E.; Pierce, E.; Ragsdale, S. W.; Armstrong, F. A. *J. Amer. Chem. Soc.* **2010**, *132*, 2132.
- 40 67. E. Benson, C. P. Kubiak, A. J, Sathrum, J. M. N. Smieja *Chem. Soc. Rev.* **2009**, *38*, 89.
- 68.

Critical STEP advances for sustainable iron production†

Cite this: *Green Chem.*, 2013, **15**, 881

Baochen Cui and Stuart Licht*

Received 14th October 2012,

Accepted 5th February 2013

DOI: 10.1039/c3gc00018d

www.rsc.org/greenchem

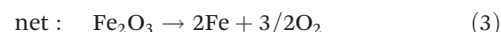
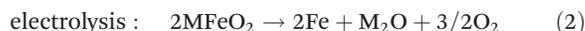
A transformative, sustainable technology to replace the age-old CO₂-intensive production of iron is presented. Molten calcium inclusive carbonates are introduced for STEP Iron. Understanding the speciation constraints permits iron synthesis at nearly 100% coulombic efficiency, without exotic electrocatalysts, and at low electrolysis energy.

There is an urgent need for a material's synthesis to replace the millennia old CO₂-extensive (carbothermal) iron making process. The production of iron and its alloys are one of the top contributors to greenhouse gases (other major contributors are electrical and vehicular power production and cement), and 9 kg of carbon dioxide are emitted for each 10 kg of iron produced. We presented a STEP (Solar Thermal Electrochemical Process) theory of solar energy conversion, building on an alternative theory of solar water splitting, that solar thermal energy could drive endothermic electrochemical reactions (such as the reduction of carbon dioxide) at high solar energy conversion efficiency in molten electrolytes and without carbon dioxide emission.¹ We experimentally demonstrated that STEP can extract graphite from carbon dioxide at solar efficiencies exceeding that of solar cells. STEP has now been applied to a range of useful products including cement, and towards water desalination and water treatment.^{1–3}

In this communication a new, effective molten path for the electrolytic CO₂-free formation of iron is introduced. The electrochemical reduction of iron ore had been investigated in several electrolytes.^{4–9} Each of those electrochemical reductions had physical chemical limitations, such as high energy or corrosivity that, to date, had prevented implementation of an electrochemical replacement to the carbothermal production of iron. Electrolysis of the emitted CO₂ subsequent to iron production has also been considered.^{1,10} Recently, we

presented a molten Li₂CO₃ electrolytic process (STEP) to generate iron without emitting CO₂ and requiring little energy, in mixed alkali and pure lithium molten carbonates.^{1,11} However, a complex, spatially dispersed, electrodeposition occurs near the cathode that includes partially reduced (Fe²⁺) species. This speciation is mapped for the first time in this study. An alternative, carbonate Na_xK_yCO₃ can confine iron to the cathode, but is not “green” corroding anode and cathode and decomposing the carbonate emitting CO₂.¹² Here, this corrosion is eliminated in a new, less alkaline iron splitting electrolyte, in which iron ore is effectively electrolyzed to iron at high efficiency and low energy.

In the prior STEP Iron formation process, an oxide, such as lithium oxide, Li₂O, dissolves the iron oxide, and is regenerated during the electrochemical reduction. Iron oxides were discovered to be unexpectedly, highly soluble in lithiated carbonates.¹ The electrolysis of the iron oxide enriched electrolyte occurs without carbon dioxide release, and without net consumption of the carbonate, such as through the intermediate soluble salt MFeO₂:



Broadening the base of understanding of speciation in the STEP Iron process will be critical to replace a pervasive high carbon footprint industrial process with an effective, low energy CO₂-free alternative. In this communication, we provide (i) the first map of the speciation of the diffuse STEP Iron product, (ii) minimize the energy of the eqn (1)–(3) mechanism, and (iii) demonstrate an alternative synthetic route, which does not produce a spatially diffuse product based on dissolution. The alternative pathway maintains the low carbon footprint, but is based on insoluble iron oxides and produces an iron metal product confined to within the interfacial domain of the cathode, and without release of iron oxide to the bulk electrolyte.

Department of Chemistry, George Washington University, Washington, DC 20052, USA. E-mail: slicht@gwu.edu; Fax: +202-994-5873; Tel: +703-226-8225

† Electronic supplementary information (ESI) available: Expanded introduction, methodology details, and electrochemical parameter optimization for the STEP Iron process. See DOI: 10.1039/c3gc00018d

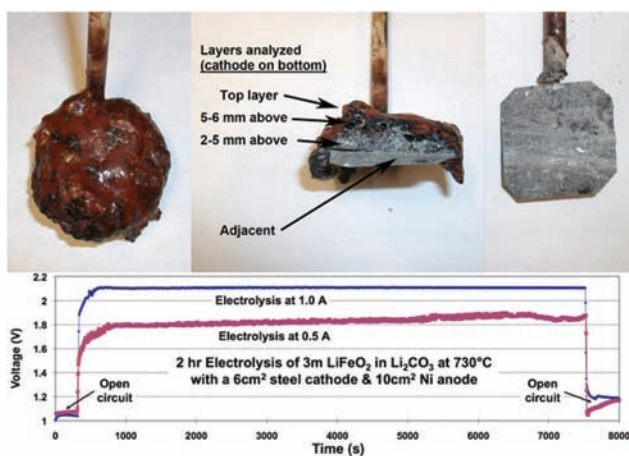


Fig. 1 Middle: Potential during the constant current electrolysis in 730 °C molten Li_2CO_3 containing 3 m LiFeO_2 . Top: Photographs of cathode and product following STEP Iron electrolysis for 2 hours at a constant current of 1 A. Left: cathode subsequent to electrolysis, extraction and cooling. Middle: bare cathode after removal of the product (the product readily peels off the cooled cathode). This reusable cathode consists of 2.5 cm \times 2.5 cm steel. Right: a cut, cross-section view of the product still on the cathode.

The series of photos in Fig. 1 present a STEP Iron electrolysis product, as deposited from molten lithium carbonate onto a planar steel cathode. A reductive bias protects cathodes during STEP Iron electrolysis, and a wide variety of materials (iron, steel, carbon) are effective as cathodes.¹¹ The left photo of Fig. 1 presents a cathode subsequent to electrolysis in molten Li_2CO_3 containing dissolved iron oxide, extraction and cooling. The middle photo shows a cut, cross-section view of the product as removed from the cathode. The product readily peels off the cooled cathode, and the right photo shows the reusable, bare cathode after removal of the product.

The ESI[†] details the iron analyses and electrolysis configuration used.^{13–16} To address the issue of the ratio of the different oxidation states of iron in the electrolysis product several techniques were considered. Techniques such as XPS provide these different oxidation states, but apply to only a small portion of the sample. From a material's perspective this high degree of spatial localization was considered here to leave the interpretation subject to too small a sample (the "trees" rather than "forest" perspective). However, such studies will be valuable in the future. Powder X-ray diffraction was also considered, and was performed on several samples. For example the electrolysis product near lying to the cathode exhibited iron metal 2-theta peaks (at 44.6°) and Li_2CO_3 (at 21.3, 29.4, 30.6, 31.8, 34.2 36.1, 36.9, 43.6, 44.7, and 48.8°). However the technique was considered more time consuming, expensive and less direct than classic quantitative analysis methodologies. This latter method directly probes the oxidation state of the iron species, and had the added advantage that it was conducted in-lab. Hence the classic quantitative analysis technique of precipitation analysis was chosen for this study to provide a complete description of the ferrous, ferric and metallic iron oxidation states as detailed in the ESI.[†]

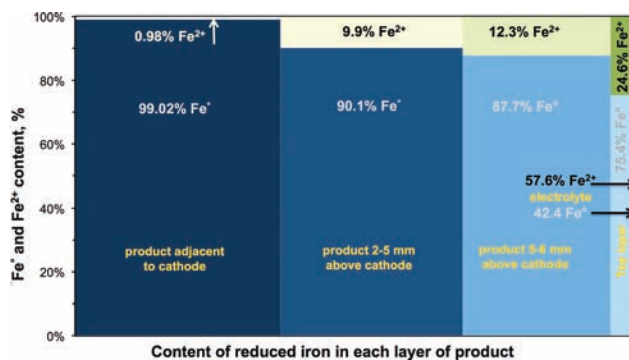


Fig. 2 Cross sectional profile of the reduced iron species analyzed from the layers photographed in Fig. 1, and the electrolyte (right side).

Fig. 2 profiles the measured concentrations of the reduced iron species subsequent to electrolysis. The width reflects the relative total fraction of iron metal found in each layer. The vertical subdivisions of each bar reflect the relative iron oxide concentration that has been reduced to Fe^{2+} or to iron metal. Product closer to the cathode is on the left side, and product further from the cathode is on the right side of the scheme.

The Fig. 2 compositional analysis provides an understanding of each of the layers evident in the photograph of the cathode product. Consistent with the grey-metal color, the dominant iron species in the layer adjacent to the cathode is zero-valent iron. The additional black evident in the next layers is consistent with the color of partially reduced iron oxides, such as ferrous oxide or Fe_3O_4 . The thin, top layer on the product was still molten while the cathode was extracted. The red/brown color of this layer is similar to that of the remaining bulk electrolyte, but still contains a significant (zero valent) iron metal content. Finally furthest from the cathode, the post electrolysis bulk electrolyte also contains zero valent iron (although at a much lower level, less than 1% of that found at the cathode surface), as well as partially reduced (ferrous) iron, and also ferric ion remaining from the initial iron oxide dissolution.

The product speciation profile in Fig. 2 presents the substantial, but incomplete reduction of iron. One objective of this study is the systematic optimization of the STEP Iron to approach 100% coulombic efficiency of the conversion of ferric ion, Fe^{3+} , to iron metal, Fe^0 , and a second objective to accomplish that high coulombic efficiency at low energy (low applied electrolysis potential and high current density). The electrolysis of Fig. 1, is conducted with parallel, horizontal anode and cathode. The nickel oxygen evolving anode is situated near the surface of electrolyte, 1 cm above the cathode. The 10 cm^2 nickel electrode is oversized compared to the 6.2 cm^2 cathode.

The electrolyte composition and temperature, and the electrode configuration, duration and current density have a substantial impact on STEP Iron coulombic efficiency. For example, the electrolysis of Fig. 1 is conducted at 730 °C, near the electrolyte melting point, and a rise in temperature to 850 °C decreases the requisite electrolysis potential but

generates a lower fraction of iron metal. The ESI[†] begins with an electrolysis temperature of 800 °C, and systematically conducts modification of the physical chemical components of the system to understand conditions which increase coulombic efficiency and minimize the requisite electrolysis potential.

Following extensive modification and systematic optimization as delineated in the ESI[†], optimized, high efficiency, low energy electrolyses are measured with an outer foil or wire cylinder pure nickel anode and a small or large diameter inner steel foil cathode. The *coulombic efficiency* compares the applied electrolysis current to the theoretical required for the three electron reduction of Fe³⁺ to iron metal. Efficiency is highest at minimum molten lithium carbonate temperature, intermediate dissolved ferric concentration (3 molal), intermediate cathode and anode current density, anode electron transfer facilitated by situating the anode near the electrolyte//air interface, and or a vertical cathode parallel to a vertical anode. Extended duration electrolyses can be sustained if levels of ferric are not depleted, such as would be achieved *via* continuous addition of ferric oxide during the electrolysis. The electrolysis configuration is simplified when the electrolysis is conducted in a nickel crucible, which comprises both the anode and the cell body in one piece.

The *overpotential* is constrained by the anode current density; energy minimization is achieved with a maximum anode surface area. Interelectrode separations must be small enough (<1 cm) to minimize potential loss at high (>0.1 A cm⁻²) current density. Consistent with the expected Nernst decrease of redox potential with increasing ferric concentration, higher LiFeO₂ (and Li₂O) concentration decreases the electrolysis potential.

As delineated in the ESI[†], optimized electrolyses occur in a low electrolysis potential of 1.35 V and at coulombic efficiency approaching 100%. The energy required to generate a mole of iron is 1.35 V × (3 Faraday/mole Fe) × (26.8 Ah per Faraday) = 109 Wh per mole of iron. This is only approximately 1/3 of the energy required to produce a mole of iron using coke carbon by the conventional carbothermal method (this assumes solar thermal energy is used to maintain the 730 °C STEP Iron electrolysis temperature).

Lithium containing carbonate electrolytes promote soluble iron oxide, as mediated by lithium oxide, eqn (1). The high solubility leads to low energy iron metal electrodeposition, but the iron product can be spatially diffuse. The carbon footprint of molten carbonate electrolytes with less soluble or insoluble is explored here as green, low cost alternatives to a pure lithium carbonate electrolyte. Iron oxide solubility in a molten carbonate electrolyte decreases when there is less lithium present; the solubility of Fe³⁺ in a Li_{0.87}Na_{0.63}K_{0.5}CO₃ eutectic is less than half of its value in Li₂CO₃.¹ Electrolysis of Fe³⁺ dissolved in this eutectic diminishes the secondary Fe²⁺ layer in the product, compared to that in Li₂CO₃, as seen in Fig. 7 of the ESI.[†]

We previously observed that a lithium-free carbonate Na_{1.23}K_{0.77}CO₃ eutectic is corrosive towards the nickel anode, the steel cathode, and the electrolyte, impeding CO₂



Fig. 3 Electrolytic production of iron using solid, rather than dissolved, iron oxide.

electrolysis, and in preliminary results (on CO₂ splitting) observed that CaCO₃ addition is highly stabilizing, sustaining an effective electrolysis of CO₂ to carbon and oxygen.² We attributed the Na_{1.23}K_{0.77}CO₃ corrosivity to the observed high solubility and alkalinity of Na₂O, and the effective electrolysis in Ca_{0.27}Na_{0.7}K_{0.75}CO₃ to the low solubility and alkalinity of CaO.

Here we observe that Fe³⁺ is insoluble (solubility ≪ 0.1 m Fe₂O₃) in both Na_{1.23}K_{0.77}CO₃ and Ca_{0.27}Na_{0.7}K_{0.75}CO₃. We investigate electrolysis of solid Fe₂O₃ pressed onto the cathode as shown on the bottom of Fig. 3. Electrolytic reduction of 2 g of solid Fe₂O₃ (pressed at 6000 psi on each side of a coiled 26.5 cm, 1.2 mm diameter, 10 cm² iron wire, Fig. 3 bottom), then dry annealed at 750 °C for 2 hours, was compared in three molten carbonate electrolytes: pure lithium, a sodium potassium eutectic and a calcium, sodium, potassium eutectic. The previous STEP Iron process using Fe₂O₃ dissolved as LiFeO₂ in Li₂CO₃ is a CO₂-free process.^{11,12} However, the electrolytic reduction of Fe₂O₃ in Na_{1.23}K_{0.77}CO₃ is not “green”. Unlike the Li₂O containing Li₂CO₃ electrolyte, this electrolyte reacts with iron oxide and releases CO₂ in accord with:



Eqn (4) is observable both as a mass loss from the electrolyte, rapid bubble evolution from the cathode, and darkening of the electrolyte during the electrolysis.

Electrolysis in the Ca_{0.27}Na_{0.7}K_{0.75}CO₃ electrolyte decreases the rate of CO₂ emission from the cathode, and results in a high quality iron metal deposit. The observed, qualitative rate of bubble evolution from the immersed cathode during 750 °C electrolysis decreased in the order Li₂CO₃ (vigorous in the absence of dissolved Li₂O) > Na_{1.23}K_{0.77}CO₃ (vigorous) > Ca_{0.27}Na_{0.7}K_{0.75}CO₃ (little, if any bubble

evolution). Similarly as shown on the top of Fig. 3, post electrolysis, the molten calcium-containing electrolyte had not changed color, whereas the Li_2CO_3 electrolyte has turned red due to ferric dissolution (as LiFeO_2), and the $\text{Na}_{1.23}\text{K}_{0.77}\text{CO}_3$ electrolyte has become black. The electrolyte, which solidifies on extraction of the $\text{Ca}_{0.27}\text{Na}_{0.7}\text{K}_{0.75}\text{CO}_3$ electrolysis product, is readily removed by a water wash. The washed metal product seen in Fig. 3, is formed at high coulombic efficiency (98% compared to only 49 or 50% coulombic conversion from Fe_2O_3 in either the Li_2CO_3 , or $\text{Na}_{1.23}\text{K}_{0.77}\text{CO}_3$ during the 2 hour 0.5 amp electrolysis). The nickel oxygen anode, photographed on the top right of Fig. 3 is unaffected by this electrolysis in $\text{Ca}_{0.27}\text{Na}_{0.7}\text{K}_{0.75}\text{CO}_3$.

Finally, although Ca^{2+} added to the $\text{Na}_y\text{K}_z\text{CO}_3$ electrolyte as calcium carbonate, CaCO_3 , suppresses corrosion and CO_2 emission from the cathode, it does not prevent CO_2 emission from another source; that is the decomposition of the carbonate electrolyte, which occurs in accord with the equilibrium:



This final electrolyte decomposition challenge is overcome by the addition of 0.5 m CaO (lime) rather than CaCO_3 (limestone) to the molten carbonate electrolyte, and we observe that both the iron oxide insoluble $\text{CaO}/\text{Na}_y\text{K}_z\text{CO}_3$ and $\text{CaO}/\text{Li}_2\text{CO}_3$ electrolytes, as well as the previous iron oxide soluble $\text{Li}_2\text{O}/\text{Li}_2\text{CO}_3$ electrolyte, provide a high quality iron metal electrolysis product from solid, pressed iron oxide. Added oxide eliminates the carbonate decomposition emission of CO_2 by driving equilibrium 5 to the left. Specifically, we had previously observed that at 750 °C Li_2CO_3 with 3 m Li_2O , absorbs atmospheric CO_2 and gains mass when exposed to air, while without added Li_2O , Li_2CO_3 or $\text{CaCO}_3/\text{Li}_2\text{CO}_3$ both emit CO_2 and lose mass (these effects are quantified and elaborated upon in ref. 2 ESI†).

In summary, the chemistry of a transformative process to decrease greenhouse gas emissions is developed here. High quality, low energy iron metal products are produced by the green electrolysis of iron oxide in molten carbonates and provide an important opportunity to replace the CO_2 intensive-carbothermal production of iron. A calcium-containing electrolyte, $\text{CaO}/\text{Na}_y\text{K}_z\text{CO}_3$, is more effective for iron production than $\text{Na}_y\text{K}_z\text{CO}_3$ from several perspectives, maximizing iron conversion efficiency, minimizing nickel anode corrosion, minimizing dissolution into the electrolyte, and spatially constraining the iron product to the cathode surface. The energy required to produce STEP Iron is only approximately 1/3 of the energy required to produce a mole of iron using coke carbon by the conventional carbothermal method (this assumes solar thermal energy is used to maintain the 730 °C STEP Iron electrolysis temperature). Future studies will probe replacing calcium with barium, which presumably will have similar, less alkaline, advantageous effects on the iron product, and electrolyte and anode stability.

Acknowledgements

We gratefully acknowledge partial support of this research by the US NSF.

Notes and references

- 1 S. Licht, *Adv. Mater.*, 2011, **47**, 5592.
- 2 S. Licht, H. Wu, C. Hettige, B. Wang, J. Lau, J. Asercion and J. Stuart, *Chem. Commun.*, 2012, **48**, 6019; S. Licht, H. Wu, C. Hettige, B. Wang, J. Lau, J. Asercion and J. Stuart, *Chem. Commun.*, 2011, **47**, 3081; S. Licht, H. Wu, C. Hettige, B. Wang, J. Lau, J. Asercion and J. Stuart, *Chem. Commun.*, 2010, **46**, 7004; S. Licht, H. Wu, C. Hettige, B. Wang, J. Lau, J. Asercion and J. Stuart, *Chem. Commun.*, 2005, 4623; S. Licht, H. Wu, C. Hettige, B. Wang, J. Lau, J. Asercion and J. Stuart, *Chem. Commun.*, 2003, 3006; and as related to batteries: S. Licht, H. Wu, C. Hettige, B. Wang, J. Lau, J. Asercion and J. Stuart, *Chem. Commun.*, 2008, 3257; S. Licht, H. Wu, C. Hettige, B. Wang, J. Lau, J. Asercion and J. Stuart, *Chem. Commun.*, 2007, 2753; S. Licht, H. Wu, C. Hettige, B. Wang, J. Lau, J. Asercion and J. Stuart, *Chem. Commun.*, 2006, 4341.
- 3 S. Licht, *J. Phys. Chem. C*, 2009, **35**, 16283; S. Licht, B. Wang and H. Wu, *J. Phys. Chem. C*, 2011, **115**, 11803; S. Licht, *et al.*, *J. Phys. Chem. Lett.*, 2010, **1**, 2363; S. Licht, *et al.*, *Int. J. Hydrogen Energy*, 2010, **35**, 10867; B. Wang, H. Wu, G. Zhang and S. Licht, *ChemSusChem*, 2012, **5**, 2000. The studies date back to the original STEP-like theory on water splitting at: S. Licht, *J. Phys. Chem. B*, 2003, **107**, 4253; S. Licht, *Electrochem. Commun.*, 2002, **4**, 789.
- 4 B. He, R. V. Gudavarthy, J. A. Koza and J. A. Switzer, *J. Am. Chem. Soc.*, 2011, **133**, 12358.
- 5 C. Donath, E. Neacsu and N. Ene, *Rev. Roum. Chim.*, 2011, **56**, 763.
- 6 A. Pal, A. N. Samata and S. Ray, *Hydrometallurgy*, 2010, **105**, 30.
- 7 B. Y. Yuan, O. E. Kongstein, G. M. Haarberg, A. N. Samata and S. Ray, *J. Electrochem. Soc.*, 2009, **156**, D64.
- 8 A. Allanore, H. Lavelaine, J. P. Birat, G. Velentin and F. Lapique, *J. Appl. Electrochem.*, 2010, **40**, 2010.
- 9 E. Mostad, S. Rolseth and J. Thonstad, *Hydrometallurgy*, 2008, **90**, 213.
- 10 A. L. Dipu, J. Ryu and Y. Kato, *ISIJ Int.*, 2012, **52**, 1427.
- 11 S. Licht and H. Wu, *J. Phys. Chem. C*, 2011, **115**, 25138.
- 12 S. Licht, *arXiv* [physics.chem-ph], 2012, *arXiv*: 1209.3512, 1.
- 13 Z. Xu, H. Hwant, R. Greenlund, X. Huang, J. Luo and S. Anshuetz, *J. Miner. Mater. Character. Eng.*, 2003, **2**, 65.
- 14 X. Shi, J. Liao and S. Wang, *Rock Miner. Anal.*, 2009, **28**, 197.
- 15 ASTM designation: D3872-86. Standard Test Method for Ferrous Iron in Iron Oxides. *Annual Book of ASTM Standards*, 1999, 1.
- 16 Y. Gende and O. Lahav, *Appl. Geochem.*, 2008, **23**, 2123.

ELECTRONIC SUPPLEMENTARY INFORMATION FOR PUBLICATION
Critical STEP Advances in the Green Chemistry of Iron Production

Baochen Cui^a and Stuart Licht,^{*a}

^aDepartment of Chemistry, George Washington University, Washington, DC 20052, USA.

CORRESPONDING AUTHOR EMAIL ADDRESS: slicht@gwu.edu

Expanded introduction, methodology details, and electrochemical parameter optimization

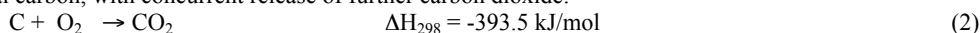
Along with control of fire and the production of cement, the carbothermal reduction of iron is one of the founding technological pillars of civilization. Yet, it is also one of the major global sources of greenhouse gas release, and a CO₂-free process to form this staple is needed. Hematite, Fe₂O₃, and magnetite, Fe₃O₄, are the principal ores currently used for the widespread carbothermal industrial production of iron. Introduced in 2010, STEP Iron produces iron without carbon dioxide emission through a new chemistry consisting of the electrochemical reduction of the unexpected, high solubility of Fe₂O₃ and Fe₃O₄ in molten lithiated carbonates.¹ This electronic supplementary information systematically characterizes the critical electrochemistry of STEP Iron, to provide high coulombic efficiency (approaching a 100% yield of the 3 e⁻ reduction of Fe₂O₃), low electrolysis potential and kinetically facile electron transfer to provide high rate. The electronic supplementary information provides a consistent analytical methodology to access iron purity, as well as specific, useful cathode, anode and electrolyte configurations to sustainably and effectively produce iron without greenhouse gas emissions.

The electrolytic formation of energetic materials dates back to the first splitting of water to hydrogen and oxygen in 1801 and the discovery of the element potassium by Lavoisier in 1807. By the 1900's the decrease in standard electrochemical potential (unit activity) with increasing temperature of a variety of half reactions was well established,^{ESI-1} and by the 1980's investigators such as Bockris^{ESI-2} suggested the use of thermal energy, including via nuclear or solar energy, to decrease the electrolysis potential required to drive water splitting. Solar splitting at elevated temperatures combines elements of solid state physics, insolation (solar radiation reaching a given area) and electrochemical theory, complicating any rigorous theoretical support of the process. In 2002, we derived the first rigorous theory that a solar photon contains sufficient thermal and electronic energy to efficiently split water by electrolysis.^{ESI-3} This led in 2003 to the first experimental demonstration that a single semiconductor with a bandgap of less than the electrochemical potential to split water ($E^\circ_{\text{H}_2\text{O}}(25^\circ\text{C}) = 1.23\text{V}$), such as silicon ($E_{\text{bandgap}} = 1.1\text{V}$), can directly drive solar water splitting (in molten hydroxide) by applying the excess solar thermal energy (not used by the silicon).^{ESI-4} The 2002 theory and experiment was generalized, from water splitting and hydrogen fuel formation, to all endothermic electrochemical processes in 2009 with the acronym STEP.¹

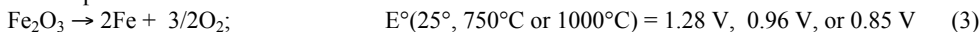
STEP and conventional iron chemistries. Commercial iron today continues to be produced by the millennia old carbothermal process. In the carbothermal process iron oxide is reduced by carbon. The carbothermal process releases the greenhouse gas, CO₂, for example in the 3 electron reduction of Fe(III), accompanied by the 4 electron oxidation of carbon, as illustrated on the left side of Figure 1.



This Fe₂O₃ reduction reaction is endothermic. To sustain this reaction, heat, ΔH, is provided by the burning of over one additional carbon, with concurrent release of further carbon dioxide:



Alternatively, iron oxide can be electrolyzed, producing iron metal and evolving only oxygen, without carbon dioxide release. For example via:



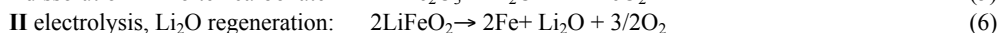
STEP and conventional carbon footprint. No CO₂ is released in this STEP process when the heat and electronic charge is generated by renewable energy (solar, wind, hydro, geothermal) or nuclear energy. Alternatively, we can calculate the CO₂ release when fossil fuels are used to form the electricity. As demonstrated in this study, iron may be formed at an electrolysis potential of as little as 0.9V in molten as Li₂CO₃. In Equation iii, the room temperature rest potential (calculated from the free energy of the reaction) is 1.28 V and the thermoneutral potential (calculated from the enthalpy of the reaction) is 1.43 V. The latter voltage is the energy required to prevent the system from cooling during electrolysis, and unlike the endothermic rest potential, is nearly constant with changing temperature, for example, $E_{\text{thermoneutral}}(1200^\circ\text{C}) = 1.40 \text{ V}$, and from Equation iii requires 6 Faraday per mole of iron. This is equivalent to 0.225 kWh / mol Fe (from F = 96,485 A sec, and 1 kW=1000 VA), and will be less if an alternate heat source is used to maintain the system electrolysis temperature. Currently, fossil fuels release ~11 mol CO₂ / kWh; specifically the natural gas, oil, and coal generation of electricity have respective stack emissions of 7.5, 12 and 15 mol CO₂ / kWh. Hence, even if fossil fuel, rather than renewable energy, is used to generate the heat and electricity and heat for iron by electrolysis, it will only emit 0.225 x 11 = 2.5 CO₂ per Fe generated. This is less than the 7 CO₂ per Fe emitted by the existing iron smelting processes. In summary:

<u>Iron generation Process</u>	<u>CO₂ emitted per Fe generated</u>
conventional smelting	7
new Li ₂ CO ₃ electrolysis powered by fossil fuel electricity	2.5
STEP Li ₂ CO ₃ (solar) electrolysis	0

Eqs. 2 and 3 endothermic, that is the energy (expressed here as the electrochemical potential) required to convert iron oxide to iron decreases with increasing temperature. The range of 500 to 950 °C provides an ideal range for the electrolysis to occur at low potential and without the materials constraints and instabilities imposed by higher temperature operating conditions.

We had recently discovered that the lithiation of iron oxides facilitates their concentrated dissolution in molten carbonates. Both hematite, Fe_2O_3 , and magnetite, Fe_3O_4 , are highly soluble in molten lithiated carbonates.^{1,11} We have observed a high solubility for both lower temperature eutectic carbonate melts ($\text{Li}_{0.87}\text{Na}_{0.63}\text{K}_{0.50}\text{CO}_3$), and for pure Li_2CO_3 , (pure Li_2CO_3 melts at 723°C). In Li_2CO_3 , ferric, [Fe(III)], solubility increases from 7 to 12 molal (molal = m = moles per / kg Li_2CO_3) with temperature increase from 750 to 900°C , while in the eutectic the solubility increases from 1 to 4 m Fe(III) as temperature increases from 550°C to 900°C .

Lithium oxide is not consumed in the iron making process. For Fe_2O_3 in molten carbonate, the STEP iron production mechanism is given by:¹



III net reaction, same as equation 3.

Figure 1 compares conventional carbothermal, and STEP's electrolytic lithiated carbonate production of iron. Iron electrolysis, equations 3 and 4, are endothermic; higher temperature requires significantly less electrolysis energy. As previously studied, in the STEP processes this thermal energy is provided by concentrated sunlight leading to high solar energy conversion efficiencies. The measurements here focus on the electrochemical, rather than solar (which has been previously studied¹), characterization of STEP Iron. A maximum coulombic efficiency, and a minimum electrolysis potential, are critical to the viability of the STEP Iron process, and have not been previously determined. This study probes that critical optimization for the electrolytic synthesis of iron metal from Fe_2O_3 .

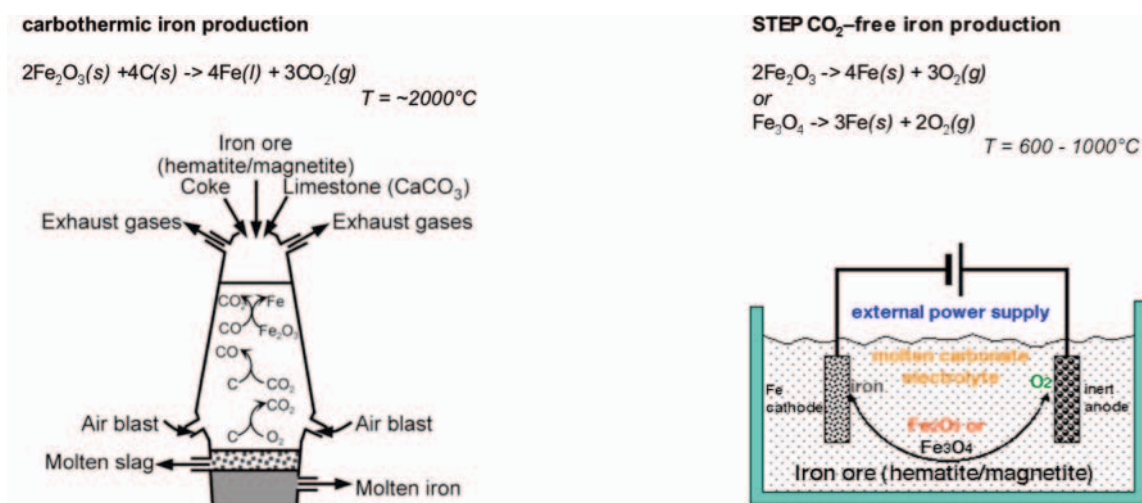


Figure 1. Comparison of the industrial (left) and the STEP CO_2 free production of iron (right).

Experimental

Chemicals and Materials. Lithium carbonate utilized is (Li_2CO_3 , Alfa Aesar, 99%), as well as ferric oxide, Fe_2O_3 (99.4%, JT Baker), Li_2O (Alfa 99.5%), 1mm and 2 mm Ni wire (Alfa 99.5 %) and Ni foil (McMaster pure Ni 200 shim), crucibles: nickel (VWR AA35906-KY), Fe wire (Anchor dark annealed), steel foil (McMaster 75 μm 316 steel), crucibles: nickel (VWR AA35906-KY), high purity alumina (AdValue Technology AL-2100), silicon dioxide (SiO_2 , Spectrum, 325 mesh), lithium orthosilicate is (Li_4SiO_4 , Alfa Aesar, 99.9%), Pflatz & Bauer, 99%).

Electrolyses. Electrolysis conditions and the systematic variation of the electrolysis cell components are described in the Systematic Optimization of electrolytic iron production in molten carbonate section. The theoretical maximum mass of iron that can be produced from the ferric salt during the electrolysis is calculated as Electrolysis current (A) x Electrolysis time (s) x Atomic Weight Fe / (3 e- x 96,485 As).

Analyses. Iron metal is produced by electrolysis in molten carbonate at the cathode. The cathode product is analyzed for iron metal content based on, and improved from the method of Xu and co-workers in which iron metal replaces copper sulfate, and the product ferrous sulfate is analyzed.¹³ The procedure has been further improved by (i) washing the electrolysis product with deionized water, and (ii) replacement of the previous UV/Vis evaluation which was used at the end of the procedure, with a more quantitative (less prone to colorimetric interference) titration by dichromate. The initial rinse removes Li_2CO_3 and Li_2O to prevent reaction of Fe^0 to form $\text{Fe}(\text{OH})_2$ or $\text{Fe}(\text{OH})_3$.

In addition to the relative valence state composition of iron, the mass percent of total iron in the sample (including the solidified electrolyte) is shown in the Fe_{total} of column in Table 1, and the last two columns are measured water soluble and water insoluble mass percent of each sample. The washed, dried insoluble component consists primarily of iron (iron metal and iron oxides). The iron analysis of weighed samples from each layer yields the concentrations: $[\text{Fe}_{\text{total}}]$, $[\text{Fe}^0]$, $[\text{Fe}^{2+}]$, and $[\text{Fe}^{3+}]$ (the latter concentration is determined from the difference of $[\text{Fe}_{\text{total}}] - [\text{Fe}^0] - [\text{Fe}^{2+}]$). A separate, weighed sample from each layer is washed, followed by subtraction of the mass of the dried insoluble (filtered, dried) component. This yields the mass of the remaining soluble components. The water soluble salts components consist of Li_2CO_3 and Li_2O . The Li_2O dissolves as LiOH , including Li_2O stripped from lithiated iron oxides when brought in contact with the wash water (e.g. $\text{LiFeO}_2 + \text{H}_2\text{O}$ liberates soluble LiOH), and the 105°C dried components are weighed as the insoluble salts).

The analysis procedure for iron metal is:

1) The cathode product is ground in a mortar and pestle, until it can be sifted and dispersed through a 70 mesh (212 μm) sieve.

2) The ground product is washed with deionized water, then extracted by suction filtration and rinsing the precipitate with deionized water until pH is near 7. The precipitates, residue and filter paper are collected to react with CuSO_4 .

3) To 0.5 g of the ground product is added 50 ml of 0.5 M CuSO_4 , to form:



4) After boiling this stirred solution for 1 hour, it is immediately filtered (to prevent the reaction of O_2 with Fe^{2+}) with a GF/A (Whatman glass microfiber) filter paper into a 250 ml volumetric flask, and the filter paper is washed with double deionized (18 M Ω) water also into the flask, and diluted to 250 ml.

5) 25 ml of the 250 ml filtrate is sampled by pipette into a 250 ml erlenmeyer flask,

and the following solutions are added to the flask: 20 ml of "A", 20 ml of "B", 50 ml of water, and 3 drops of indicator solution "C", where

A: is a mix of 50 ml of water with 10 ml concentrated H_2SO_4

B: 700 ml of water with 150 ml concentrated H_2SO_4 , 150 ml H_3PO_4 (binds colored Fe^{3+} , which is colored, as colorless $\text{Fe}(\text{HPO}_4)_2^-$, to improve clarity of the endpoint)

C: Is the indicator solution consisting of 0.2% aqueous Diphenylamine 4-sulfonic acid sodium salt

D: Is the titrant consisting of 0.004167 M (6 x dilution of 0.025 M) $\text{K}_2\text{Cr}_2\text{O}_7$

which titrates as 1 equivalent $\text{K}_2\text{Cr}_2\text{O}_7$ per FeSO_4 ; each ml of solution D = 1.3962 mg of Fe° metal.

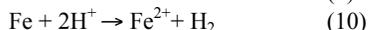
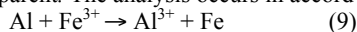


The endpoint is observed as a color change from light blue (initial) to the endpoint's purple.

This titration analysis is also confirmed by weighing the mass of magnetically removed the iron product that was washed & dried to remove oxide. The reliability of the analysis during the titration is improved when solutions are stirred slowly in step 2, rather than rapidly, to prevent significant errors (underestimating the Fe° content of the product with increasing speed of stirring) due to the introduction of oxygen, which can convert ferrous to ferric prior to the titration. The need to switch to a lower stirring speed for the Fe° analysis was discovered and applied to the latter half of the experiments in this study. Under this latter condition replicate analyses of Fe° metal mass from are reproducible to within a $\pm 2\%$.

The analysis procedure for total Fe is:

In accord with the method of Shi et al,¹⁴ a 0.1g sample was placed in a 250 ml flask with the addition of 20 ml of 1:1 diluted HCl. The sample was placed on a mixer hot plate at about 90 °C (to prevent volatile loss of FeCl_3 at higher temperature) until completely dissolved. 20 ml water was added under N_2 (99.999%). Al powder was added in three 0.1 g portions (in large excess of the theoretical amount to reduce Fe^{3+} to Fe^{2+}). With a minimum of stirring, the Al quickly reacts with Fe^{3+} and H^+ to form Al^{3+} , and Fe^{3+} was reduced to Fe^{2+} . A color change from yellow to light yellow was observed until the solution was transparent. The analysis occurs in accord with the following equations:



100 ml of H_2O was added and the solution was cooled until room temperature. 20 ml sulfuric-phosphoric acid solution and 5 drops of the diphenylamine indicator where added after which the solution was titrated with the standard $\text{K}_2\text{Cr}_2\text{O}_7$ solution (0.0250 mol 1/6 $\text{K}_2\text{Cr}_2\text{O}_7/\text{L}$).

$$\text{Total Fe}^{3+} (\%) = V \times N \times \text{FW Fe} \div 1000/S$$

V-- standard $\text{K}_2\text{Cr}_2\text{O}_7$ solution volume, ml.

N-- standard $\text{K}_2\text{Cr}_2\text{O}_7$ solution concentration, mol/L.

FW Fe = 55.85 g/ mol.

S—specimen weight, g.

The analysis procedure for Fe^{2+} is based on the method of reference 14, as modified by references 13 and 15. In this analysis, 0.5 g of the sample to be analyzed was added to 250 ml flask and 20 ml of 1:1 diluted HCl was added. This solution was mixed on a hot plate under 99.999% N_2 at 90 °C until completely dissolved. 100 ml H_2O was added and the solution allowed to cool to room temperature. 20 ml sulfuric-phosphoric acid solution (prep: add 600 ml concentrated H_2SO_4 to 800 ml stirred DI, then add 600 ml of 86% phosphoric acid) and 5 drops of the diphenylamine indicator were added and titrated with the standard $\text{K}_2\text{Cr}_2\text{O}_7$ solution (0.0250 mol 1/6 $\text{K}_2\text{Cr}_2\text{O}_7/\text{L}$) to a sharp endpoint color change from green to purple.

In accord with the equation:

$$\text{Fe}^{2+} (\%) = V \times N \times \text{FW Fe} \div 1000/S.$$

V-- standard $\text{K}_2\text{Cr}_2\text{O}_7$ solution volume, ml.

N-- standard $\text{K}_2\text{Cr}_2\text{O}_7$ solution concentration, mol/L.

S—specimen weight, g.

The analysis procedure for Fe^{3+} is the straightforward difference from the known total iron, the sum of the iron metal and ferrous species as: $\text{Fe}^{3+} (\%) = \text{Total Fe} (\%) - \text{Fe}^\circ (\%) - \text{Fe}^{2+} (\%)$

The analysis procedure for the aqueous soluble components:

Filters were dried in an oven at 105 °C for 1 hour, and then cooled in a desiccator, and weighed. After weighing, samples (~0.3g) to be analyzed were stirred one hour in 100 ml of DI (18 M Ω) in a 250 ml flask at room temperature, then filtered using suction, and the filtrate washed on the filter with three 20 mL volumes of DI water. The filter is transferred onto a glass weighing dish, and dried 105°C for a minimum of 1 hour until a minimum mass is measured (after cooling to room temperature in the desiccator).

Equation: Water soluble substances (wt%) = (A-B) \square 100/A.

A—Specimen weight, g.

B-- Residue on the filter paper weight, g.

Systematic Optimization of electrolytic iron production in molten carbonate.

A systematic, variation of molten iron electrolysis can yield efficient iron production efficiency at low energy. General conditions of the first series of electrolyses are summarized in Table 1. The cathode in this first series of experiments is a thin planar 6.25 cm² steel sheet. This cathode lies under the anode, and we observe that the iron product is deposited on top of the cathode. This cathode surface is the active area exposed to short ion diffusion path between the electrodes.

Table 2 summarizes the results of 1 hour electrolyses at 1 Amp in an 800°C molten lithium carbonate electrolyte containing 1.5 m Fe₂O₃ and 3 m Li₂O (to generate 3 m LiFeO₂ in solution). In this series of experiments the anode, a coiled pure nickel (McMaster 200 Ni) wire is situated 3 mm below the surface of the electrolyte to facilitate oxygen evolution in an attempt to minimize oxygen interaction with the cathode product.

Table 1. Constant characteristics in the first series of STEP Iron parametric optimization studies.

Current of electrolysis	1.0 amp
Time of electrolysis (1h)	3600 s
Theoretical max mass Fe ⁰ from electrolysis: Fe ³⁺ +3e ⁻ → Fe ⁰	1A□3600□96485□3□55.85 = 0.696 g
Anode: Ni wire tightly coiled, l = 16 cm, d = 2.0 mm, area:	10 cm ²
Cathode: Steel shim, 2.5cm□2.5cm, area	6.25 cm ²



Figure 2. Anode (upper electrode) and cathode (lower electrode) prior to electrolysis (top) and following electrolysis prior to removal of cathode product (bottom). Insulating alumina ceramic tubes are reused and hence appear charred.

In the first series of experiments, summarized in Table 2, the anode to interelectrode spacing is varied, and the mass of electrolyte was changed to cover smaller or larger inter-electrode separations. The electrodes before and after electrolysis are photographed in Figure 2. The lithium based electrolyte is highly conductive, and even at these relatively high current densities, electrolytic resistance losses are not significantly impacted by the variation of inter-electrode spacing. The electrolysis potentials at 1 A constant current are the same to within 0.1 V, independent of the 0.25 to 2.0 cm electrode separation. Coulombic efficiency, particularly during the 0.25 cm separation electrolysis may have been impacted by shorting as the iron deposit growing from the cathode approached the anode, and that a maximum of over 50% coulombic efficiency is achieved for an intermediate spacing of 1.0 cm.

Table 3 summarizes STEP Iron electrolyses in which the starting concentration of Li₂O is varied. In each case, the initial ferric concentration (as added Fe₂O₃) is kept constant at

3 molal Fe³⁺ in Li₂CO₃. As we have previously demonstrated, Fe₂O₃ is not soluble in carbonate unless Li₂O is added, and reacts to form LiFeO₂ in the molten solution.¹ The Li₂O is not consumed in the electrolysis process. That is consistent with eq. 7, as LiFeO₂ is reduced to form iron metal, Li₂O is liberated to dissolve the next iteration of added iron ore (Fe₂O₃). As seen in the photo in Figure 3, the iron is deposited directly on top of the cathode, followed by a black layer of partially reduced iron (magnetite), followed by a layer of the electrolyte containing the excess (brown) Fe₂O₃ dissolved in the electrolyte. The iron layer is easily separated from the cathode, Figure 4, and as seen in Figures 3 and 4 leaves behind a reusable cathode. As seen in Table 3, a 1:1 ratio of Li₂O to Fe₂O₃ supports the maximum coulombic efficiency, although it is interesting to note in Figure 5, that higher concentrations of Li₂O significantly decrease the required electrolysis potential (as seen comparing the 1.5 m and 9.0 m Li₂O electrolysis). This decrease in potential with increasing oxide concentration may be due to the formation of a peroxide intermediate in the anodic evolution of oxygen as we have recently demonstrated.¹¹ Also evident in the figure, potential variations are occasionally observed during individual electrolyses, although average electrolysis potential trends are highly consistent.

Table 2. Effect of electrode spacing and electrolyte mass on electrolysis. Electrodes are delineated in Table 1. The electrolyte mass was changed as indicated below, to maintain electrolyte coverage in experiments with smaller or larger inter-electrode separations. Note, coulombic efficiency, particularly during the 0.25 separation electrolysis may have been impacted by shorting as the iron deposit grew from the cathode towards the anode.

Temperature (°C)	800	800	800	800
Anode/Cathode separation (cm)	0.25	0.5	1.0	2.0
Electrolyte Total mass (g): Electrolyte weighed from a mix of 200.0015g Li ₂ CO ₃ , 47.8888g Fe ₂ O ₃ and 17.9286g Li ₂ O,	8.3193	16.6128	33.2174	66.4510

Fe ³⁺ concentration (mol /kg Li ₂ CO ₃) as Fe ₂ O ₃	3.0 m	3.0 m	3.0 m	3.0 m
Li ₂ O concentration (mol /kg Li ₂ CO ₃)	3.0 m	3.0 m	3.0 m	3.0 m
Cathode: Steel shim, 2.5cm□2.5cm	6.25 cm ²	6.25 cm ²	6.25 cm ²	6.25 cm ²
Fe ⁰ mass in product (g)	0.135	0.328	0.381	0.249
Coulombic efficiency (100%x Fe ⁰ mass experiment/theory)	19.4	47.0	54.7	35.7

The next series of experiments utilizes the general conditions described in Table 2, still at constant (1.0 amps) current, but varies the electrolysis time. As summarized in Table 4, whereas 1 hour of electrolysis should theoretically yield 0.7 g of iron (assuming 1000% coulombic efficiency of the three electron reduction of dissolved Fe³⁺), 8 hours of electrolysis would be expected to generate 5.6 g of iron metal. As summarized in Table 4, the experimental coulombic efficiency during electrolysis is approximately 50 percent and is not substantially affected by the electrolysis time. What is affected, as shown in the photos in Figure 6, is the amount of salt that is removed with the product, and is enriched 5-fold in iron metal after the extended electrolysis. The amount of salt accompanying the cathode product is seen to be much lower after 8h electrolysis than after 1 hour electrolysis. In each case, the cathode product is washed prior to the iron(0) content analysis. Even subsequent to extended electrolysis time, each of the cathodes remain intact after the removal of product. As seen in Figure 6, the 8 hour electrolysis cathode product does not exhibit the multiple layers evident, and instead has iron metal throughout the product (but the iron remains spatially diffuse intermingled with electrolyte).

Table 3. Effect of Li₂O concentration on electrolysis. The anode/cathode separation is 1.0 cm; other electrolysis conditions are detailed in Table 1. Note, an intermediate Li₂O concentration (2 molal) conducted for double the electrolysis time, generated greater iron metal product.

Temperature (°C)	800	800	800	800
Time of electrolysis (h) at 1.0 amp	1h	2h	1h	1h
Theoretical max mass Fe ⁰ from electrolysis: Fe ³⁺ + 3e ⁻ → Fe ⁰	0.696 g	1.389 g	0.696 g	0.696 g
Average Potential of electrolysis (V)	1.84	1.80	1.69	1.57
Carbonate Electrolyte: Li ₂ CO ₃ (g)	25.000	25.001	24.992	21.999
Fe ³⁺ concentration (mol /kg Li ₂ CO ₃)	3.0 m	3.0 m	3.0 m	3.0 m
Fe ₂ O ₃ mass (g)	5.9866	5.9868	5.9843	5.9167
Li ₂ O concentration (mol /kg Li ₂ CO ₃)	1.5 m	2.0 m	3.0 m	9.0 m
Li ₂ O mass (g)	1.1200	1.4941	2.241	5.9167
Electrolyte Total Weight (g)	32.1138	32.4217	33.2174	33.1841
Fe ⁰ mass in product (g)	0.312	0.711	0.381	0.155
Coulombic efficiency (100%x Fe ⁰ mass exper/theory)	44.8	51.7	54.7	22.3

Figure 3. Side view of cathode with product.

Figure 4. Cathodes, after removal of product, remain intact.

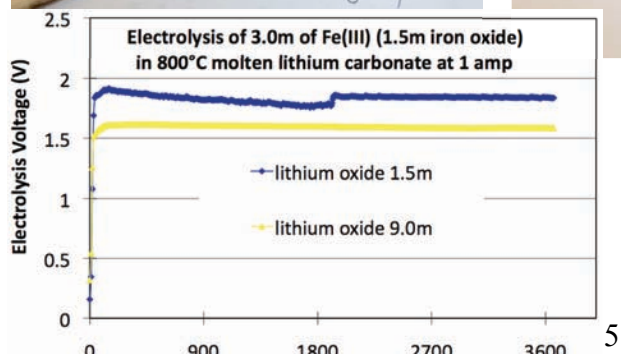
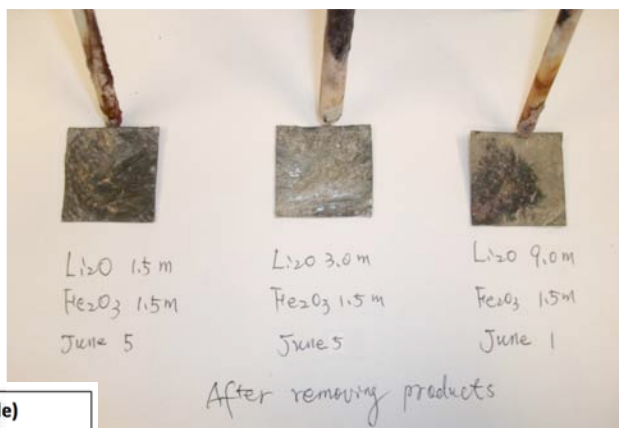


Figure 5. Variation of STEP Iron electrolysis potential with different Li₂O concentrations.

Sodium carbonates (mp 851°C) or potassium carbonate (mp 891°C) both have higher melting points than lithium carbonate (mp 723°C). However, a eutectic mix of the three carbonates, such as $\text{Li}_{0.85}\text{Na}_{0.61}\text{K}_{0.54}\text{CO}_3$, has melting point below 400°C, and provides an opportunity to explore STEP Iron at lower temperatures. At these lower temperature conditions, the electrolysis potential would be expected to be considerably higher. As previously shown the reaction of iron oxide to iron and oxygen is endothermic, with (i) an increase in rest potential with decrease in temperature. This will be exacerbated by (ii) a lower solubility of iron oxide in the eutectic at lower temperature and with lower lithium ion content, and (iii) higher overpotential due to the higher electrolyte resistance of a mixed alkali, compared to pure lithium, electrolyte. The general conditions of electrolysis are similar to those in Table 1. At the lower 500°C temperature, only a lower concentration of iron oxide could be dissolved in the eutectic and the sustainable current at a reasonable electrolysis potential was only, 0.4 A, rather than 1A. Hence, the electrolysis time was increased from 1 to 2.5 hours to provide a constant total current during the experiment. As summarized in Table 5, even at the lower current, the lower temperature still requires a high (3.5V) average electrolysis potential, and results in a poor coulombic efficiency. As seen in Table 5, by 750°C, the $\text{Li}_{0.85}\text{Na}_{0.61}\text{K}_{0.54}\text{CO}_3$ eutectic could readily accommodate the full 3 molal Fe^{3+} used in the pure lithium carbonate electrolyte at 800C. It is evident in the figure that in the eutectic at 750C, a higher electrolysis potentials was needed to accommodate the same 1 Amp current used in the pure lithium electrolyte. Interestingly, coulombic efficiencies are high in both cases, and as seen in Figure 7, the cathode product contains a low fraction of removed salt, and a high fraction of iron.

Table 4. Effect of electrolysis time on the electrolytic formation iron. The anode/cathode separation is 1.0 cm; other electrolysis conditions are detailed in Table 1.

Temperature (°C)	800	800	800	800	800
Time of electrolysis (h) at 1.0 amp	<i>1h</i>	<i>1h 20m</i>	<i>2h</i>	<i>4h</i>	<i>8h</i>
Theoretical max mass Fe^0 via: $\text{Fe}^{3+} + 3\text{e}^- \rightarrow \text{Fe}^0$	0.696 g	0.926 g	1.389 g	2.778 g	5.557 g
Average Potential of electrolysis (V)	1.69	1.75	1.57	1.7	1.65
Fe^{3+} concentration (mol /kg Li_2CO_3) as Fe_2O_3	3.0 m	3.0 m	3.0 m	3.0 m	3.0 m
Li_2O concentration (mol /kg Li_2CO_3)	3.0 m	3.0 m	3.0 m	3.0 m	3.0 m
Electrolyte Total Weight (g)	33.2174	33.0001	33.2163	33.2143	33.2177
Fe^0 mass in product (g)	0.381	0.529	0.732	1.493	2.553
Coulombic efficiency (100% \times Fe^0 mass exp/theory)	54.7	57.1	52.7	53.7	45.9
* = anode contact broke just prior to completion		*	*		



Figure 6. Product removed and partially peeled from cathode after 1 or 8 hour electrolyses. The amount of salt removed with the product is high after 1h electrolysis (then washed prior to analysis) & lower after the extended (8h) electrolysis. During the 8h electrolysis, a higher fraction of the initial 3 m of Fe^{3+} is converted to Fe^0 & the product layer sitting on the cathode is enriched in iron metal.



Figure 7. (right) Side view of cathode with product after 1h 3 m LiFeO_2 in $\text{Li}_{0.85}\text{Na}_{0.61}\text{K}_{0.54}\text{CO}_3$ 750°C STEP iron electrolysis.

Table 5. Effect of eutectic ($\text{Li}_x\text{Na}_y\text{K}_z\text{CO}_3$) or pure (Li_2CO_3) carbonate, and of temperature, on the electrolytic formation iron. The electrodes are separated by 1.0 cm and are detailed in Table 1.

Temperature (°C)	500	750	800
Time of electrolysis (h)	<i>2.5h</i>	<i>1h</i>	<i>1h</i>
Electrolysis current (A)	0.4	1.0	1.0
Average Potential of electrolysis (V)	3.5	1.95	1.69
Carbonate Electrolyte	$\text{Li}_{0.85}\text{Na}_{0.61}\text{K}_{0.54}\text{CO}_3$	$\text{Li}_{0.85}\text{Na}_{0.61}\text{K}_{0.54}\text{CO}_3$	Li_2CO_3
Carbonate Electrolyte: Li_2CO_3 (g)	30.0026	25.0002	24.9926
Fe^{3+} concentration (mol /kg Li_2CO_3)	0.8 m	3.0 m	3.0 m
Fe_2O_3 weight (g)	1.9156	5.9861	5.9843
Li_2O concentration (mol /kg Li_2CO_3)	0.8 m	3.0 m	3.0 m
Li_2O weight (g)	0.7177	2.2416	2.241
Electrolyte Total Weight (g)	32.6468	33.2349	33.2174
Fe^0 mass in product (g)	0.026	0.388	0.381
Coulombic efficiency (100% \times Fe^0 mass exp/theory)	3.73	55.8	54.7

Table 6. Effect of planar foil cathode surface area on the electrolytic formation iron. The electrolysis time, current, theoretical maximum mass of iron, and anode are as detailed in Table 1. Inter-electrode separation is 1.0 cm. Cathodes are described in the table.

Temperature (°C)	800	800	800	800
Average Potential of electrolysis (V)	1.66	1.68	1.69	1.43
Electrolyte Total Weight (g): Electrolyte weighed from a mix of 200.0015g Li ₂ CO ₃ , 47.8888g Fe ₂ O ₃ and 17.9286g Li ₂ O, Fe ³⁺ concentration (mol/kg Li ₂ CO ₃) as Fe ₂ O ₃	33.2161	33.2093	33.2174	33.281
Li ₂ O concentration (mol/kg Li ₂ CO ₃)	3.0 m	3.0 m	3.0 m	3.0 m
Cathode: Steel shim, 2.5cm□2.5cm	0.8 cm ²	2.5 cm ²	6.25 cm ²	12.5 cm ²
Fe ⁰ mass in product (g)	0.238	0.325	0.381	0.191
Coulombic efficiency (100%× Fe ⁰ weight experiment/theory)	34.2	46.7	54.7	27.5

Table 6 summarizes interesting, but unsuccessful, attempts to improve the coulombic efficiency of the planar iron foil cathode, by increasing or decreasing its surface area. As seen in Figure 8, two smaller surface area electrodes were compared, as well as a double surface area electrode folded in an accordion configuration to accommodate the double width of the electrode. As summarized in Table 6, while the larger surface area electrode did decrease the average electrolysis potential, the coulombic efficiency was maximum for the simpler planar, solid cathode. As in prior experiments, the anode was a Ni coil, 16 cm length, 2.0 mm diameter, area 10 cm², and the anode/cathode inter-electrode separation was 1 cm.



Figure 8 (left). Solid steel foil cathodes with various surface areas prior to electrolysis (top) and following electrolysis with partial removal of cathode product (bottom). Spot welds to connect the steel wire contacts are evident.

Figure 9. The 6.25 cm² foil, and 5 or 20 cm² coiled wire, cathodes prior to electrolysis.

Table 7 summarizes a successful attempt to modify the cathode configuration, which is accomplished by transitioning from a planar, to a coiled, steel cathode. Figure 9 compares the planar and coiled cathode configurations. Not shown is the similar, intermediate 10 cm² coil, which appears to combine the advantages of a loose coil packing with a relatively high surface. Interpolating between the coulombic efficiencies of the 5 or 10 cm² coiled cathodes, it can be noted that the 6.25 cm² foil cathode exhibits similar efficiencies to the same surface area coiled wire electrode. A common impurity in iron ores is silicate. Another change in this experiment was addition of 10%, by mass, lithium silicate as an initial attempt to simulate the electrolysis of iron ore with silicate. As seen comparing Tables 6 and 7, the silicate marginally diminishes the coulombic efficiency at the planar, foil electrode to 51%. However, the coulombic efficiency at the 10 cm² coiled steel wire cathode is higher at 55%.

Table 7. Effect of cathode shape and current density (determined by cathode surface area) on the electrolytic formation of iron. The anode, with an anode/cathode separation of 1.0 cm is detailed in Table 1. Cathodes are described in the table. Each electrolysis is at 1 A for 2 hours.

Temperature (°C)	800	800	800	800
Average Potential of electrolysis (V)	1.636	1.759	1.787	1.738
Carbonate Electrolyte: Li ₂ CO ₃ (g)	25.0	25.0	25.0	25.0
Fe ³⁺ concentration (mol/kg Li ₂ CO ₃)	3.0	3.0	3.0	3.0
Fe ₂ O ₃ weight (g)	5.9885	5.9886	5.9880	5.9883
Li ₄ SiO ₄ (g) (10 wt % SiO ₂ content in Fe ₂ O ₃)	1.194	1.194	1.194	1.194
Electrolyte Total Weight (g)	33.9996	34.0005	34.4254	34.0002

Cathode: Area (cm ²)	6.25	5.0	10.0	20.0
Size: Length□width or diameter (cm)	2.5□2.5	13.3□0.12	26.5□0.12	53□0.12
Shape: foil or coiled wire	Fe foil	Fe wire	Fe wire	Fe wire
Current density (mA/cm ²)	160	200	100	50
Fe ⁰ mass in product (g)	0.7049	0.2994	0.7693	0.6350
Coulombic efficiency (100%× Fe ⁰ weight experiment/theory)	51%	22%	55%	46%

In the absence of silicate, the improvement in coulombic efficiency with the larger surface area coiled, rather than smaller surface area planar, cathode is more evident. Table 8 summarizes results of electrolyses each using a 10 cm² coiled cathode, and with either 2, 3, 4 or 6 molal Fe³⁺, and Li₂O in 800°C molten lithium carbonate. The coulombic efficiency is high and comparable in the 3 and 4 molal electrolytes, with the 3 molal exhibiting a modestly higher efficiency of 70%. In the presence of 10% silicate, as seen in Table 9, and continuing with use of the preferred coiled cathode, the coulombic efficiency is somewhat higher in the 3, rather than 2, molal Fe³⁺, and higher when a 1:1 equivalent ratio, rather than a 2:1 equivalent ratio of Li₂O is used. In all cases the presence of the silicate decreases the measured coulombic efficiency.

Table 8. Effect of Fe₂O₃ concentration on the electrolytic formation iron. The anode is as detailed in Table 2, with an anode/cathode separation of 1.0 cm. Cathodes are described in the table. Each electrolysis is at 1 A for 1 hour.

Temperature (°C)	800	800	800	800
Average Potential of electrolysis (V)	1.6645	1.826	1.847	1.584
Carbonate Electrolyte: Li ₂ CO ₃ (g)	26.9996	25.0006	23.0006	21.0003
Fe ³⁺ concentration (mol /kg Li ₂ CO ₃)	2.0	3.0	4.0	6.0
Fe ₂ O ₃ weight (g)	4.3117	5.9881	7.3460	10.0603
Li ₂ O concentration (mol /kg Li ₂ CO ₃)	2.0	3.0	4.0	6.0
Li ₂ O weight (g)	1.6134	2.2413	2.7485	3.7643
Electrolyte Total Weight (g)	32.9352	33.2002	33.0226	34.8159
Cathode: Fe coil, 26.5 cm length, 1.2 mm diameter, area	10 cm ²	10 cm ²	10 cm ²	10 cm ²
Fe ⁰ mass in product (g)	0.7229	0.9710	0.9496	0.4111
Coulombic efficiency (100%× Fe ⁰ weight experiment/theory)	52%	70%	68%	30%



Figure 10. Left: 10 cm² coiled steel foil cathodes removed after the electrolyses described in Table 8. Right: removed, then ground product, prior to washing from the electrodes picture on the left side.

Table 9. Effect of Fe₂O₃ concentration in an electrolyte containing dissolved silicate (10 wt % SiO₂ content in Fe₂O₃), on the electrolytic formation of iron. The anode is as detailed in Table 1, with an anode/cathode separation of 1.0 cm. Cathodes are described in the table. Each electrolysis is at 1 A for 2 hours.

Temperature (°C)	800	800	800	800
Average Potential of electrolysis (V)	1.639	1.791	1.791	1.745
Carbonate Electrolyte: Li ₂ CO ₃ (g)	26.9992	24.9994	22.9998	20.9994
Fe ³⁺ concentration (mol /kg Li ₂ CO ₃)	2	3	2	3
Fe ₂ O ₃ mass (g)	4.3115	5.9886	7.3468	10.0603
Li ₂ O concentration (mol /kg Li ₂ CO ₃)	2	3	4	6
Li ₂ O weight (g)	1.6132	2.2411	2.7485	3.7648
Li ₄ SiO ₄ (g) (10 wt % SiO ₂ content in Fe ₂ O ₃)	0.8605	1.1942	1.4659	2.0068
Electrolyte Total Weight (g)	33.7870	34.4254	34.5667	36.8151

Cathode: Fe coil, 26.5 cm length, 1.2 mm diameter, area	10 cm ²	10 cm ²	10 cm ²	10 cm ²
Fe ⁰ mass in product (g)	0.6708	0.7693	0.4784	0.5899
Coulombic efficiency (100% \times Fe ⁰ weight experiment/theory)	48%	55%	34%	42%

Table 10 summarizes probes of the temperature effect on STEP Iron electrolysis in a pure lithium carbonate electrolyte (but containing silicate, and 3 molal Fe³⁺ and Li₂O). While the electrolysis potential decreases with increasing temperature, the electrolysis efficiency is lowest (23%) at the highest, 900°C, temperature, and highest (58%) at the lowest, 750°C, electrolysis temperature. The lower efficiencies, at higher temperature, may be associated with the greater reactivity and diffusivity of the oxygen produced at the anode, which can back react with iron to form a parasitic iron oxide loss. Table 11 further probes of silicate effect on STEP Iron. We had previously studied the dissolution of silica, SiO₂, as Li₄SiO₄ in molten carbonates.¹¹ Here, we see the trend that higher SiO₂ ranging from 10 to 30% (added as a percentage of the iron oxide mass to simulate an impurity in the iron ore), tends to decrease the average electrolysis potential, but also decreases the coulombic efficiency of iron production.

Table 10. Effect of temperature on the 1 A, 2 hour electrolytic formation iron (with silicate in electrolyte). The anode, detailed in Table 2, is separated from the cathode by 1.0 cm.

Temperature (°C)	750	800	900
Average Potential of electrolysis (V)	1.801	1.788	1.522
Carbonate Electrolyte: Li ₂ CO ₃ (g)	25	25	25
Fe ³⁺ concentration (mol /kg Li ₂ CO ₃)	3	3	3
Li ₂ O concentration (mol /kg Li ₂ CO ₃)	3	3	3
Li ₄ SiO ₄ (g)	1.194	1.194	1.194
Electrolyte Total Weight (g)	33.9999	34.4254	33.9998
Cathode: Fe coil, 26.5 cm length, 1.2 mm diameter, area	10 cm ²	10 cm ²	10 cm ²
Fe ⁰ mass in product (g)	0.8067	0.7693	0.3183
Coulombic efficiency (100% \times Fe ⁰ weight experiment/theory)	58%	55%	23%

Table 11. Effect of SiO₂ content on the 1 A, 2 hour electrolytic formation iron. Anode/cathode separation is 1.0 cm; anode as detailed in Table 1.

Temperature (°C)	800	800	800
Average Potential of electrolysis (V)	1.794	1.812	1.672
Carbonate Electrolyte: Li ₂ CO ₃ (g)	24.9994	25.0000	24.9996
Fe ³⁺ concentration (mol /kg Li ₂ CO ₃)	3	3.0	3.0
Fe ₂ O ₃ weight (g)	5.9886	5.9880	5.9883
Li ₂ O concentration (mol /kg Li ₂ CO ₃)	3.0	3.0	3.0
Li ₂ O weight (g)	2.2411	2.241	2.2410
Li ₄ SiO ₄ (g) = Fe ₂ O ₃ weight \square SiO ₂ content \square 60.08 (SiO ₂) \square 119.84 (Li ₄ SiO ₄)	1.1942	1.7940	3.5883
SiO ₂ content in Fe ₂ O ₃ (wt %)	10%	15%	30%
Cathode: Fe coil, 26.5 cm length, 1.2 mm diameter, area	10 cm ²	10 cm ²	10 cm ²
Fe ⁰ mass in product (g)	0.7693	0.7282	0.5668
Coulombic efficiency (100% \times Fe ⁰ weight experiment/theory)	55%	52%	41%

In the next series of experiments the anode stability was improved by raising the anode, from 3 mm below the electrolyte surface (a configuration used in all prior experiments), up to the surface of electrolyte. Prior to this surface anode configuration, anodes occasionally spontaneously broke during the course of the electrolysis. However the surface anodes appear to be fully stable, that is, there is no case of anode discontinuity occurring with the surface anodes in the next 30 experiments, independent of electrolysis conditions, and the anode always appeared to be unaffected by the electrolysis (no corrosion was evident).

Table 12. Effect of surface area of the anode, when situated at the surface (the interface between the molten electrolyte and the gas above the melt), on the 1 A, 2 hour electrolytic formation iron. Anode and cathode are detailed below in the table.

Temperature (°C)	800	800	800	800	800
------------------	-----	-----	-----	-----	-----

Anode: Ni wire, 2.0 mm diameter, length: surface area: coil configuration:	2 cm	8 cm	16 cm	16 cm	30 cm
	1.3 cm ²	5 cm²	10 cm²	10 cm²	18.8 cm²
	tight	tight	tight	loose	tight
Cathode: Fe coil, l = 26.5 cm, d = 1.2 mm, area:	10 cm ²	10 cm ²	10 cm ²	10 cm ²	10 cm ²
Average Potential of electrolysis (V)	1.96	1.91	1.89	1.83	1.66
Fe ³⁺ concentration (mol /kg Li ₂ CO ₃) as Fe ₂ O ₃	3.0 m	3.0 m	3.0 m	3.0 m	3.0 m
Li ₂ O concentration (mol /kg Li ₂ CO ₃)	3.0 m	3.0 m	3.0 m	3.0 m	3.0 m
Electrolyte total mass (g)	33.2176	33.2167	33.2172	33.2172	33.2161
Li ₄ SiO ₄ (g)	0	0	0	0	0
Fe ⁰ mass in product (g)	0.490	0.826	0.808	0.563	0.655
Coulombic efficiency (100% \times Fe ⁰ mass exp/theory)	35.2	59.3	58.0	40.4	47.0

In Table 12 two anode parameters are varied, the surface area, and whether the anode wire is loosely or tightly coiled, as illustrated in the photographs of Figure 11. As seen in Table 12, the electrolysis potential decreases with increasing anode surface area, and its overpotential decreases by 300 mV as the surface area is increased from 1.3 to 19 cm². With the exception of the largest anode surface cell (which may be an outlier and exhibited an unstable electrolysis potential), the coulombic efficiency increases with increasing anode surface area, and the tightly coiled anode configuration leads to higher efficiency than the loosely coiled anode configuration. Finally, the surface anode in Table 12, while more stable, operates at lower coulombic efficiency than its 10 cm² tightly coiled counterpart in Table 9.



Figure 11. Coiled nickel wire anodes with a tight or loose (open) prior to the Table 12 electrolyses.

Table 13 presents the effect of the gas above the electrolysis on the iron production, when the gas is changed from either air, to carbon dioxide, or to nitrogen. It is seen here that nitrogen significantly lowers the electrolysis potential and that both N₂ or CO₂ can improve the coulombic efficiency. As previously shown,¹ pure CO₂ will be absorbed in the electrolyte according to the back reaction of the lithium carbonate decomposition/reformation equilibrium. Air contains (0.03%) CO₂, and molten situated Li₂CO₃ below a blanket of air will be relatively stable, while pure N₂, without CO₂, will slowly decompose in accord with the equilibrium equation: Li₂CO₃ → CO₂ + Li₂O. Nitrogen above the electrolysis is seen to decrease the electrolysis potential, and has only a marginal impact on coulombic efficiency. As also summarized in Table 13, additional Li₂O added to the molten lithium carbonate electrolyte (above 3 m) decreases coulombic efficiency, but sustains the electrolysis at a lower potential.

Table 13. Effect of the gas above the melt, and the Li₂O concentration, on the electrolytic 1A, 2 hour formation of iron.

Temperature (°C)	800	800	800	800	800
Gas above electrolyte	air	air	CO₂	N₂	air
Anode: Ni wire, 2.0 mm diameter, length: surface area: coil configuration:	16 cm	16 cm	16 cm	16 cm	16 cm
	10 cm ²	10 cm ²	10 cm ²	10 cm ²	10 cm ²
	tight	tight	tight	tight	tight
Cathode: Fe coil, l = 26.5 cm, d = 1.2 mm, area:	10 cm ²	10 cm ²	10 cm ²	10 cm ²	10 cm ²
Average Potential of electrolysis (V)	1.87	1.80	1.95	1.62	1.71
Fe ³⁺ concentration (mol /kg Li ₂ CO ₃) as Fe ₂ O ₃	3.0 m	3.0 m	3.0 m	3.0 m	3.0 m
Li ₂ O concentration (mol /kg Li ₂ CO ₃)	2.0 m	3.0 m	3.0 m	3.0 m	4.0 m
Electrolyte total mass (g)	32.5140	33.2172	33.2153	33.2131	33.9994
Fe ⁰ mass in product (g)	0.880	0.808	0.871	0.833	0.708
Coulombic efficiency (100% \times Fe ⁰ mass exp/theory)	63.17	58.0	62.5	62.8	50.8

Lowering the electrolysis temperature and decreasing the cathode current density can improve coulombic efficiency. As seen in Table 14, the coulombic efficiency is increased by over 20%, that is to ~85%, by simultaneously decreasing the electrolysis temperature from 800°C to 750°C, and/or by increasing the cathode surface area. This is not observed when the temperature is held constant and the cathode surface area is decreased to 7.5 cm². Table 14 onward, are presented in an

abbreviated format, without the electrolyte concentration to save manuscript space. In each case the electrolyte total mass is ~ 33 g. In each case the electrolyte is 3.0 m in Fe³⁺ and Li₂O and without silicates. The coulombic efficiency also depends on when the electrode is removed from the electrolysis chamber (electrolysis time, Table 15) and the electrolysis current (Table 16). As seen in Table 15, removing the electrode after, 1 hour negatively impacts the efficiency, although this effect presumably may be mitigated if iron oxide is fed into the electrolysis chamber as iron is produced.

Table 14. Effect of the decrease in temperature and variation in cathode surface area on the 1A, 2 hour electrolytic formation of iron with coiled iron cathodes. The electrolyte is 3.0 m in Fe³⁺ and Li₂O.

Temperature (°C)	750	750	750	800
Gas above electrolyte	N ₂	N ₂	N ₂	N ₂
Anode: Ni wire, d = 2.0 mm, l = 16 cm, coil, area:	10 cm ²	10 cm ²	10 cm ²	10 cm ²
Cathode: Fe coil, 1.2 mm diameter, length: surface area:	20 cm	26.5 cm	33 cm	26.5 cm
	7.5 cm ²	10 cm ²	12.5 cm ²	10 cm ²
Average Potential of electrolysis (V)	1.90	2.1	2.0	1.62
Coulombic efficiency (100%x Fe ⁰ mass exp/theory)	75.4	86.7	84.7	62.8

Table 15. Effect of the electrolysis time in a lower temperature (750 °C) lithium carbonate electrolyte on the electrolytic formation iron with coiled iron cathodes. The electrolyte is 3.0 m in Fe³⁺ and Li₂O.

Temperature (°C)	750	750	750	750
Gas above electrolyte	N ₂	N ₂	N ₂	N ₂
Anode: Ni wire, d = 2.0 mm, l = 16 cm, coil, area:	10 cm ²	10 cm ²	10 cm ²	10 cm ²
Cathode: Fe coil, l = 26.5 cm, d = 1.2 mm, area:	10 cm ²	10 cm ²	10 cm ²	10 cm ²
Time of electrolysis (h) at 1.0 amp	1h	2h	3h	4h
Coulombic efficiency (100%x Fe ⁰ mass exp/theory)	79.6	86.7	69.6	57.4

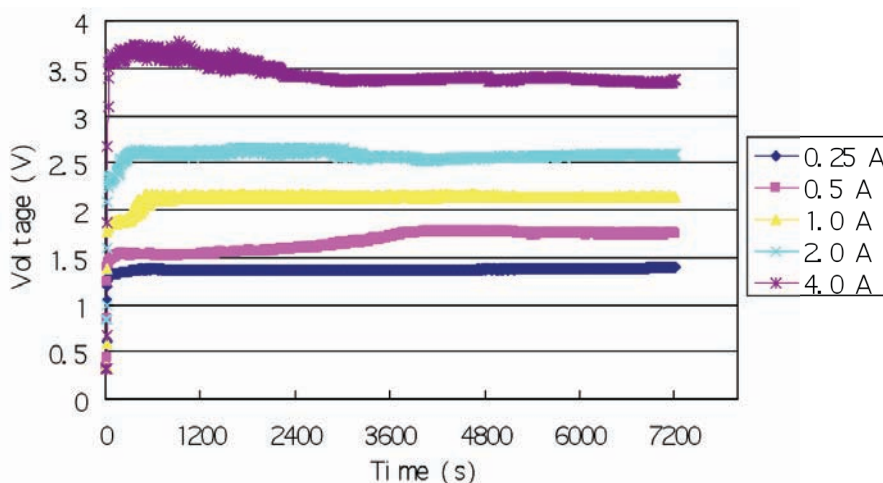


Figure 12. Variation of STEP Iron electrolysis potential with electrolysis current in a lower temperature (750 °C) lithium carbonate electrolyte.

Current density, Table 16, substantially effects the electrolysis with a maximum coulombic efficiency of 93% observed at 0.5 A, and as seen in Figure 12, a substantial decrease of the electrolysis potential at lower currents; a lowering of 2 volts between the electrolyses at 4.0 A compared to 0.25 A. A further increase in coulombic efficiency of the electrolytic formation of iron at 1 A occurs at even lower temperature, 730°C in Table 17. This temperature approaches the 723°C melting point of pure Li₂CO₃. While the efficiency falls rapidly at high temperature, the electrolysis potential is lower as seen in Figure 13. Electrolyte decomposition (from lithium carbonate to lithium oxide and carbon dioxide) occurs more rapidly at higher temperature. There is little decomposition at 750°C,² and the decomposition which occurred at higher temperature may be controlled or eliminated by increasing the lithium oxide concentration within the electrolyte, or increasing the concentration of carbon dioxide in the atmosphere above the electrolysis. Hence, flowing air (0.03% CO₂), rather than nitrogen (0% CO₂), above the electrolysis will decrease the rate of electrolyte loss at higher temperature, even though as seen in Table 17, this nitrogen may marginally improve the coulombic efficiency compared to the electrolysis in air.

Table 16. Effect of the electrolysis current in a lower temperature (750 °C) lithium carbonate electrolyte on the electrolytic formation iron with coiled iron cathodes. Electrolyte is 3.0 m in Fe³⁺ and Li₂O.

Temperature (°C)	750	750	750	750	750
Gas above electrolyte	N ₂				
Anode: Ni wire, d = 2.0 mm, l = 16 cm, coil, area:	10 cm ²				

Cathode: Fe coil, l = 26.5 cm, d = 1.2 mm, area:	10 cm ²				
Electrolysis current (A) during a 2 hour electrolysis	0.25	0.5	1.0	2.0	4.0
Coulombic efficiency (100% x Fe ⁰ mass exp/theory)	53.7	93.1	86.7	50.3	25.6

Table 17. Effect of the electrolysis temperature in a lithium carbonate electrolyte on the electrolytic formation iron with coiled horizontal nickel anodes and coiled wire iron cathodes. 1A, 2 hour electrolyses. Electrolyte is 3.0 m in Fe³⁺ and Li₂O.

Temperature (°C)	730	750	750	800	850
Gas above electrolyte	N ₂	N ₂	air	air	air
Anode: Ni wire, d = 2.0 mm, l = 16 cm, coil, area:	10 cm ²				
Cathode: Fe coil, l = 26.5 cm, d = 1.2 mm, area:	10 cm ²				
Coulombic efficiency (100% x Fe ⁰ mass exp/theory)	89.9	86.7	84.7	58.0	34.5

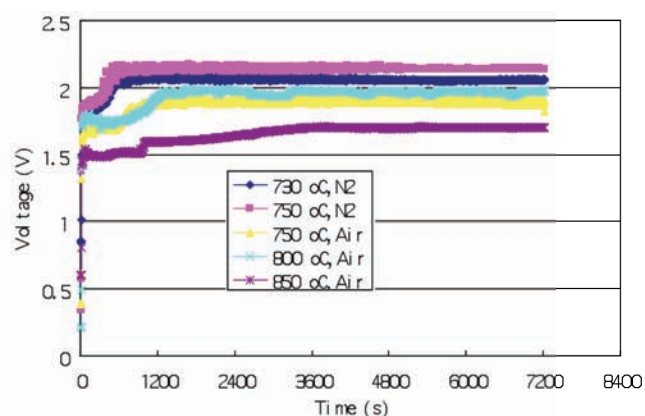


Figure 13. Variation of STEP Iron electrolysis potential at 1.0 A with electrolysis temperature lithium carbonate electrolyte. Electrolyses are conducted either under air or under nitrogen, as indicated on the figure.

Table 18 includes even higher coulombic efficiency STEP iron configurations. The first column contains the same anode on the surface separated by 1 cm from a cathode near the bottom of the cell. As seen in the second column, the use of a smaller (half) diameter nickel or iron wire for the anode and cathode decreases, rather than increases, the coulombic efficiency. We had been working under the hypothesis that hot oxygen would be

deleterious to the metallic iron product. Hence, we had previously configured the anode above the cathode to allow gas to evolve without contacting the iron. Interestingly, in Table 18, at the lower temperature of 730°C in molten lithium carbonate, an opposite, inverted electrode configurations is not only functional, but can exhibit both improved coulombic efficiency and lower electrolysis potential. The coulombic efficiency of these inverted cells is at least 94 to 95% (and this may be considered a lower limit if any iron metal drops into the electrolyte during the cathode removal).

Photos of a vertical cathode inside the anode configuration are presented in Fig. 14. The potential during electrolysis of these inverted electrode configurations is presented in Figure 15. The random oscillations during the cathode on top configuration may be related to a temporary partial blockage of the cathode as anode gas evolved below, passes through this upper electrode. Electrolyte is 3.0 m in Fe³⁺ and Li₂O.

Table 18. Effect of the cathode location in molten 730°C lithium carbonate on the electrolytic formation iron. Electrolyte is 3.0 m in Fe³⁺ and Li₂O.

Temperature (°C)	730	730	730	730
Gas above electrolyte	N ₂	N ₂	N ₂	air
Time of electrolysis (h) at 1.0 amp	2h	2h	1h	1h
Cathode, tight coiled steel wire: Area (cm ²)	10 cm ²	10 cm ²	10 cm ²	10 cm ²
Size: Length □ or diameter (cm)	26.5x0.12	53x0.06	26.5x0.12	26.5x0.12
Coil shape: horizontal (plate) or vertical (cylinder)	plate	plate	plate	vertical
Cathode above, below, or inside the anode	below	below	above	inside
Anode: Ni coiled wire: Area (cm ²)	10 cm ²	10 cm ²	10 cm ²	10 cm ²
Size: wire length □ diameter (cm), prior to coiling	16x0.20	32x0.10	16x0.20	16x0.20
Coil shape: horizontal (plate) or vertical (cylinder)	plate	plate	plate	cylinder
Anode above, below, or outside the cathode	above	above	below	outside
Average Potential of electrolysis (V)	1.87	1.80	1.62	1.95
Coulombic efficiency (100% x Fe ⁰ mass exp/theory)	89.9	71.8	94.4	94.8



Figure 14. Vertical cylindrical configured electrodes used in the molten 730°C lithium carbonate electrolysis in which the cathode was placed inside the anode. Left, middle and right-hand photos respectively show the electrodes prior to the electrolysis, after electrolysis and after removal from the electrolyte, and finally after separation of the cathode from the anode.

The ongoing series of STEP Iron electrode electrolyses are each at 730°C, for 2 hours, but are conducted at 0.5, rather than 1.0 A, to probe a path to lower electrolysis potentials, while preserving, or further increasing, the high coulombic efficiencies of iron production. Photographs of these electrodes with various surface areas of the inner, vertical cathode and outer anode coiled electrodes are shown in Figure 17. As seen compared to Figure 15, in Fig. 16, the lower current substantially decreases the electrolysis potential, and as seen in Table 19, retains over 90% the coulombic efficiency. For the same 0.5 A current, a substantially larger surface area electrodes (20 cm² cathodes and 40 cm² anodes, providing lower current density conditions), lowers the electrolysis potential to less than 1.4 V as seen in Fig. 16, but also decreases the coulombic efficiency in the last column of Table 19.

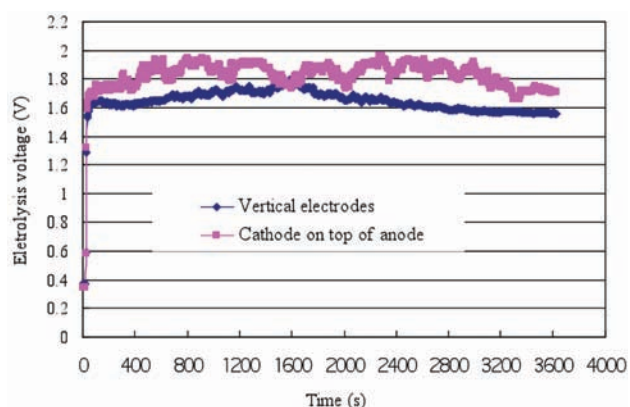


Figure 15 (left). Variation of STEP Iron electrolysis potential in a 730°C lithium carbonate electrolyte using the alternate vertical or inverted anode/cathode configurations.

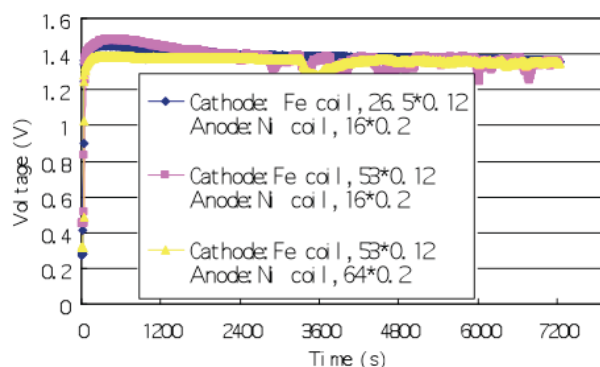


Figure 16 (right). Variation of STEP Iron electrolysis potential in a 730°C lithium carbonate electrolyte using the vertical, inner coiled, cathode configuration with different electrode surface areas.



Figure 17. Vertical cylindrical configured, coiled electrodes with surface area varied by changing the length and coil diameter of the Ni (outer anode) or steel (inner cathode) wire as used in the molten 730°C lithium carbonate electrolysis.

Table 19. For the vertical anode situated outside the cathode configuration, the effect of current and electrode area on the iron formation in molten 730°C Li₂CO₃ containing 3.0 m Fe³⁺ and Li₂O.

Temperature (°C)	730	730	730
Gas above electrolyte	air	N ₂	N ₂
Current & time of electrolysis	1.0A, 1h	0.5A, 2h	0.5A, 2h
Cathode, tight coiled steel wire: Area (cm ²)	10 cm ²	10 cm ²	20 cm ²
Size: Length □ or diameter (cm)	26.5x0.12	26.5x0.12	53.5x0.12
Coil shape: vertical (cylinder), inside the anode			
Anode: Ni coiled wire: Area (cm ²)	10 cm ²	10 cm ²	40 cm ²
Size: wire length □ diameter (cm), prior to coiling	16x0.20	16x0.20	64x0.20
Coil shape: vertical (cylinder), outside the cathode			
Coulombic efficiency (100%x Fe ⁰ mass exp/theory)	94.8	91.2	72.8

In an attempt to further prevent any parasitic reaction of the anode and cathode products, the next configuration, places an alumina tube between the outer (anode) and inner vertical, coiled electrodes. This configuration is photographed in Figure 18, and although the average electrolysis potential is high at 1.98 V, as seen in the second column of Table 20, the efficiency does improve. A return to the horizontal, coiled anode (above the cathode and with an alumina separator) retains very high coulombic efficiencies but creates high electrolysis potential. Compared to an average of 1.4 V electrolysis in the Figure 17

series of experiments, the next two electrolyses occur at an average, higher electrolysis potentials of 1.81V and 1.78 V respectively. In each case a 10 cm² cathode has a horizontal configuration and is located below the coiled, horizontal anode. The first utilizes the coiled steel wire and the second a coiled shim (4.8 x 0.65 cm foil) steel cathode. Reflecting the high coulombic efficiencies summarized in the last two columns of Table 18, the high iron content of the product is evident, in Figure 19 both at the (uncoiled) shim cathode and still coiled wire cathode. An alternative, horizontal reticulated) Ni anode (consisting of a square 6.25 cm² area, 0.33 cm thick Ni sponge) above a vertical cathode supported electrolysis at an intermediate potential of 1.51 V. An expanded study of this latter anode, with high surface area morphology, will be presented at a future date.



Figure 18 (left). Configuration: outer Ni anode is alumina tube shielded & inside is the coiled steel wire cathode.

Figure 19. Photo of the high iron content at the (uncoiled) shim and still coiled wire cathodes after removal from the electrolytes summarized in

the last two columns of Table 19 in the molten 730°C lithium carbonate, electrolytic production of iron.

Table 20. The vertical anode inside anode configuration: effect of area and planar versus wire cathodes on the electrolytic formation of iron in molten 730°C Li₂CO₃ with 3.0 m Fe³⁺ and Li₂O.

Temperature (°C)	730	730	730	730
Gas above electrolyte	N ₂	N ₂	N ₂	N ₂
Current & time of electrolysis (0.5A, 2h	0.5A, 2h	0.5A, 2h	0.5A, 2h
Cathode, tight coiled steel wire: Area (cm ²)	10 cm ²	7.5 cm²	6.25 cm²	10 cm²
Wire or shim (foil)	wire	wire in tube (Fig. 18)	shim	wire
Size: Length □ wire diameter or shim height (cm)	26.5x0.12	20x0.12	4.8x0.65	26.5x0.12
Coil shape: horizontal (plate) or vertical (cylinder)	vertical	horizontal	vertical	vertical coil id x h: 1.3x0.65
Wire Cathode above, below, or inside the anode	inside	below	below	below
Anode: Ni coiled wire: Area (cm ²)	10 cm ²	5.7 cm²	10 cm²	10 cm²
Size: Length □ diameter (cm)	16x0.20	9x0.20	32x0.10	32x0.10
Coil shape: horizontal (plate) or vertical (cylinder)	cylinder	coil	horizontal	horizontal
Anode above, below, or outside the cathode	outside	outside	above	above
Coulombic effic. (100%x Fe ⁰ mass exp/theory)	91.2	96.3	98.0	98.6

Further increases in coulombic efficiency and decrease in the energy needed to drive the STEP Iron are achieved with relatively small changes to the cathode. As seen in Table 21, replacement of the vertical inner coiled wire cathode with a similar shaped, steel shim (foil) cathode increases the coulombic efficiency. Furthermore, an increase in anode surface area (40 cm², compared to the 10 cm² in the first column of Table 20), decreases the electrolysis potential to 1.4 V. Further increases in the cathode diameter of these shim electrodes, with or without a “bottom” on the cathode (as pictured in Figure 20), decrease the electrolysis potential to less than 1.4 V (Figure 21), but, perhaps as a result of the increasing proximity of the anode, results in a decrease in the coulombic efficiency (Table 21). The time variation of the electrolysis potential for the high coulombic efficiency is presented in Figure 21 and compared to similar configurations for the production of iron at 730°C in lithium carbonate containing 1.5 m in Fe₂O₃ and Li₂O.

Table 21. The vertical anode inside anode configuration: effect of electrode shape and area on the electrolytic formation iron at 730°C in molten Li₂CO₃ containing 3.0 m Fe³⁺ and Li₂O.

Temperature (°C)	730	730	730	730	730
Gas above electrolyte	N ₂	N ₂	N ₂	N ₂	N ₂
Current & time of electrolysis	0.5A, 2h	0.5A, 2h	0.5A, 2h	0.5A, 2h	0.5A, 2h
cathode (inside), vertical cylinder, area (cm ²)	10 cm ²	3 cm²	6 cm²	9 cm²	3 cm²
coiled steel wire or shim (foil)	wire	shim	shim	shim	shim
Length □ wire diameter or shim height (cm)	26.5x0.12	1.67x1.80	3.34x1.80	5x1.80	1.67x1.80
open or with solid bottom	open	open	bottom	bottom	bottom
anode: Ni vertical wire coil or Ni crucible	10cm ² coil	40cm ² coil	40cm ² coil	40cm ² coil	crucible

Ni wire prior to coiling: length x diam (cm) coil or crucible diameter:	16x0.20	64x0.20	64x0.20	64x0.20	
	4.0 cm	4.0 cm	4.0 cm	4.0 cm	3.2 cm
Coulomb. effic. (100% \times Fe ⁰ mass exp/theory)	91.2	100.0	97.5	47.6	98.2



Figure 20. Vertical steel shim electrodes placed inside the anode for STEP Iron electrolysis as described in Table 21.

The electrolysis configuration is simplified when the electrolysis is conducted in a nickel crucible which comprises both the anode and the cell body in one piece, and can further decrease the electrolysis potential. This configurations of the STEP Iron cell is presented in Figure 22; included is a photograph of the cathode after the electrolysis, with the product attached and including some solidified electrolyte). The iron electrolysis product is easy to remove and readily detaches from the cathode. As shown in Figure 21, the electrolysis potential is 1.35 V.

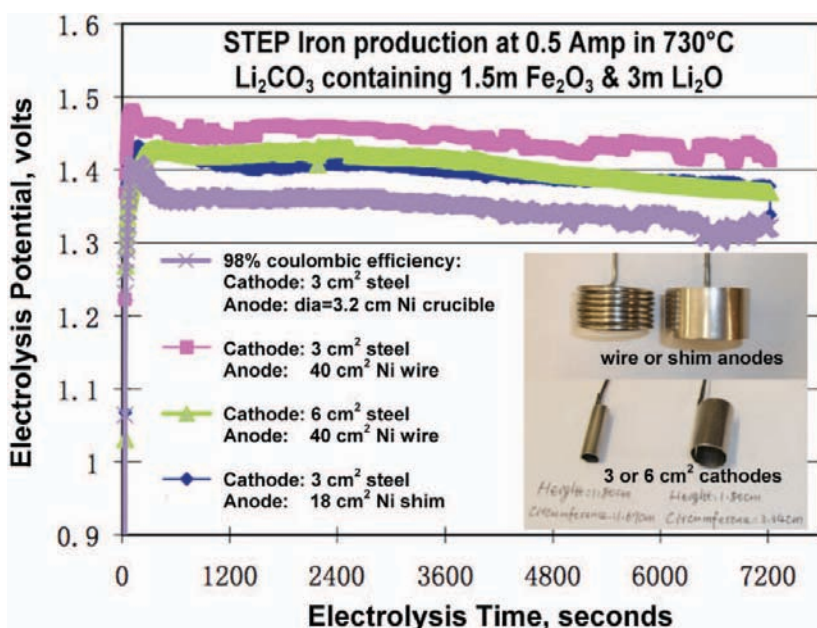


Figure 21. The variation of the electrolysis potential for the electrolytic production of iron. Inset: photographs of anodes (top) or cathodes (bottom) used in these electrolyses. During the electrolysis the cathode, immersed in the molten electrolyte, is situated within the anode.



Figure 22. A nickel crucible serving as both cell wall and anode electrode. A vertical steel cylinder cathode is placed inside the crucible for STEP Iron electrolysis as described in the final column of Table 21. Inset photo: Cathode with product (and including some solidified electrolyte) after the electrolysis.

This electronic supplementary information provides a detailed characterization of the necessary electrolyte composition, temperature and electrochemical component proximity, size and shape for STEP Iron to provide high coulombic efficiency, at low electrolysis potential, while maintaining kinetically facile electron transfer. The coulombic efficiency approaches 100% yield of the 3 e⁻ reduction of Fe₂O₃. The electrolysis potential is less than 1.4 V at a high (current density) rate of iron production. The iron electrolysis product contains iron and electrolyte, and is easy to remove, readily detaching from the cathode. A larger surface area cathode will lower this potential, but may lead to closer proximity to the anode which can decrease the iron coulombic efficiency. Opportunities to significantly decrease the electrolysis potential, while maintaining high cathode current densities, will likely be attained by moving from the largely planar oxygen electrode (anode) to

chemically, or mechanically roughened, high microscopic surface area electrodes, and/or using geometric shapes which will expose more of anode surface than the planar electrode.

Alternative carbonate electrolytes. A more cost effective solution to the corrosivity of the sodium-potassium STEP carbonate melt (than the use of iridium which is stable as an air electrode during 5 hours of electrolysis in 750°C $\text{Na}_{0.23}\text{K}_{0.77}\text{CO}_3$, compared to nickel air electrodes which corrode) is found by the addition of calcium carbonate or barium salts to the sodium-potassium, lithium-free, carbonate melt (the addition of calcium carbonate is shown here for the electrolytic formation of a carbon product from carbon dioxide splitting, rather than an iron product from iron oxide splitting).¹² The addition of calcium carbonate can decrease the melting point of a carbonate mix. The sodium/lithium carbonate mix, $\text{Li}_{1.07}\text{Na}_{0.93}\text{CO}_3$, has a melting point of 499°C, but decreases to below 450°C if 2 to 10 mol% equimolar CaCO_3 and BaCO_3 is added.

In addition to the sodium-potassium carbonate electrolytes, electrolyses are also conducted here in calcium-sodium-potassium electrolytes ranging up to a calcium fraction of $\text{Ca}_{0.27}\text{Na}_{0.70}\text{K}_{0.75}$. Electrodes used are presented in Figure 1. A nickel oxygen anode appears to be fully stable during extended (five hour) 0.5 A electrolyses at 750°C in this melt, using the 30 cm² nickel foil anode and a 7.0 cm² steel wire cathode, and the electrolysis proceeds at between 1.9 to 2.2V. Unlike the electrolyses conducted in the calcium free (sodium-potassium) carbonate melt, carbon forms and remains on the cathode during electrolysis, and the steel cathode remains the same diameter, as measured subsequent to the electrolysis. As shown subsequent to the electrolyses, in the cathode photographs at the bottom of Figure 1, electrolyses conducted in either $\text{Ca}_{0.16}\text{Na}_{1.03}\text{K}_{0.65}\text{CO}_3$ or $\text{Ca}_{0.27}\text{Na}_{0.70}\text{K}_{0.75}\text{CO}_3$ electrolytes exhibit a thick carbon product on the cathode, while this is not the case following electrolysis without calcium carbonate in $\text{Na}_{1.23}\text{K}_{0.77}\text{CO}_3$. The electrolysis potential and subsequent cathode product, during a repeat of the $\text{Ca}_{0.27}\text{Na}_{0.70}\text{K}_{0.75}\text{CO}_3$ electrolysis, but at a constant electrolysis current of 1A, rather than 0.5A, and utilizing a 21cm² (55 cm coiled steel wire) cathode is presented in Figure 2.

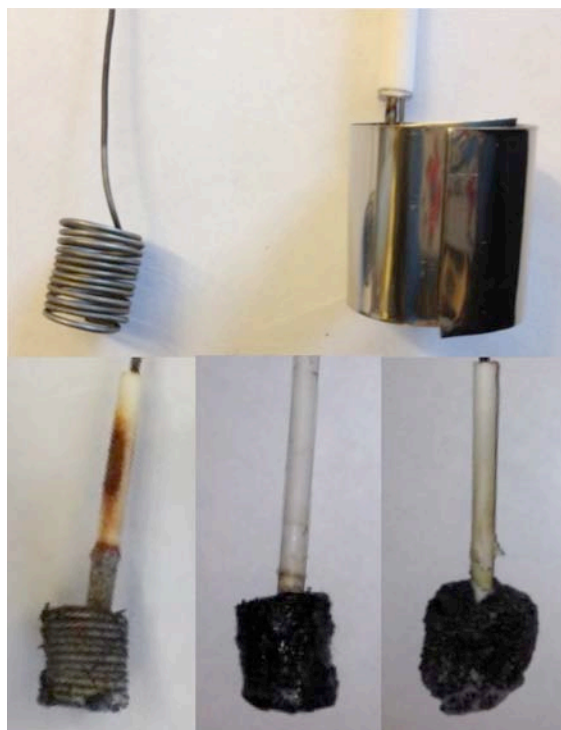


Figure 1. Top: Cathode (top left) and anode (top right) prior to 0.5 A, 5 hour lithium-free electrolyses at 750°C with increasing calcium carbonate concentration. The cathode is placed inside the anode, which are both immersed in the molten electrolyte. Bottom: Cathodes after electrolysis in lithium-free molten carbonates. Electrolytes used were respectively: $\text{Na}_{1.23}\text{K}_{0.77}\text{CO}_3$ (lower left cathode), $\text{Ca}_{0.16}\text{Na}_{1.03}\text{K}_{0.65}$ (lower middle cathode), and $\text{Ca}_{0.27}\text{Na}_{0.70}\text{K}_{0.75}$ (lower right cathode).

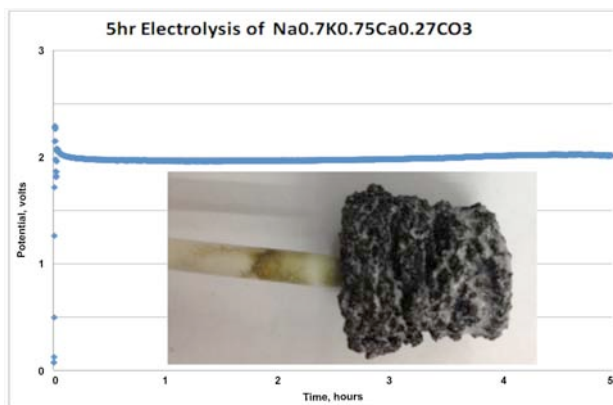


Figure 2. Time variation of the electrolysis potential during a five hour electrolysis at 1A in $\text{Ca}_{0.27}\text{Na}_{0.70}\text{K}_{0.75}\text{CO}_3$ at 750°C. Inset: cathode subsequent to the electrolysis.

References

- ESI-1 A. J. deBethune, T. S. Licht, *J. Electrochem. Soc.*, 1959, **106**, 616.
- ESI-2 J. O'M. Bockris, *Energy Options* (1980, Halsted Press, NY).
- ESI-3 S. Licht, *J. Phys. Chem. B*, 2003, **107**, 4253.
- ESI-4 S. Licht, L. Halperin, M. Kalina, M. Zidman, N. Halperin, *Chem. Comm.*, 2003, **2003**, 3006.

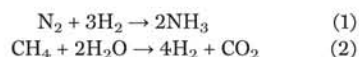
REPORTS

AMMONIA SYNTHESIS

Ammonia synthesis by N₂ and steam electrolysis in molten hydroxide suspensions of nanoscale Fe₂O₃Stuart Licht,^{1*} Baochen Cui,¹ Baohui Wang,¹ Fang-Fang Li,¹ Jason Lau,¹ Shuzhi Liu¹

The Haber-Bosch process to produce ammonia for fertilizer currently relies on carbon-intensive steam reforming of methane as a hydrogen source. We present an electrochemical pathway in which ammonia is produced by electrolysis of air and steam in a molten hydroxide suspension of nano-Fe₂O₃. At 200°C in an electrolyte with a molar ratio of 0.5 NaOH/0.5 KOH, ammonia is produced at 1.2 volts (V) under 2 milliamperes per centimeter squared (mA cm⁻²) of applied current at coulombic efficiency of 35% (35% of the applied current results in the six-electron conversion of N₂ and water to ammonia, and excess H₂ is cogenerated with the ammonia). At 250°C and 25 bar of steam pressure, the electrolysis voltage necessary for 2 mA cm⁻² current density decreased to 1.0 V.

The Haber-Bosch process annually hydrogenates over 120 million metric tons of N₂ from the atmosphere (1, 2) to produce ammonia for fertilizer (Eq. 1) (3). Today, hydrogen for ammonia synthesis is produced primarily through steam reformation, which consumes 3 to 5% of the world's natural gas production and releases large quantities of CO₂ to the atmosphere (1):



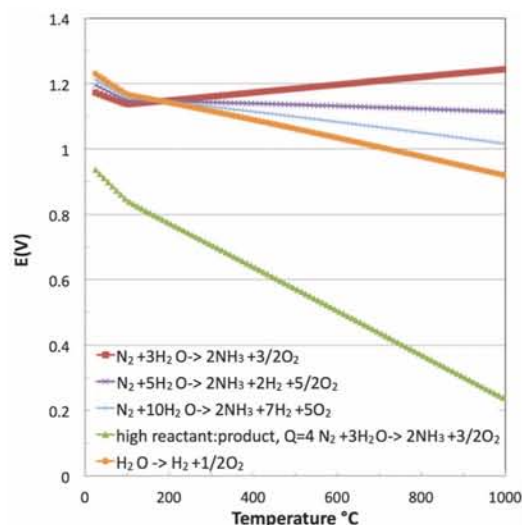
The ammonia hydrogenation reaction is separate from the steam-reforming reaction (Eq. 2) that generates the hydrogen. Renewable energy-driven water splitting could provide an alternative H₂ source, but economic, non-CO₂-emitting sources of H₂ have yet to be proven on the industrial scale. Although ammonia hydrogenation is exothermic, it is kinetically disfavored at ambient temperature and pressure. In the Haber-Bosch process, this kinetic limitation is overcome via an iron-based catalyst, repeated cycling, high pressure, and elevated temperature. The last-named conditions are energy-intensive and consume 2% of the world's energy production (1).

Several electrochemical processes have been pursued to provide alternative syntheses of NH₃. The electrolytic formation of nitrides from nitrogen gas in molten alkali chlorides was studied before 1980 (4, 5), including subsequent reactions with hydrogen to yield ammonia, but such studies have not led yet to commercial production of ammonia because of challenges including the competing back-reaction of nitride to

nitrogen (6–10). In 1985, room-temperature electrolytic synthesis of ammonia was introduced, albeit at low rates, via protolysis of W(N₂)₂(PMe₂Ph)₄ (11). Ammonia was synthesized from H₂ and N₂ in aqueous sulfate solutions using metal-phthalocyanine (C₃₂H₁₈N₈) complexes loaded into carbon black as a cathode and Pt loaded into carbon black as an anode, again at a low rate; note that tin, rather than iron, phthalocyanines exhibited the highest efficiency and stability (12). Density functional calculations have been used to evaluate hydrogen and nitrogen adsorption and/or reduction on a variety of transition metals as possible electrocatalysts in ammonia formation (13). The solid-state electrochemical synthesis of ammonia in two-compartment cells with either proton or oxide ion conductors has been reviewed, with the highest rate reported at 80°C and 2 V using a Nafion membrane (14).

Fig. 1. Thermodynamic electrolysis potentials for water splitting and for water-based ammonia syntheses.

Calculations of potentials are based on the temperature variation of the individual species' thermochemical data. The upper curves are calculated at unit activity, whereas the lower curve is calculated at a high ratio of reactants to products given by $Q = 4 = \log(10,000)$, that is $a_{\text{NH}_3}^2 a_{\text{O}_2}^{3/2} / a_{\text{N}_2} a_{\text{H}_2\text{O}}^3 = 10,000$. Electrolysis provides control of the relative amounts of reactant and generated product in a system. A substantial activity differential ($Q > 1$) can also lower $E(V)$ to drive STEP improvement at elevated temperature.



There are few reports in the literature about using water or steam as a reactant in lieu of hydrogen for the electro-synthesis of ammonia, as one means to avoid the CO₂ emissions of Eq. 2. The rate of ammonia formation is lower by several orders of magnitude, and the coulombic efficiency drops to less than 1%, when water, rather than H₂, is used (14). One study used a strontia-ceria-ytterbia oxide proton-conducting solid electrolyte at 450° to 700°C and a Ru-based catalyst but reported that the conversions with respect to nitrogen or steam were low, primarily because of the poor conductivity of the working electrode (15). Using a Nafion separator in aqueous 2 M KOH with a Ru on C cathode enabled ammonia synthesis from water and nitrogen at a rate and maximum coulombic efficiency of 2.8×10^{-12} mol NH₃ s⁻¹ cm⁻² and 0.9% at 20°C and, at 90°C, a maximum rate of 2.1×10^{-11} mol s⁻¹ cm⁻² at 0.2% efficiency (16). Using Pt/C on a gas diffusion layer at both electrodes and room temperature Nafion as the electrolyte yielded NH₃ at a higher rate of 1.1×10^{-9} mol s⁻¹ cm⁻², which consumed water at the anode and air at the cathode at 0.6% coulombic efficiency (17). Recently, ammonia was formed at 0.8% coulombic efficiency and a similar rate of 0.9×10^{-10} mol s⁻¹ cm⁻² by using Pt/C electrodes and a Nafion membrane (18). The related literature for alkaline electrochemical water splitting (19–21) is substantially larger than for water-air ammonia electro-synthesis. We became intrigued by a molten hydroxide (a NaOH-KOH eutectic electrolyte) ammonia fuel cell (22) in which NH_{3-gas} (as fuel) and air reacted to produce electricity and unspecified products. A subsequent paper used the NaOH-KOH eutectic cell to split water (23) into hydrogen and oxygen in a manner similar to our earlier molten NaOH water splitting protocol (24):

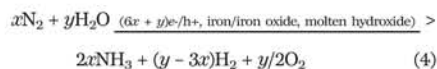


By effectively reversing the NH₃ fuel cell, we present an electrochemical pathway to produce ammonia from air and steam at 200°C with simple materials (molten hydroxide, Ni electrodes,

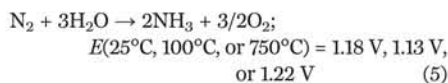
¹Department of Chemistry, George Washington University, Washington, DC 20052, USA.

*Corresponding author. E-mail: slicht@gwu.edu.

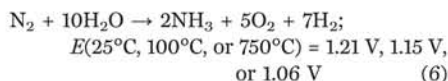
and nano-Fe₂O₃), in one pot without a separator. We reasoned that combining Eq. 3 with Eq. 1 in a highly conductive molten hydroxide for the hydrogen generation, in the presence of an appropriate ammonia-generating catalyst such as iron, should provide a one-pot medium for the electrolytic synthesis of ammonia from air and water:



The thermodynamic potentials for water splitting and the reaction of nitrogen with water are plotted in Fig. 1; they exhibit similar redox potentials at room temperature. We also calculated alternative ammonia-producing reactions, such as the reaction of N₂ with several water molecules, shown in Fig. 1 that could occur in a molten hydroxide medium. In each case, the electrolysis potential is calculated from the known temperature variation of the entropy and enthalpies of the reactants and products by using the convention to describe the positive potential necessary to drive a nonspontaneous potential, $E_T = \Delta G(T)/nF$ (25–28), where the Gibbs free energy is calculated at a temperature (T) and n is the electrons transferred and F is Faraday's constant. On the basis of these calculations, when three H₂O molecules, rather than H₂, act as the hydrogen source for the NH₃ (Eq. 5), the potential decreases up to the water boiling point, but then increases with temperature.



With more than three H₂O equivalents per N₂, as in Eq. 6, hydrogen is cogenerated as a product along with ammonia, and as seen in Fig. 1, the electrolysis potential decreases with increasing water.



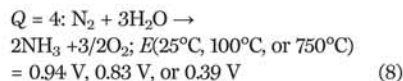
The free energy and, hence, potential variation with activity, a , of the reaction is

$$\Delta G(T, a) = \Delta G^\circ(T) + RT \ln \left[\prod_{i=1}^x a(R_i)^{\nu_i} / \prod_{i=1}^y a(C_i)^{\nu_i} \right] \\ = \Delta G^\circ(T) + 2.303RTQ; \\ \text{ where}$$

$$Q = \log \left[\prod_{i=1}^x a(R_i)^{\nu_i} / \prod_{i=1}^y a(C_i)^{\nu_i} \right] \quad (7)$$

R is the gas constant, T is the Kelvin temperature, and R_i and C_i represent the products and reactants. Q in Eq. 7 combines the log of the reaction quotient and n into a single term to assess the magnitude of this Nernst effect and reflects the relative activity of the reactants compared with the products. Reaction 5 yields $Q = \log(a_{\text{NH}_3}^2 a_{\text{O}_2}^{3/2} / a_{\text{N}_2} a_{\text{H}_2\text{O}}^3) / 6$. As shown in Fig. 1, with appropriate choice of medium, this Eq. 7 Nernst effect can

generate a dramatic energy decrease in the required electrolysis potential, for example, in molten electrolytes when the water reactant and nitrogen concentrations are high and the product concentration is relatively low. The effect is enhanced proportionally to the relative increases in the Kelvin temperature. Compared with $Q = 1$ in Eq. 5:



As measured at 200°C, the molten hydroxide electrolyzer efficiently splits water, bubbled in as steam. As expected, H₂ was produced at a 2:1 ratio to O₂ when the electrolyzer did not contain nitrogen or an effective ammonia generation surface. A range of LiOH, NaOH, KOH, and CsOH eutectic mix (29) electrolytes (such as a molar ratio of 0.5 NaOH/0.5 KOH) were effective for water electrolysis below 300°C. The pure alkali hydroxides each melt only at temperatures above 300°C. Based on common materials, the NaOH-KOH eutectic is of particular interest and melts at 170°C. At 200°C, this electrolyte approached 100% of the electrolysis efficiency for water splitting. The variation of the water-splitting electrolysis voltage as a function of current density and temperature at 1 atmosphere was measured between planar Ni electrodes and is presented in Fig. 2. Alternative, textured, and/or alloyed electrodes and modifications of the cell configuration have been widely studied (19–21) and can decrease the electrolysis voltage at higher water-splitting current densities.

Experimentally, we observed high rates of ammonia generation when the 200°C molten hydroxide (NaOH-KOH) electrolyte was mixed with high-surface area Fe₂O₃ to provide iron as a reactive surface and when nitrogen and water vapor were in the cell. The medium was electrolyzed between a planar nickel anode and a mesh nickel-monel cathode. Initially, the H₂-evolving mesh cathode had been used to enclose the iron oxide, but the mesh openings were too large to contain the nano-Fe₂O₃. Therefore, nano-Fe₂O₃ was simply added to the electrolyte. Both water-saturated nitrogen and CO₂-scrubbed air (bubbled through a 1 M NaOH solution to remove CO₂) yielded similar efficiencies of ammonia generation. In lieu of air, 99.999% nitrogen was saturated with water at room temperature by bubbling the nitrogen through doubly deionized water en route to the electrolyzer. Unlike the water-splitting electrolysis, the efficiency of the ammonia generation by electrolysis was lower at higher current densities.

Ammonia generation by electrolysis here refers to the global reaction of nitrogen, water, and electrons to form ammonia (and oxygen), and the efficiency is calculated based on the moles of electrons consumed compared with the equivalents of ammonia (3e⁻/NH₃) generated. This efficiency was >30% at 20 mA through 10 cm² electrodes compared with ~7% at 250 mA. This suggests that the conversion efficiency is not limited by the available hydrogen, but rather by the available surface area of the nano-Fe₂O₃ to promote the nitrogen and hydrogen conversion to ammonia.

The measured efficiency of ammonia evolution in time in 200°C NaOH-KOH molten electrolyte under a variety of conditions is shown in Fig. 3, including a constant current of either 0 or 20 mA between the 10 cm² Ni electrodes. Evolved ammonia was collected and measured in a room-temperature water trap. The constant current of electrolysis was measured. The three electron equivalents of ammonia, measured as described in the supplementary material, were divided by this integrated electrolysis charge to determine the electrolysis efficiency to synthesize ammonia. The electrolysis efficiency to produce ammonia was high, in excess of 30% when we used either wet air or wet nitrogen reactants and with nano-Fe₂O₃ to provide iron as a reactive surface (30). This observed >30% efficiency for the conversion of electrons, air, and water to ammonia compares with the highest values of <1% previously noted for the generation of ammonia from air or nitrogen and water (16–18). The cogeneration of H₂, as measured by a Micro IV hydrogen analyzer (GfG Instrumentation) is consistent with the remaining (~65%) electrolysis current (30). At 20 mA applied current, the cogeneration of ammonia and hydrogen is consistent with the net reaction: N₂ + 8H₂O → 2NH₃ + 4O₂ + 6H₂, but, as will be shown, the ratio of H₂ to NH₃ grows with increasing applied current. As seen in Fig. 3, ammonia is not generated if current is not applied. Iron oxide-iron mixes are catalysts for the traditional chemical synthesis of ammonia. The high surface area of the nano-Fe₂O₃ in the new electrochemical synthesis appears critical to the

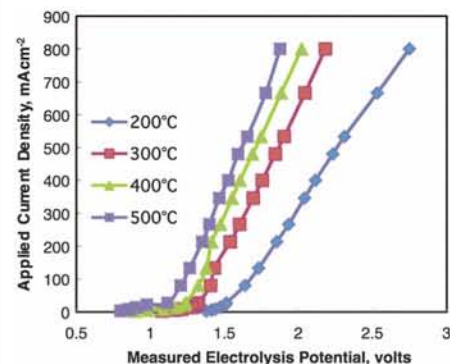


Fig. 2. Measured electrolysis potential. The measured electrolysis potential at 200°C of a molar molten mix of 0.5 NaOH/0.5 KOH at 1 atmosphere between two 2.5- by 1.5-cm planar nickel electrodes. Steam is bubbled into the cell to saturate each electrolyte with water. For example, the 200°C molten NaOH-KOH electrolyte contains ~8% weight water. At 200°C, the coulombic water-splitting efficiency approaches 100% as measured for currents of 25 to 1000 mA cm⁻². Water-splitting coulombic efficiency in the open air drops with increasing temperature as the molten electrolyte dehydrates with increasing temperature. At 300°C, the coulombic efficiency has dropped to ~90%, and by 500°C, the coulombic efficiency has decreased to 25%. Note that measured potentials are ~0.1 V lower when lithiated Ni anodes and monel mesh cathodes are used in lieu of planar nickel (30).

process. As seen in Fig. 3, the cell with no Fe_2O_3 , or conventional (99.4%, J.T. Baker), rather than nanoscopic, Fe_2O_3 , did not generate discernible ammonia. The 20- to 40-nm Fe_2O_3 remains colloidal throughout the electrolysis, whereas the conventional Fe_2O_3 descends and collects at the bottom of the electrolysis cell. After we milled conventional Fe_2O_3 at 300 rpm for 2 hours in a Retsch PM100 ball mill, discernible ammonia still was not generated during electrolysis, and the Fe_2O_3 still collected at the bottom of the cell. However, ball milling at 600 rpm for 2 hours, which decreased the particle size to ~ 200 nm, sustained a colloidal suspension throughout the electrolysis and generated a small, but discernible, quantity of ammonia at ~ 0.03 times the rate of the 20- to 40-nm Fe_2O_3 electrolysis cell. As delineated in the supplementary materials, when the 20- to 40-nm Fe_2O_3 was placed above (in the headspace), rather than in, the electrolyte, ammonia was not generated. Ammonia also was not generated when 20- to 40-nm Fe_2O_3 was first heated under argon to desorb any nitrogen before its addition to the molten electrolyte, and when argon (saturated with water vapor), rather than nitrogen, was bubbled into the cell during the electrolysis. However, as seen in Fig. 3, when wet (water-saturated) argon, rather than nitrogen, was bubbled into the cell, and nano- Fe_2O_3 without this desorption pretreatment was added to the electrolyte, a low level of ammonia was initially generated until nitrogen, evidently preadsorbed onto the nano- Fe_2O_3 , was depleted.

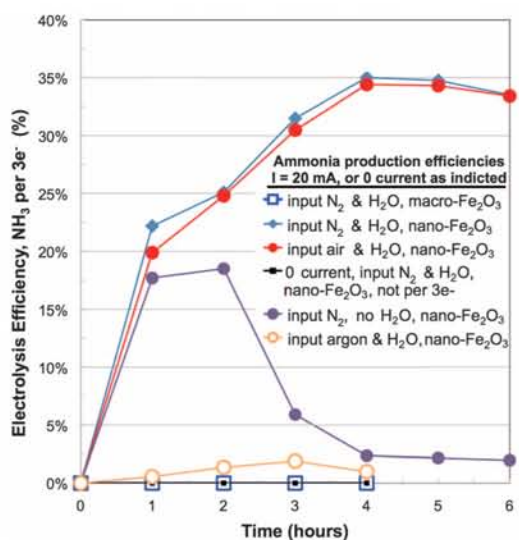
Ammonia was also initially generated under conditions without water vapor in the nitrogen. However, as seen in Fig. 3, this ammonia production tapered off rapidly in time. This appears to be consistent with consumption of the molten hydroxide as an alternate source of water:



In accord with Eq. 9, ammonia production continued until the molten hydroxide became dehydrated and oxide enriched.

Fig. 3. Efficiency of current conversion of ammonia product. Experimental quantification of ammonia from air or nitrogen, either saturated with water or dry, by one-pot synthesis.

The input gas was added to molten hydroxide at 200°C and electrolyzed in the presence of nano- or micron-sized Fe_2O_3 . The indicated constant current was applied between 10 cm^2 Ni electrodes. The product gas was bubbled through a water trap quantitatively analyzed for ammonia and compared with the applied, integrated electrolysis charge to determine the electrolysis efficiency.



The full cell voltage to drive molten hydroxide electrolysis of wet nitrogen or air to ammonia at 200°C in the presence of nano- Fe_2O_3 was $1.23 (\pm 0.02)$ V when the applied current was 20 mA between the 10 cm^2 Ni electrodes (2 mA cm^{-2}) in the molten NaOH-KOH electrolyte; it increased to $1.44 (\pm 0.02)$ V when the current increased to 250 mA (25 mA cm^{-2}), and then to 2.4 V for 2000 mA (200 mA cm^{-2}). At 2 mA cm^{-2} , under these conditions, ammonia evolved at a rate of $2.4 \times 10^{-9}\text{ mol s}^{-1}\text{ cm}^{-2}$, and hydrogen was cosynthesized at $6.6 \times 10^{-9}\text{ mol s}^{-1}\text{ cm}^{-2}$. At 25 mA cm^{-2} the ammonia synthesis rate increased to $6.7 \times 10^{-9}\text{ mol NH}_3\text{ s}^{-1}\text{ cm}^{-2}$, and the rate of hydrogen coproduction increased to $1.0 \times 10^{-7}\text{ mol H}_2\text{ s}^{-1}\text{ cm}^{-2}$. Hence, with increasing current density, the observed produced ratio of H_2 to NH_3 increased, that is the hydrogen coproduction rate increased more rapidly than the ammonia production rate, and the global ($\text{NH}_3 + \text{H}_2$) coulombic efficiency remained high at current densities of both 2 and 25 mA cm^{-2} . At the highest current density of 200 mA cm^{-2} , the ammonia production rate was $1.0 \times 10^{-8}\text{ mol NH}_3\text{ s}^{-1}\text{ cm}^{-2}$. Cesium has been observed to enhance the catalytic activity of iron and iron oxides in ammonia production (31, 32). At 200°C when the NaOH-KOH electrolyte was replaced by a CsOH electrolyte (containing 30 wt % water to maintain the liquid-molten state at 200°C) the 25 mA cm^{-2} rate increased from 6.7×10^{-9} to $7.7 \times 10^{-9}\text{ mol NH}_3\text{ s}^{-1}\text{ cm}^{-2}$. At the measured current densities and temperature, the variation of the electrolyte cation has not been observed to affect the electrolysis potentials. The same electrolysis potentials were observed when the 0.5:0.5 NaOH-KOH molten electrolyte was replaced by a 0.48:0.52 molar ratio NaOH-CsOH, a 0.7:0.3 NaOH-LiOH, or a 0.7:0.3 KOH-LiOH eutectic electrolyte. Presumably, higher current densities and higher temperature potential will be affected by the cation, which will affect electrolyte conductivity and water retention.

The energy consumption of this ambient pressure process varies with rate (which affects the voltage) and the ammonia-only or global current

efficiency (including both ammonia and hydrogen). Hydrogen cogenerated with the ammonia is not lost energy and is available for storage, or use as a fuel, or as a chemical reactant. As a first estimate of the energy consumption, we use the 1.2 V at 2 mA cm^{-2} ($= 2.4 \times 10^{-9}\text{ cm}^{-2}\text{ MJ s}^{-1}$). This produces $2.4 \times 10^{-9}\text{ s}^{-1}\text{ cm}^{-2}\text{ mol NH}_3$ ($= 4.1 \times 10^{-11}\text{ s}^{-1}\text{ cm}^{-2}\text{ kg NH}_3$); that is, 59 MJ is consumed per kg NH_3 produced. The energy content of the recovered H_2 is 120 to 142 MJ/kg (with or without the heat of water vaporization). This energy consumption estimate does not include the associated engineering losses, or the energy of heating to 200°C , as the optimal operating temperature needs to be determined.

In the absence of the nano- Fe_2O_3 , water is simply electrolyzed into hydrogen at the cathode and oxygen at the anode in the 200°C molten hydroxide chamber. In the presence of nano- Fe_2O_3 , two alternative mechanisms of the ammonia synthesis can be considered. In the first, electrochemical reduction of water to hydrogen occurs at the cathode, which then diffuses to react with adsorbed nitrogen on the nano- Fe_2O_3 surface to form ammonia. An alternative mechanism to consider is the electrochemical reduction of nitrogen and water at the nano- Fe_2O_3 to form ammonia. The latter mechanism would necessitate electron transfer from the nickel cathode to the dispersed, electrolyte-suspended nano- Fe_2O_3 . The latter mechanism could be ruled out in the 200°C molten hydroxide electrolyte with the high-surface area Fe_2O_3 if ammonia were to be formed when no electrochemical current was applied, as in the case where H_2 and N_2 (rather than H_2O and N_2) were instead added as chemical reactants. That situation would preclude the electrochemical reduction of nitrogen and water at the suspended Fe_2O_3 and yet facilitate ammonia formation. It was interesting that little or no ammonia was formed in this case when gas phase H_2 and N_2 , with or without O_2 , were introduced to this cell without current. As one experiment, H_2 was used as the inlet reactant (with O_2 , N_2 , and H_2O) after generation by room-temperature electrolysis at 2000 mA in an aqueous solution of 4 M NaOH and 4 M KOH . This generated gas containing 2:1 H_2 to O_2 , and forming 15 ml min^{-1} of H_2 , was mixed with 5 ml min^{-1} of water saturated N_2 as the inlet gas. This procedure converts the one-pot synthetic chamber into a two-pot chamber (in which hydrogen is formed by electrolysis in the preliminary room-temperature pot and bubbled into the second molten electrolyte pot through the nickel tube and nickel mesh). In this case, ammonia was formed at a marginal, but discernible, rate compared with that observed when the 2000 mA of current was applied directly to the 200°C electrolysis chamber (0.2×10^{-9} versus $1.0 \times 10^{-8}\text{ mol NH}_3\text{ s}^{-1}\text{ cm}^{-2}$). As a second experiment, without any electrolysis, 15 ml min^{-1} pure H_2 and 5 ml min^{-1} pure N_2 gases were bubbled through water and used as the inlet gas. Again, ammonia was only formed at a marginal, but discernible, rate (0.2×10^{-9} versus $1.0 \times 10^{-8}\text{ mol NH}_3\text{ s}^{-1}\text{ cm}^{-2}$). We posit that these experiments provide supporting evidence that the second mechanism (electrochemical reduction of the nitrogen and water at the nano- Fe_2O_3) of ammonia

synthesis dominates. However, alternative factors such as a (smaller, more reactive) H_2 bubble size for the in situ generated (one-pot) versus ex situ hydrogen may contribute to the lack of the observed reaction of gas phase hydrogen to ammonia.

The simple dispersion of the nano-iron oxides in the electrolyte, as demonstrated in this study, was not conducive to long-term stability of the cell, as electrostatics tend to coagulate the nanoparticles over time. During the last 2 hours of a 200°C (NaOH-KOH) 6-hour, 2 mA cm^{-2} run, the ammonia production rate fell to 85% of its average value over the first 4 hours. Better mixing and excess nitrogen and water vapor significantly stabilized the rate. When the water-saturated nitrogen increased from 4 to 111 ml min^{-1} (retaining all other conditions at the 20 mA applied current), the ammonia production fell only 3% (to 97% of the average rate over the first 6 hours). We are exploring providing a rigid structure to immobilize the dispersed nano-iron oxides in a solid framework.

In this study, we also introduced a solar thermal water self-pressurizing, low electrolysis energy path system. Solar thermal energy is readily absorbed at conversion efficiency in excess of 65% (33–35), and here provides an efficient energy source and mechanism to maintain a high reactant pressure. Specifically, the NaOH-KOH electrolyte under N_2 gas is heated with varying amounts of water in a confined volume. As expected, heating in a constrained volume evaporates water and yields up to a demonstrated increase in water pressure from 0.03 bar at room temperature to 60 bar at 275°C, and a concurrent decrease in the ammonia electro-synthesis potential in hydroxide electrolytes as ammonia is formed, and as described in the supplementary materials (30). The generated high water pressure is in accord with improved high Q/low ammonia energy synthesis conditions theoretically predicted by Eqs. 7 and 8, as seen by the lower voltage curve of Fig. 1. At 250°C and 25 bar of steam pressure, the observed electrolysis potentials were 0.78V, 1.01V, and 1.31V, respectively, at 0.1, 2, and 25 mA cm^{-2} . The last-named potentials are 0.2 V more favorable than observed at ambient pressure and 200°C. The measured 2 mA cm^{-2} rate of ammonia synthesis of 2.4×10^{-9} mol $cm^{-2} s^{-1}$ at high pressure is similar to that observed at ambient pressure, but the coproduction of H_2 is not observed at this lower potential (30).

There is ample room for advances of this pathway. Fe_2O_3 was utilized as the reactive surface, whereas today's Haber-Bosch catalysts use Fe_2O_3 or ruthenium-based catalysts with a wide variety of carefully optimized additives (31, 32, 36), which may also improve this electrochemical process.

REFERENCES AND NOTES

1. V. Smil, *Enriching the Earth: Fritz Haber, Carl Bosch, and the Transformation of World Food Production* (MIT Press, Cambridge, MA, 2004).
2. J. Rockström et al., *Nature* **461**, 472–475 (2009).
3. R. Strait, M. Nagvekar, Carbon dioxide capture and storage in the nitrogen and syngas industries. *Nitrogen+Syngas* **303** (Jan.-Feb.), 1–3 (2010); www.kbr.com/Newsroom/

Publications/Articles/Carbon-Dioxide-Capture-and-Storage-in-the-Nitrogen-Syngas-Industries.pdf.

4. A. Bonomi, M. Hadat, C. Gentaz, *J. Electrochem. Soc.* **124**, 982–986 (1977).
5. A. Bonomi, M. Hadat, F. Breda, *J. Electrochem. Soc.* **126**, 248–251 (1979).
6. T. Murakami, T. Nishikiori, T. Nohira, Y. Ito, *J. Am. Chem. Soc.* **125**, 334–335 (2003).
7. Y. Ito, T. Goto, *J. Nucl. Energy* **344**, 128–135 (2005).
8. T. Murakami, T. Nohira, Y. H. Ogata, Y. Ito, *Electrochem. Solid-State Lett.* **8**, D12–D14 (2005).
9. T. Murakami et al., *Electrochem. Solid-State Lett.* **10**, E4–E6 (2007).
10. N. Serizawa et al., *J. Electrochem. Soc.* **159**, E87–E91 (2012).
11. C. J. Pickett, J. Talarmin, *Nature* **317**, 652–653 (1985).
12. N. Furiya, H. Yoshida, *J. Electroanal. Chem.* **291**, 269–272 (1990).
13. E. Skúlason et al., *Phys. Chem. Chem. Phys.* **14**, 1235–1245 (2012).
14. I. Amar, R. Lan, C. Petit, S. Tao, *J. Solid State Electrochem.* **15**, 1845–1860 (2011).
15. A. Skodra, M. Stoukides, *Solid State Ion.* **180**, 1332–1336 (2009).
16. V. Kordali, G. Kyriacou, C. Lambrou, *Chem. Commun. (Camb.)* **2000**, 1673–1674 (2000).
17. R. Lan, J. T. S. Irvine, S. Tao, *Sci. Rep.* **3**, 1145 (2013).
18. R. Lan, S. Tao, *RSC Adv.* **3**, 18016–18021 (2013).
19. J. R. McKone, S. C. Marinescu, B. S. Brunschwig, J. R. Winkler, H. B. Gray, *Chem. Sci.* **5**, 865–878 (2014).
20. D. Santos, C. A. C. Sequeira, J. L. Figueiredo, *Quím. Nova* **8**, 1176–1193 (2013).
21. K. Zeng, D. Zhang, *Progr. Energy Combust. Sci.* **36**, 307–326 (2010).
22. J. Ganley, *J. Power Sources* **178**, 44–47 (2008).
23. J. Ganley, *Int. J. Hydrogen Energy* **34**, 3604–3611 (2009).
24. S. Licht, L. Halperin, M. Kalina, M. Zidman, N. Halperin, *Chem. Commun. (Camb.)* **2003**, 3006–3007 (2003).
25. M. W. Chase, *J. Phys. Chem. Ref. Data* **9**, 1 (1998).
26. Thermochemical data from (25) are available online at U.S. National Institute of Standards and Technology ChemWeb: <http://webbook.nist.gov/chemistry/form-ser.html>.
27. Glenn Research Center, National Aeronautics and Space Administration (NASA), ThermoBuild access to NASA Glenn thermodynamic CEA database (2006); data available at www.grc.nasa.gov/WWW/CEAWeb/ceaThermoBuild.htm.
28. S. Licht, *J. Phys. Chem. C* **113**, 16283–16292 (2009).
29. A. Pelton, K. Hack (and codevelopers), *283 binary salt phase diagram*, [Facility for the Analysis of Chemical Thermodynamics (FACT). Centre for Research in Computational Thermochemistry (CRCT), University of Montreal, rev. ed., 2012]; www.crct.polymtl.ca/FACT/documentation/FTsalt/FTsalt_Figs.htm.
30. Materials and methods are detailed in the supplementary materials on Science Online.
31. A. Hellman et al., *J. Phys. Chem. B* **110**, 17719–17735 (2006).
32. M. Appl, Ammonia 2 production processes, *Ullman's Encyclopedia of Industrial Chemistry*, doi: 10.1002/14356007 (Wiley-VCH, Weinheim, Germany, ed. 7, 2012), pp. 139–210.
33. S. Licht, *Adv. Mater.* **47**, 5592–5612 (2011).
34. R. Pritz-Paal, in *Solar Energy Conversion and Photoenergy Systems*, J. B. Galvez, S. M. Rodriguez, Eds. (EOLSS Publishers, Oxford, 2007).
35. T. Hahn, H. Schmidt-Traub, B. Leßmann, *Sol. Energy* **65**, 33–41 (1999).
36. W. Ziqing, Z. Kiuming, L. Jianxin, W. Rong, W. Kemei, *J. Catal.* **33**, 377–378 (2013).

ACKNOWLEDGMENTS

Full materials and methods and a section on solar thermal-constrained volume pressurization are presented in the supplementary materials. The authors are grateful for partial support of this research by the Office of Naval Research (award N00014-13-1-0791). A related provisional U.S. patent has been filed.)

SUPPLEMENTARY MATERIALS

www.sciencemag.org/content/345/6197/637/suppl/DC1
Materials and Methods
Supplementary Text
Figs. S1 to S5
Table S1
References

1 April 2014; accepted 23 June 2014
10.1126/science.1254234



Supplementary Materials for
**Ammonia synthesis by N₂ and steam electrolysis in molten hydroxide
suspensions of nanoscale Fe₂O₃**

S. Licht,* B. Cui, B. Wang, F.-F Li, J. Lau, S. Liu

*Corresponding author. E-mail: slicht@gwu.edu

Published 8 August 2014, *Science* **345**, 637 (2014)
DOI: 10.1126/science.1254234

This PDF file includes

Materials and Methods
Supplementary Text
Figs. S1 to S5
Table S1
References

Supplementary Materials

Ammonia synthesis by N₂ and steam electrolysis in molten hydroxide suspensions of nanoscale Fe₂O₃

Stuart Licht,^{1*} Baochen Cui,¹ Baohui Wang,¹ Fang-Fang Li,¹ Jason Lau,¹ Shuzhi Liu¹

Materials

Anhydrous sodium hydroxide (Sigma-Aldrich S5881), potassium hydroxide (sigma-aldrich P1767, KOH•½H₂O), cesium hydroxide (99.9% CsOH•1-2H₂O Alfa-Aesar 13233) and lithium hydroxide (anhydrous, 98%, Acros Organics 37918) are combined to form various eutectic molten hydroxide electrolytes each with melting points < 300°. The pure anhydrous alkali hydroxides each melt only at temperatures > 300°C; LiOH (T_{mp} = 462°C), NaOH (T_{mp} = 318°C), KOH (T_{mp} = 406°C), CsOH (T_{mp} = 339°C). Whereas, molar ratios of 0.3:0.7 LiOH/NaOH, 0.3:0.7 LiOH/KOH, 0.5:0.5 NaOH/KOH, 0.44:0.56 KOH/CsOH, respectively melt at 215°C, 225°C, 170°C and 195°C (22), and are even lower when hydrated hydroxide salts are used. Conventional microscopic (99.4%, JT Baker) or high surface area nanoscopic (20-40 nm particle, 30-60 m²/g AlfaAesar 45007, NanoArc; used lot L20Y042: Alfa Aesar Certificate of analysis, 99.9% iron oxide, 35 nm average particle size, 33 m² g⁻¹ BET) Fe₂O₃ are added to the molten hydroxide electrolyte to promote ammonia formation.

Gas input to the electrolysis chamber consisted of either A: wet (1) 99.999% nitrogen (ultra high purity nitrogen generator 3000 cc/min Dominick Hunter G2-110W), or (2) Ar, bubbled through double deionized water to water saturation at room temperature (2.6% water at 22°C), or (3) air bubbled through a 1 M KOH solution to remove carbon dioxide and saturate with water at room temperature, B: the dry gases. Gas flow was maintained at 4.1 ml min⁻¹ in the 20 mA electrolyses and 111 ml min⁻¹ in the 250 mA electrolyses. For mass balance the wet (water saturated) gases provide sufficient water (8x10⁻⁸ or 2x10⁻⁶ mol H₂O/s, respectively) for the hydrogen generation component of the electrolysis and excess nitrogen. It is a challenge to design higher input gas flow rates into the current cell design, and the 2000 mA experiment is conducted with flow of 222 (and also a slow flow experiment of 2.2) ml min⁻¹. The latter, 2000 mA slow flow 2.2 ml min⁻¹ experiment constrains steam and nitrogen entering the cell and yields only 0.62 of the initial ammonia production rate of the fast flow experiment, and respectively after 4 or 6 hours exhibited an ammonia rate of only 13% or 5% of the initial two hour average rate. As described in the text, excluding either nitrogen or water from the cell decreased (zeroed) the ammonia output from the electrolysis cell. The electrolysis is conducted in a pure alumina crucible (AdValue, 99.6%). In the alumina crucible cell, the anode consists of a pure Ni (McMaster 200) shim cut to 10 cm², the 10 cm² Ni cathode consists of 200 mesh woven wire cloth (Alloy 400, Monel, McMaster 9225T361). This Monel cathode mesh is stable in the molten 200°C hydroxide, whereas 316 stainless steel mesh is observed to (slowly) react forming hydrogen. The electrodes are connected externally by spot welded Ni wire (99.5% Alfa Aesar 41361).

Calculations

Thermodynamic electrolysis potentials for water splitting and ammonia synthesis with water are calculated from the unit activity thermochemical data for the individual species, using the convention to describe the positive potential necessary to drive a non spontaneous potential (19-21), from the reactions: $\sum_{i=1}^x r_i R_i \rightarrow \sum_{i=1}^y c_i C_i$; using

$$E_T = \Delta G(T)/nF$$

$$\text{and } \Delta G^\circ(T) = \sum_{i=1}^y c_i (H^\circ(C_i, T) - TS^\circ(C_i, T)) - \sum_{i=1}^x r_i (H^\circ(R_i, T) - TS^\circ(R_i, T)).$$

Electrolysis provides control of the relative amounts of reactant and generated product in a system. A substantial activity differential can also drive **STEP** improvement at elevated temperature. The free energy and hence potential variation with activity, a , of the reaction is,

$$\begin{aligned} \Delta G(T, a) &= \Delta G^\circ(T) + RT \ln \left(\frac{\prod_{i=1}^x a(R_i)^{r_i}}{\prod_{i=1}^y a(C_i)^{c_i}} \right) \\ &= \Delta G^\circ(T) + 2.303 RT Q; \text{ where } Q = \log \left(\frac{\prod_{i=1}^x a(R_i)^{r_i}}{\prod_{i=1}^y a(C_i)^{c_i}} \right) \end{aligned}$$

Methods

A single chamber electrolysis configurations was used to electrolyze water saturated air or N_2 to NH_3 . In addition a double chamber cell configuration was only used to confirm that ammonia was separately generated at the cathode and oxygen at the anode. The latter configuration is described in the subsequent paragraph. The single chamber configuration is photographed in Fig. S1. A stainless steel (316 alloy) cover is cut with a groove on the lower side that matches the circumference of the alumina crucible (100 ml alumina crucible Advent AL-2100). The cover to crucible seal is gas-leak free when the groove is filled with a high temperature adhesive (Resbond 907 heavy grade adhesive) and the cover is compressed to the crucible by four outer bolts through the cover and a bottom plate as seen in the figure. 0.25" Inconel (McMaster 89865K) or alumina tubes (McMaster 8746K) pass through the cover into the electrolyzer, and are gas-leak free when sealed with the Resbond 907. The middle alumina tube becomes the outlet gas exit, which is bubbled through an ammonia trap (described below). The anode connecting wire seen on the left is in an alumina tube. The inconel tube, seen on the right side, functions as both the cathode electrical connection and as the gas inlet. Either N_2 or air, and water vapor enters through this inlet. The anode and cathode tubes are also sealed at the cover with Resbond 907 adhesive. In addition the cathode tube is connected to the inlet gas (either N_2 or air and water vapor). The cell is situated within a 1700 W Band Heater (McMaster 8160T21), and insulated by (1) alumina silica ceramic fiber ultra high insulation with an aluminum facing on one side (McMaster 9379K93) and (2) rigid thermal shock resistant ceramic insulation without binder (McMaster 9359K75). Temperature is monitored by thermocouple and controlled by DIN Compact Temperature Controller (Omega CN2100-R20). The full cell voltage to drive molten hydroxide electrolysis of wet N_2 or air to ammonia at 200°C in the presence of nanoscopic Fe_2O_3 is 1.2V when the applied current is 20 mA between the 10 cm² Ni electrodes, and increases to 1.4 V when the current is increased to 250 mA. In each case, when current is applied

the electrolysis potential rises from 0V to 60% of the final voltage within the initial 30 seconds of electrolysis, and to 80% of the final potential within the first 5 minutes of the electrolysis. We observe that Ni, Pt (18) and lithiated Ni (17) are effective anodes. The lithiated Ni is prepared by anodization at 1 mA cm^{-2} for 24 hours in 100°C 3M LiOH, and drives the electrolysis at a $\sim 0.07\text{V}$ lower potential. However, in this study, commercial, pure (Ni 200) shim is employed as the anode to demonstrate ease of process. At these current densities and temperature, variation of the cation has not been observed to affect these electrolysis potentials. The same electrolysis potentials are observed when the equimolar NaOH/KOH molten electrolyte, is replaced by an 0.48:0.52 molar ratio NaOH/CsOH, an 0.7:3 NaOH/LiOH, or an 0.7:3 KOH/LiOH eutectic electrolyte. Presumably, higher current densities and higher temperature potential will be affected by the cation, which will affect electrolyte conductivity and water retention.

The product gas from the electrolysis chamber is bubbled (sparged) through an ammonia trap containing 500 ml doubly deionized water, changed regularly for ammonia analysis. Ammonia concentration was determined by triple redundant methodologies (1) UV/vis absorption, (2) ion selective electrode analysis (Hach 2348700 Ammonia ISE Analysis package) and (3) ammonia test strips (Hach 2755325, dilution required on more concentrated samples). In each case, redundant measurements yield similar ammonia measurements, with the observed reproducibility of first two methodologies $\pm 2\%$ and the test strips to $\pm 5\%$. Initially, two water traps (in series) were used to probe whether all ammonia was collected by the first water trap. No ammonia was measured in the second water trap, even under high ammonia production conditions, and only a single water trap was used in subsequent experiments. A (single 500 ml) millimolar acid water trap was also effective. High ammonia concentrations required a dilution prior to analysis by the ammonia test strips. The ammonia ISE is calibrated with a series of NH_4Cl solutions, and 2 ml pH of ionic strength adjustor (Orion ISA 951210) added to 100 ml of analyte. The ammonia ISE responds quickly to moderate and high ammonia concentrations, however required several minutes to reach a limiting voltage (concentration) when analyzing dilute ammonia concentrations. Hence, UV/vis was the preferred method of analysis. The UV/vis ammonia determination is measured by absorption at 697 nm on Perkin Elmer Lambda 35 in a conventional 1 cm path length cuvette by the salicylic method, as calibrated with standard aqueous ammonium chloride (NH_4Cl) solutions. The method is delineated in reference 30, and in brief absorption is measured following the additions of 0.36 M salicylic acid ($\text{C}_6\text{H}_4(\text{OH})\text{COOH}$) in 0.32 M aqueous NaOH, aqueous 0.032 sodium nitroprusside ($\text{Na}_2[\text{Fe}(\text{CN})_5\text{NO}] \cdot 2\text{H}_2\text{O}$), and 0.1M sodium hypochlorite (NaClO) in 0.75 M aqueous NaOH. Ammonia measured under a variety of discharge conditions is presented in Table S1.

H_2 was measured directly by a Micro IV hydrogen analyzer (GfG Instrumentation) or, in the case of high hydrogen concentrations, following serial dilution by added nitrogen; at lower N_2 inlet flow rates, H_2 was redundantly determined by the volume of H_2 & O_2 gas collected (after corrections for the partial volumes of N_2 and $\text{H}_2\text{O}_{\text{vapor}}$). H_2 was redundantly measured, along with O_2 , by GC (HP 5890 series II gas chromatograph) with 3 ml/min argon flow using a Carboxen-1010 column, injecting a $250\mu\text{L}$ sample, which yields H_2 and O_2 peaks respectively at 2.15 and 3.7 minutes.

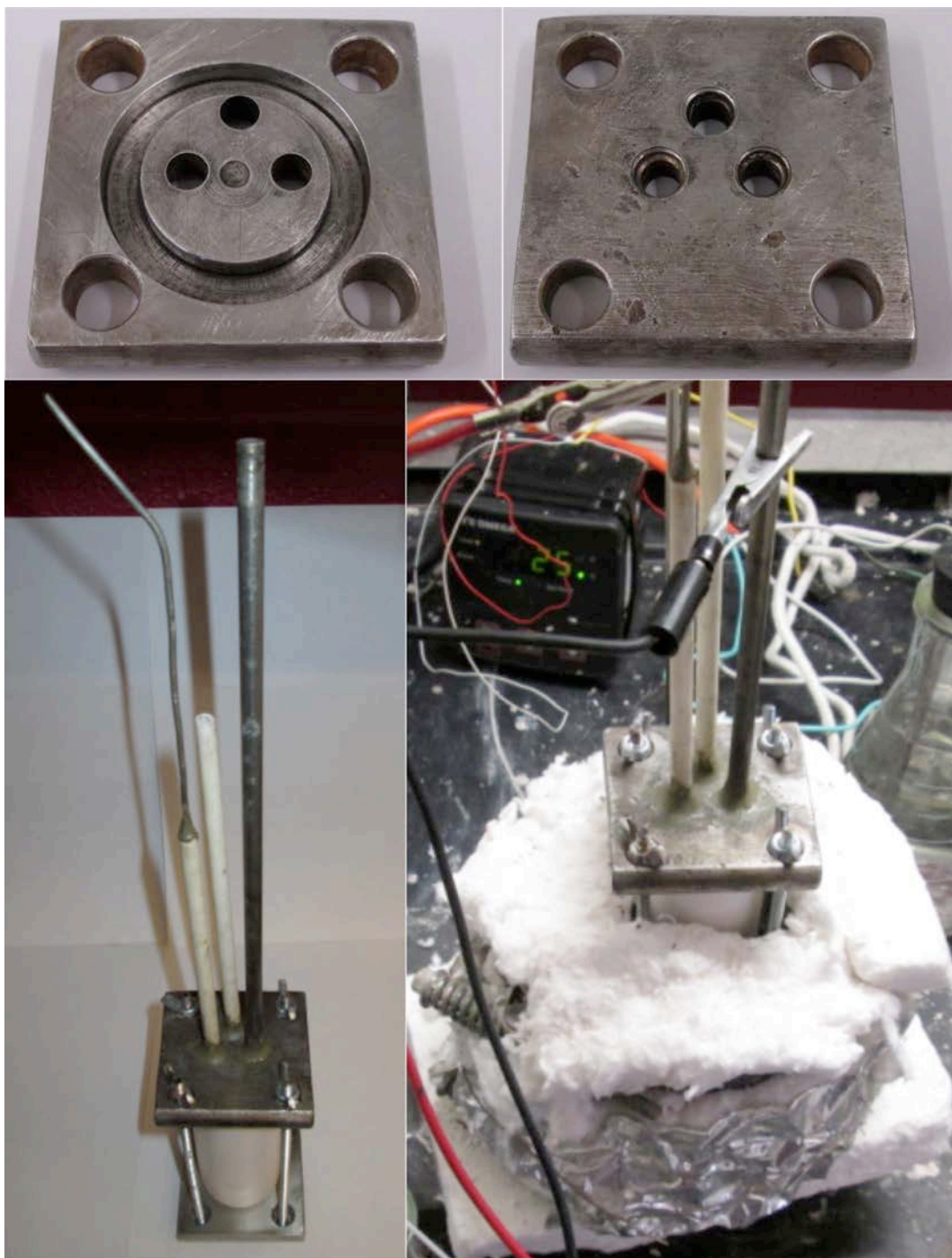


Fig. S1. The single chamber electrolysis cell configuration as described in the text and used to confirm that ammonia was produced at the cathode and oxygen at the electrode. Top left and right photos: underside and top of cell cover. Bottom left: alumina crucible situated in the cover groove and bolted closed. Above the cell, from left to right is the electrical connection of the anode that is sheathed in alumina, the alumina gas outlet, and on the right side an Inconel tube functioning as both the gas inlet & the cathode electrical connection. Bottom, right: the electrolyzer sitting within the band heater (not visible) and surrounded by insulation.

Table S1. Measured ammonia produced as a function of time in the Fig. S1 electrolysis cell at either 0 or 20 mA applied current and at 200°C in a molten Na/KOH electrolyte. In the table NH₃ is the mg of measured NH₃ analyzed as detailed in the text. EE is the electrolysis efficiency, that is NH₃/3e⁻ (%) calculated from the charge, q, and measured ammonia as: 100%*mol NH₃/(q /3). In the case of q =0, EE =NH₃ (measured). Nano-Fe₂O₃ above the electrolyte (columns 14 & 15) is maintained in the headspace, and kept separate from the electrolyte by fiber alumina wool. Specifically, three cm above the molten electrolyte a platform was formed in the headspace of the electrolysis chamber which consisted of (i) Ni shim pierced with holes and covering the diameter of the alumina crucible, (ii) fine (400) 316 stainless mesh, and (iii) Cotronics 300 porous alumina paper with through holes for the alumina tubes covering the electrodes, (iv) then the nano-Fe₂O₃, (v) a top layer of Cotronics 300 porous alumina paper, and finally packed with (vi) high temperature fiber alumina wool (McMaster 9379K93 with foil-face removed).

current: I = 0 mA		I = 20 mA		macro-Fe ₂ O ₃		nano-Fe ₂ O ₃ , above,		nano-Fe ₂ O ₃								
additive: nano-Fe ₂ O ₃						Ar preheated						not in, electrolyte				
inlet gas: wet N ₂		wet N ₂		wet Ar		wet Ar		dry N ₂		wet N ₂		wet N ₂		wet air		
Time (hr)	NH ₃	q, Faraday	NH ₃	EE	NH ₃	EE	NH ₃	EE	NH ₃	EE	NH ₃	EE	NH ₃	EE	NH ₃	EE
0	0 mg	0.00E+00	0 mg	0%	0.00	0%	0.00	0%	0.00	0%	0.00	0%	0.00	0%	0	0%
1	0 mg	7.46E-04	0 mg	0%	0.02	0.6%	0.00	0%	0.75	17.7%	0.94	22.2%	0.00	0%	0.84	19.9%
2	0 mg	7.46E-04	0 mg	0%	0.06	1.4%	0.00	0%	0.78	18.5%	1.06	25.1%	0.00	0%	1.05	24.8%
3	0 mg	7.46E-04	0 mg	0%	0.08	1.9%	0.00	0%	0.25	5.9%	1.33	31.5%	0.00	0%	1.29	30.5%
4	0 mg	7.46E-04	0 mg	0%	0.04	1.0%	0.00	0%	0.10	2.4%	1.48	35.0%	0.00	0%	1.46	34.4%
5	0 mg	7.46E-04	0 mg	0%					0.09	2.2%	1.47	34.8%			1.45	34.3%
6	0 mg	7.46E-04	0 mg	0%					0.08	2.0%	1.42	33.5%			1.41	33.4%

A second, double chamber cell is shown in Fig. S2. An alumina crucible (not shown) sits in the outer groove of the cell cover, while an inner alumina tube sits in the inner groove. The outer chamber, situated between the crucible and the inner alumina tube contains an Inconel tube (left side) which functions both as an inlet of water saturated air or nitrogen, and as an electrical connector for the nickel 400 mesh cathode. The outer chamber also contains an alumina tube outlet to one (of two) water traps for gas analysis. The inner chamber, situated within the alumina tube, contains the nickel anode connected externally by a nickel wire sheathed in an alumina tube, as well as a second alumina tube outlet to the second water trap for gas analysis. This configuration exhibits higher cell voltages due to the long electrolyte path between anode and cathode and was only used to confirm that ammonia was produced at the cathode and oxygen at the anode. While this configuration exhibits higher cell voltages, it is interesting to note that we never observed an improvement in efficiency (that is we did not observe an increase in the ammonia produced) in these experiments in which oxygen was partially (with air as the inlet gas) or fully (with nitrogen as the inlet gas) excluded from the cathode chamber, which suggested that there is no observable reaction of ammonia with oxygen in the 200°C molten hydroxide electrolyte.



Fig. S2. The double chamber electrolysis cell configuration as described in the text and used to confirm that ammonia was produced at the cathode and oxygen at the electrode. Top left and right photos: underside and top of cell cover. Bottom photos, left: alumina tube with cathode outside and anode inside, prior to addition of electrolyte and outer crucible. Right: Double chamber cell prior to closure with bolts showing from right to left inconel tube for gas inlet & cathode electrical connection, outer chamber gas outlet, inner chamber electrical connection to anode, and inner chamber gas outlet.

The electrolyzer current was supplied by power supply in initial experiments and is now provided by an efficient concentrator photovoltaic in lab under 1 kW Xenon, daylight color (5600K) AM1(air mass) illumination as described in Fig. S3.

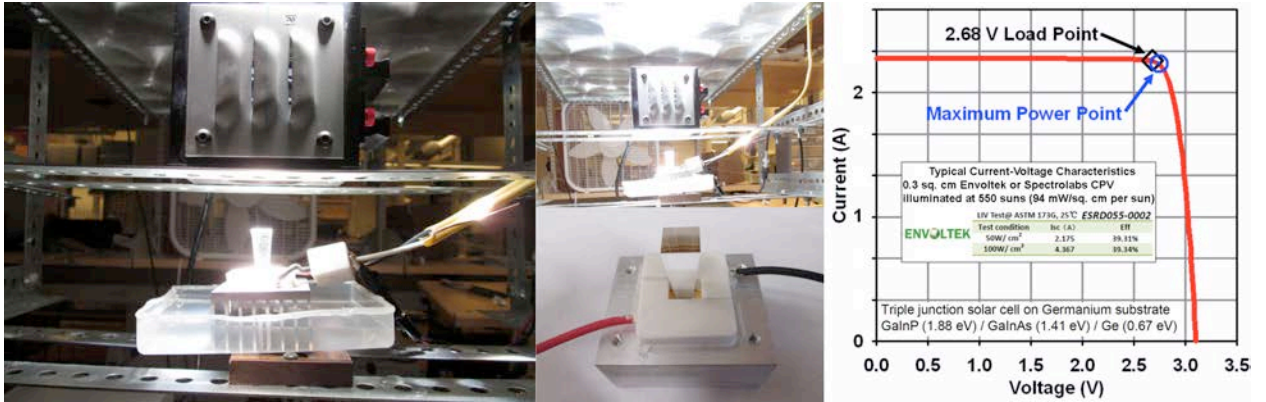
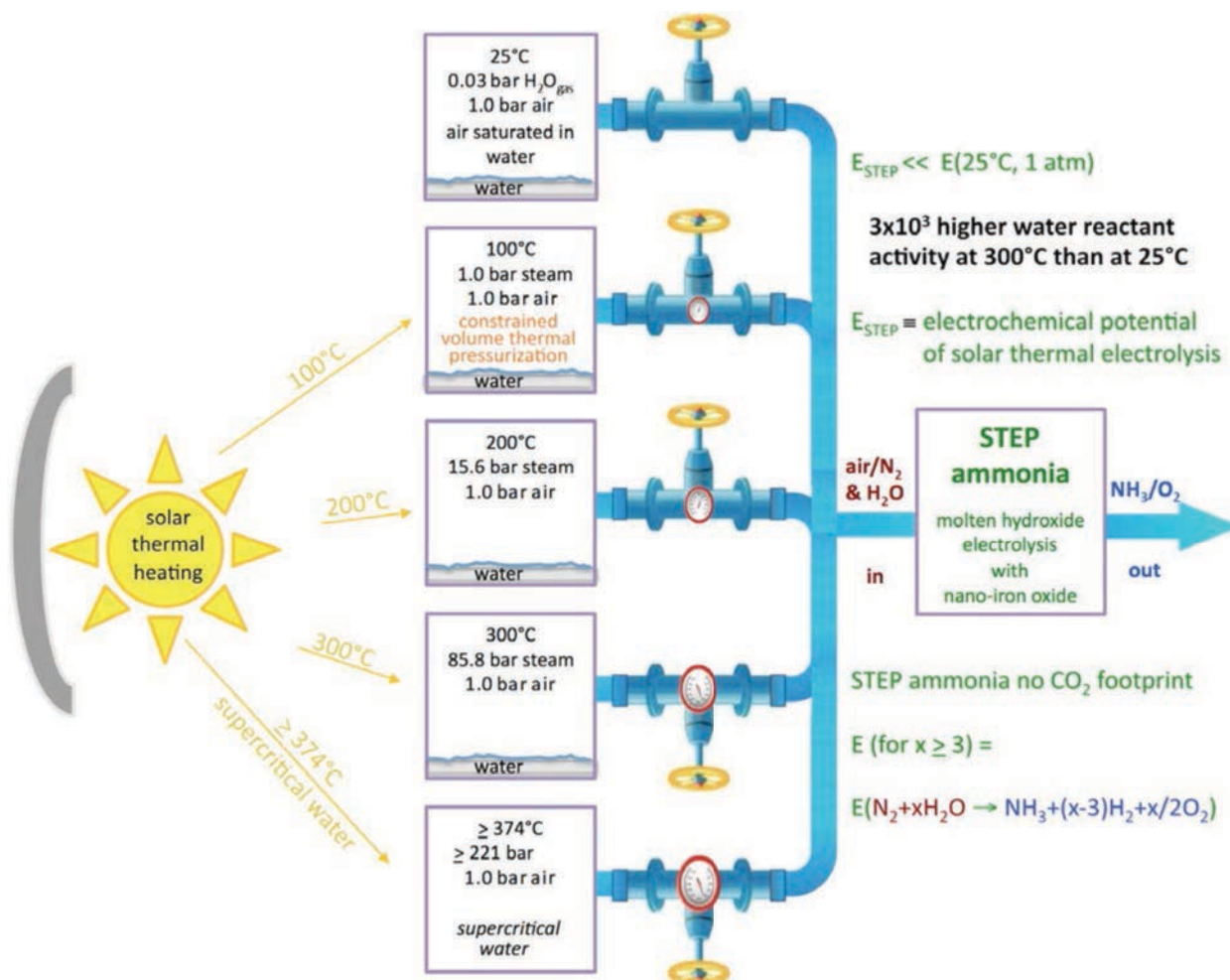


Fig. S3. Electrolyzer current by power supply (initial experiments) and now provided by an efficient concentrator photovoltaic in lab under 1 kW Xenon, daylight color (5600K) AM1(air mass) illumination. Left side is the 0.3074 cm² Envoltek ESRD055 CPV situated under the air-cooled AM1 filter. Middle top: The fresnel concentrator above the AM 1 filter. Middle bottom: the unattached CPC under the secondary optical concentrator. Right side: Typical (550 sun) photocurrent - voltage plot of the CPV.

Solar Thermal Constrained Volume Pressurization

A low energy route to solar energy conversion. In this study we also introduce a solar thermal water self-pressurizing, low electrolysis energy path system. The solar generated high pressure of the reactant gas phase equilibrates with gas or molten phase reactants to decrease the electrochemical potential required for endothermic electrolyses. Sunlight provides the energy to evaporate a reactant in a constrained volume, driving the reactant to high pressure as shown (for H₂O) in Scheme S1 (alternatively, the higher pressure H₂O can be used to compress a piston to pressurize a reactant such as N₂ in air). The sunlight also provides higher temperature, which further decreases the electrolysis splitting energy. Solar thermal energy is readily absorbed at conversion efficiency in excess of 65%, and here provides an efficient energy source and mechanism to maintain a high reactant pressure. Hence the energy needed to split water or electrochemically synthesize molecules can be substantially decreased by sunlight. Specifically here, pure water or an NaOH:KOH electrolyte, was enclosed with air and heated in a confined volume.



Scheme S1. The pressure of water saturating 1 bar of air, without or with solar heating in a constrained volume, as a feedstock for STEP ammonia production. Note, that dry air's composition is 78.08% N₂, 20.95% O₂, 0.93% Ar, and other lower concentration gases; alternatively a pure N₂ feedstock can be considered instead of air.

As expected, heating volume constrained water yielded a demonstrated increase in water pressure from 0.03 bar at room temperature to 60 bar at 275°C measured in the 200 ml constrained volume experimental cell (a modified hydrothermal reaction chamber) shown in Fig. S4. The generated high water pressure is in accord with improved high Q /low energy ammonia synthesis conditions theoretically predicted by Eq 7 & 8, seen in the lower voltage curve of Fig. 1 of the main text.



Fig. S4. High-pressure cell used to measure saturated water pressure as a function of temperature. The Tech-zoom stainless steel reactor has an inner 200ml Teflon chamber (top shown as used to measure saturated water pressure), and (bottom) is shown as in-house modified for electrolysis by replacement of the right-hand flow valve with throughput electrical contacts using an OMEGA MFT-116-3 Feedthrough for up to three 1/16" diameter probes with a 1/4" NPTM fitting.

In addition to water as shown in Scheme S1, we directly heated water/hydroxide mixtures in the Fig. S4 modified hydrothermal reaction chamber shown in the Methods section. Pure water in a constrained environment will achieve a pressure of 85.8 bar at 300°C (31). As seen in Fig. S5, a KOH mix containing 50% water (an 18m KOH aqueous solution) will achieve 30 bar in a constrained environment (a substantial portion of the water is bound by the KOH). The 1:1 molar NaOH:KOH used in the main portion of this study is a low melting point eutectic but at 1 bar retains relatively low concentrations of water (<8%) at 200°C. In order to achieve water-saturation pressures that can decrease the electrolysis energy, higher concentrations of water are required. As seen in the figure we measure that a 1:1 molar ratio of NaOH to KOH when containing 67 % water (an aqueous solution that is 4 molal in both NaOH and KOH) does rise to a water pressure of over 50 bar when heated to 300°C. In comparison, as seen in the figure, the variation with temperature of this saturated water pressure is similar, but slightly less, than that previously observed above pure 8 m NaOH or pure 8 m KOH solutions.

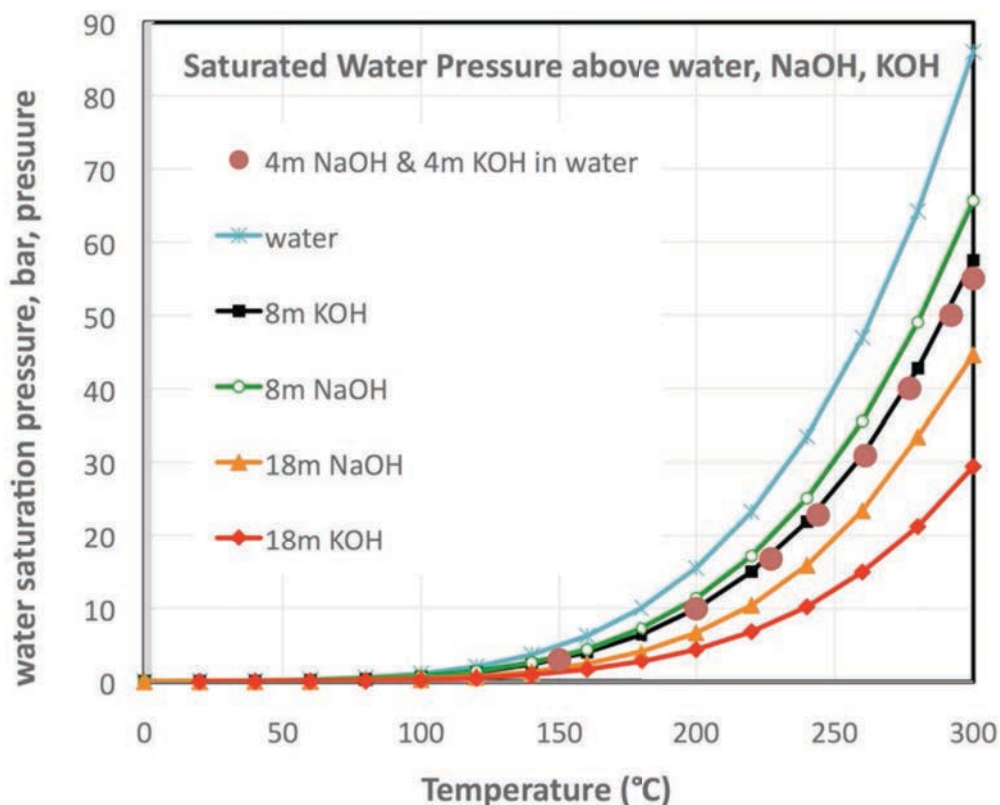


Fig. S5. The measured water pressure above a 4 molal NaOH + 4 molal KOH aqueous solution (a mix containing a 1:1 molar ratio of NaOH to KOH and 72.2 mass percent water) compared to the known (31) experimental saturated water pressures above water, 8 or 18 m NaOH, and 8 or 18 m KOH.

In principle, the heat required to raise the aqueous hydroxide mix is low (the heat capacity for water, NaOH and KOH varies from $C_p = 1$ to $4 \text{ J g}^{-1} \text{ K}^{-1}$ with temperature). To safely constrain the pressure, the Teflon lined stainless steel 200 ml reaction chamber used in this study is massive (5 kg) compared to the 70g mass of the heated hydroxide

solution, which provides a challenge to heating the chamber solely with solar energy. However demonstrating that solar thermal is sufficient, is that outdoors 60 to 70 g of an alkali eutectic salt consistently reaches and sustains temperatures of 500°-700°C, and 30 g reaches over 700°C, with (Edmund Optics) Fresnel lens concentrator under Washington DC sunlight.

We kept the temperature of Fig. S4 high-pressure cell at or below 300°C, as the decomposition temperature of Teflon is 325°C. We observe that the Teflon lining began to soften or deform at temperatures over 300°C. In accord with Scheme S1, high water content, closed contained electrolyses provide an opportunity to increase the saturated water pressure above the mNolten phase reaction by three orders of magnitude by increasing the temperature from 25°C to 300°C. These conditions provide the opportunity to explore the capability of solar thermal energy to decrease the electrolysis potential needed to drive water reactant electrolyses such in the ammonia synthesis reactions Eqs. 4-8.

In experiments in the volume constrained cell with externally connected electrodes shown on the right side of Fig. S4, the potential between Ni electrodes in an 8 m hydroxide ammonia synthesis electrolyte (4m NaOH, 4 m KOH, nano-Fe₂O₃) decreased with increasing temperature providing initial supporting evidence of the predicted high Q, low potential ammonia synthesis potential calculated in Fig. 1 of the main text. Specifically at 250°C and 25 bar under volume constrained conditions using the Fig. S4 cell, measured electrolysis potentials are lower than those measured at atmospheric pressure and lower temperature, and the ammonia generation rate and current efficiency is higher. Measured potentials over the 10 cm² electrodes at higher temperature and pressure were 0.78V at 1 mA, 1.01V at 20 mA (compared to 1.23V at ambient pressure and 200°C), and 1.31V at 250 mA (compared to 1.44V at ambient pressure and 200°C). The cell was then maintained at 20 mA (2 mA cm⁻²) for 10 hours, and regularly (every ~2 hours) vented through a sparger/water trap to analyze for ammonia and the gas analyzed for hydrogen. Compared to the 200°C, 1 atm experimental results, the 250°C, 25 bar results require significantly lower electrolysis voltage, while coulombic efficiency and peak ammonia rate are the same 35% and 2.4 x 10⁻⁹ mol NH₃ cm⁻² s⁻¹. Interestingly however, no hydrogen co-product was detected during the course of the experiment. At 250°C and 25 bar the ammonia production rate varied with time as 2.1 x 10⁻⁹ (hours 0 to 2.5), 2.2 x 10⁻⁹ (hours 2.5 to 5), 2.4 x 10⁻⁹ (hours 5 to 8), and then dropped to 1.6 x 10⁻⁹ (hours 8 to 10). In each case the pressure increased from 25 bar prior to venting. The cell was allowed to increase in pressure to 39 bar subsequent to the first vent/ammonia analysis, and then vented at 35 to 36 bar subsequently through 8 hours of electrolysis time. During hours 8 to 10, the rate of pressure build-up in the cell slowed and only increased from 25 to 28 bar during this two hour interval. Concurrent with the measured decrease in ammonia rate during this time interval was an increase in voltage (from 1.01 V to 1.11V).

As expected, we observe that using water evaporation in a closed container increases the electrolysis cell pressure, and in addition we observe that this induces a significant decrease in the energy (electrolysis voltage) measured to drive ammonia production. It should be noted that the lack of an observed hydrogen co-product at high pressure during ammonia synthesis at 2 mA cm⁻² represents a loss of this fuel as a co-product.

References

1. V. Smil, *Enriching the Earth: Fritz Haber, Carl Bosch, and the Transformation of World Food Production* (MIT Press, Cambridge, MA, 2004).
2. J. Rockström, W. Steffen, K. Noone, A. Persson, F. S. Chapin 3rd, E. F. Lambin, T. M. Lenton, M. Scheffer, C. Folke, H. J. Schellnhuber, B. Nykvist, C. A. de Wit, T. Hughes, S. van der Leeuw, H. Rodhe, S. Sörlin, P. K. Snyder, R. Costanza, U. Svedin, M. Falkenmark, L. Karlberg, R. W. Corell, V. J. Fabry, J. Hansen, B. Walker, D. Liverman, K. Richardson, P. Crutzen, J. A. Foley, A safe operating space for humanity. *Nature* **461**, 472–475 (2009). [Medline doi:10.1038/461472a](#)
3. R. Strait, M. Nagvekar, Carbon dioxide capture and storage in the nitrogen and syngas industries. *Nitrogen+Syngas* **303** (Jan.-Feb.), 1–3 (2010); www.kbr.com/Newsroom/Publications/Articles/Carbon-Dioxide-Capture-and-Storage-in-the-Nitrogen-Syngas-Industries.pdf.
4. A. Bonomi, M. Hadat, C. Gentaz, Galvanic cell studies on ionic carbide and nitride solutions in molten salts. *J. Electrochem. Soc.* **124**, 982–986 (1977). [doi:10.1149/1.2133513](#)
5. A. Bonomi, M. Hadat, F. Breda, Electrochemical studies on ionic nitride solutions in molten salts. *J. Electrochem. Soc.* **126**, 248–251 (1979). [doi:10.1149/1.2129013](#)
6. T. Murakami, T. Nishikiori, T. Nohira, Y. Ito, Electrolytic synthesis of ammonia in molten salts under atmospheric pressure. *J. Am. Chem. Soc.* **125**, 334–335 (2003). [Medline doi:10.1021/ja028891t](#)
7. Y. Ito, T. Goto, Electrochemistry of nitrogen and nitrides in molten salts. *J. Nucl. Energy* **344**, 128–135 (2005).
8. T. Murakami, T. Nohira, Y. H. Ogata, Y. Ito, Electrolytic ammonia synthesis in molten salts under atmospheric pressure using methane as a hydrogen source. *Electrochem. Solid-State Lett.* **8**, D12–D14 (2005). [doi:10.1149/1.1870633](#)
9. T. Murakami, T. Nohira, Y. Araki, T. Goto, R. Hagiwara, Y. H. Ogata, Electrolytic synthesis of ammonia from water and nitrogen under atmospheric pressure using a boron-doped diamond electrode. *Electrochem. Solid-State Lett.* **10**, E4–E6 (2007). [doi:10.1149/1.2437674](#)
10. N. Serizawa, H. Miyashiro, K. Takei, T. Ikezumi, T. Nishikiori, Y. Ito, Dissolution behavior of ammonia electrosynthesized in molten LiCl–KCl–CsCl system. *J. Electrochem. Soc.* **159**, E87–E91 (2012). [doi:10.1149/2.099204jes](#)
11. C. J. Pickett, J. Talarmin, Electrosynthesis of ammonia. *Nature* **317**, 652–653 (1985). [doi:10.1038/317652a0](#)
12. N. Furuya, H. Yoshiba, Electroreduction of nitrogen to ammonia on gas diffusion electrodes loaded with inorganic catalysts. *J. Electroanal. Chem.* **291**, 269–272 (1990). [doi:10.1016/0022-0728\(90\)87195-P](#)
13. E. Skúlason, T. Bligaard, S. Gudmundsdóttir, F. Studt, J. Rossmeisl, F. Abild-Pedersen, T. Vegge, H. Jónsson, J. K. Nørskov, A theoretical evaluation of

- possible transition metal electro-catalysts for N₂ reduction. *Phys. Chem. Chem. Phys.* **14**, 1235–1245 (2012). [Medline doi:10.1039/c1cp22271f](#)
14. I. Amar, R. Lan, C. Petit, S. Tao, Solid-state electrochemical synthesis of ammonia: A review. *J. Solid State Electrochem.* **15**, 1845–1860 (2011). [doi:10.1007/s10008-011-1376-x](#)
 15. A. Skodra, M. Stoukides, Electrocatalytic synthesis of ammonia from steam and nitrogen at atmospheric pressure. *Solid State Ion.* **180**, 1332–1336 (2009). [doi:10.1016/j.ssi.2009.08.001](#)
 16. V. Kordali, G. Kyriacou, C. Lambrou, Electrochemical synthesis of ammonia at atmospheric pressure and low temperature in a solid polymer electrolyte cell. *Chem. Commun. (Camb.)* **2000**, 1673–1674 (2000). [doi:10.1039/b004885m](#)
 17. R. Lan, J. T. S. Irvine, S. Tao, Synthesis of ammonia directly from air and water at ambient temperature and pressure. *Sci. Rep.* **3**, 1145 (2013). [Medline doi:10.1038/srep01145](#)
 18. R. Lan, S. Tao, Electrochemical synthesis of ammonia directly from air and water using a Li⁺/H⁺/NH₄⁺ mixed conducting electrolyte. *RSC Adv.* **3**, 18016–18021 (2013). [doi:10.1039/c3ra43432j](#)
 19. J. R. McKone, S. C. Marinescu, B. S. Bruneschwig, J. R. Winkler, H. B. Gray, Earth-abundant hydrogen evolution electrocatalysts. *Chem. Sci.* **5**, 865–878 (2014). [doi:10.1039/c3sc51711j](#)
 20. D. Santos, C. A. C. Sequeira, J. L. Figueiredo, Hydrogen production by alkaline water electrolysis. *Quím. Nova* **8**, 1176–1193 (2013). [doi:10.1590/S0100-40422013000800017](#)
 21. K. Zeng, D. Zhang, Recent progress in alkaline water electrolysis for hydrogen production and applications. *Progr. Energy Combust. Sci.* **36**, 307–326 (2010). [doi:10.1016/j.pecs.2009.11.002](#)
 22. J. Ganley, An intermediate-temperature direct ammonia fuel cell with a molten alkaline hydroxide electrolyte. *J. Power Sources* **178**, 44–47 (2008). [doi:10.1016/j.jpowsour.2007.11.093](#)
 23. J. Ganley, High temperature and pressure alkaline electrolysis. *Int. J. Hydrogen Energy* **34**, 3604–3611 (2009). [doi:10.1016/j.ijhydene.2009.02.083](#)
 24. S. Licht, L. Halperin, M. Kalina, M. Zidman, N. Halperin, Electrochemical potential tuned solar water splitting. *Chem. Commun. (Camb.)* **2003**, 3006–3007 (2003). [Medline doi:10.1039/b309397b](#)
 25. M. W. Chase, *J. Phys. Chem. Ref. Data* **9**, 1 (1998).
 26. Thermochemical data from (25) are available online at U.S. National Institute of Standards and Technology ChemWeb: <http://webbook.nist.gov/chemistry/form-ser.html>.

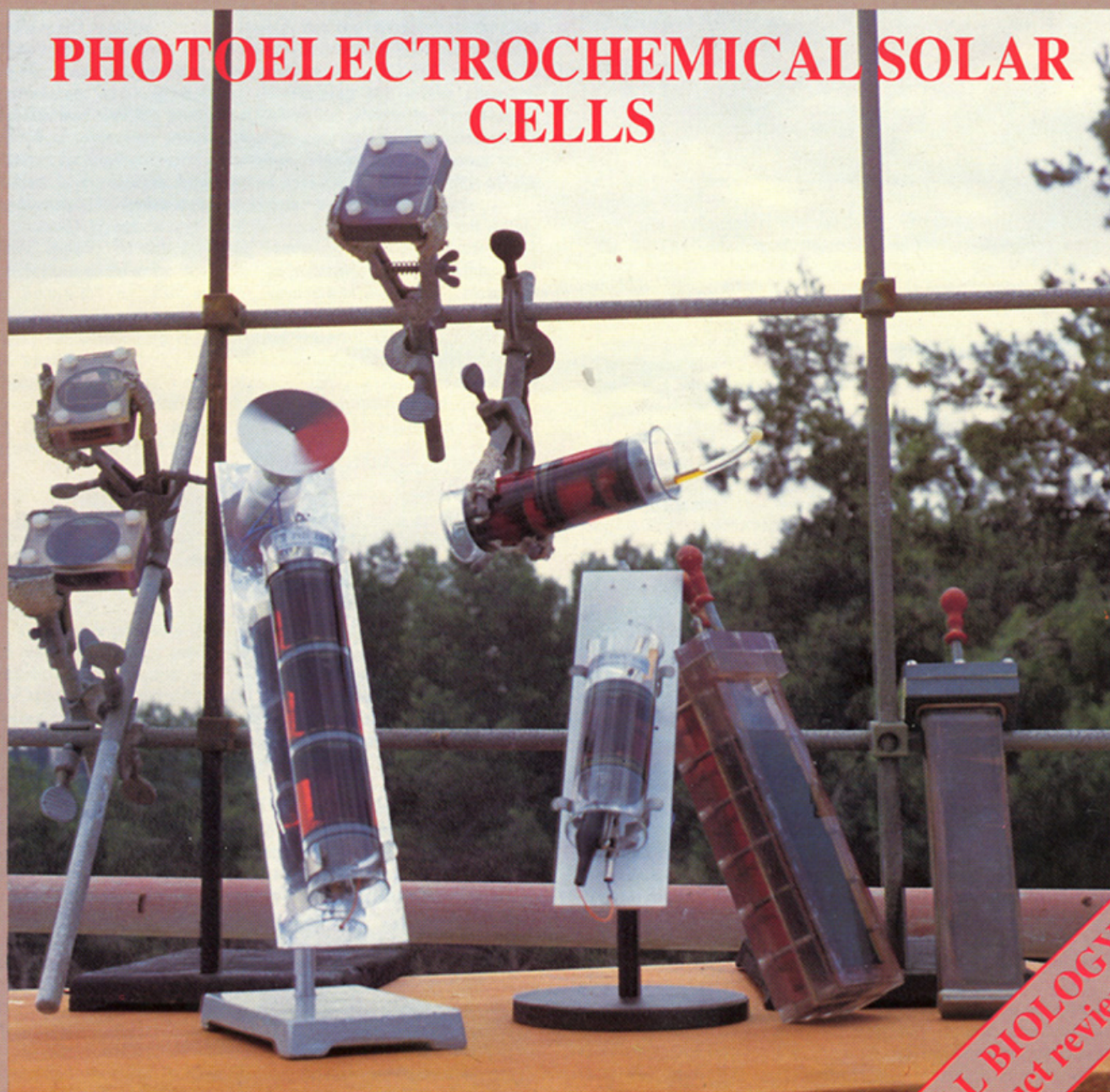
27. Glenn Research Center, National Aeronautics and Space Administration (NASA), ThermoBuild access to NASA Glenn thermodynamic CEA database (2006); data available at www.grc.nasa.gov/WWW/CEAWeb/ceaThermoBuild.htm.
28. S. Licht, STEP (solar thermal electrochemical photo) generation of energetic molecules: A solar chemical process to end anthropogenic global warming. *J. Phys. Chem. C* **113**, 16283–16292 (2009). [doi:10.1021/jp9044644](https://doi.org/10.1021/jp9044644)
29. A. Pelton, K. Hack (and codevelopers), *283 binary salt phase diagram*, [Facility for the Analysis of Chemical Thermodynamics (FACT), Centre for Research in Computational Thermochemistry (CRCT), University of Montreal, rev. ed., 2012]; www.crct.polymtl.ca/FACT/documentation/FTsalt/FTsalt_Figs.htm.
30. Materials and methods are detailed in the supplementary materials on *Science Online*.
31. A. Hellman, E. J. Baerends, M. Biczysko, T. Bligaard, C. H. Christensen, D. C. Clary, S. Dahl, R. van Harreveld, K. Honkala, H. Jonsson, G. J. Kroes, M. Luppi, U. Manthe, J. K. Nørskov, R. A. Olsen, J. Rossmeisl, E. Skúlason, C. S. Tautermann, A. J. Varandas, J. K. Vincent, Predicting catalysis: Understanding ammonia synthesis from first-principles calculations. *J. Phys. Chem. B* **110**, 17719–17735 (2006). [Medline doi:10.1021/jp056982h](https://pubmed.ncbi.nlm.nih.gov/16711111/)
32. M. Appl, Ammonia 2 production processes, *Ullman's Encyclopedia of Industrial Chemistry* (Wiley-Verlag, Weinheim, Germany, ed. 7, 2012), pp. 139–210; doi: 10.1002/14356007.
33. S. Licht, Efficient solar-driven synthesis, carbon capture, and desalination, STEP: Solar thermal electrochemical production of fuels, metals, bleach. *Adv. Mater.* **47**, 5592–5612 (2011). [Medline doi:10.1002/adma.201103198](https://pubmed.ncbi.nlm.nih.gov/211103198/)
34. R. Pitz-Paal, in *Solar Energy Conversion and Photoenergy Systems*, J. B. Galvez, S. M. Rodriguez, Eds. (EOLSS Publishers, Oxford, 2007).
35. T. Hahm, H. Schmidt-Traub, B. Leßmann, A cone concentrator for high-temperature solar cavity-receivers. *Sol. Energy* **65**, 33–41 (1999). [doi:10.1016/S0038-092X\(98\)00119-4](https://doi.org/10.1016/S0038-092X(98)00119-4)
36. W. Ziqing, Z. Kiuming, L. Jianxin, W. Rong, W. Kemei, Preparation and application of nanometer materials supported ruthenium catalysts. *J. Catal.* **33**, 377–378 (2013).

nature

INTERNATIONAL WEEKLY JOURNAL OF SCIENCE

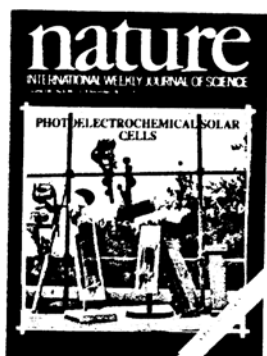
Volume 330 No.6144 12-18 November 1987 £1.95

PHOTOELECTROCHEMICAL SOLAR CELLS



Cover Article: "A Description of Energy Conversion in Photoelectrochemical Solar Cells" by Stuart Licht

CELL BIOLOGY
product review



nature

12 November 1987
Vol. 330 Issue no. 6144

A variety of liquid solar cells operating from a roof-top laboratory. Each cell contains an aqueous polysulphide electrolyte and an *n*-cadmium chalcogenide semiconductor. The chemical mechanism of energy conversion in these cells is described on page 148.

A description of energy conversion in photoelectrochemical solar cells

Stuart Licht*

Department of Materials Research, The Weizmann Institute of Science, Rehovot 76100, Israel

Photoelectrochemical cells (PECs) provide alternatives to conventional solid-state solar cells. Since the discovery in 1976, the *n*-cadmium chalcogenide/aqueous polysulphide photoelectrochemical cell, *n*-CdX/S_j²⁻ PEC, has been the most studied and in some ways the most promising of these liquid solar cells^{1,2}, and can combine photoelectrochemical conversion with electrochemical storage³ in a system competitive in overall efficiency with the best comparable solid-state systems. But despite hundreds of studies, neither the reactive chemical species nor the chemical mechanism of operation is known. Here a complete description of the radiative to electrical energy conversion process in *n*-CdX/S_j²⁻ systems is introduced, accomplished by determining the active chemical species and limiting photoelectrochemical processes. Two distinct chemical processes control energy conversion. Photocurrent is limited by supersulphide adsorption. Maximum photopower utilization is desorption limited and related to the activity of the hydrosulphide, hydroxide and shorter polysulphide species.

Photoelectrochemical studies have often focused on solid-state aspects of the systems, accessing available models for analogous solid-state devices. The polysulphide electrolyte used in the *n*-CdX/S_j²⁻ PEC system, formed by the simple dissolution of a sulphide salt and sulphur in water, is known to be highly complex, containing H⁺ and other cations⁴, OH⁻, H₂S, S²⁻, the polysulphides (S_j²⁻ (*j* = 2 to 5)) (refs 5,6), supersulphide⁷ (S₂⁻), thiosulphate (S₂O₃²⁻) and sulphate⁶ (SO₄²⁻). As a result of this complexity the overall mechanism of photoinduced oxidation in the *n*-CdX/S_j²⁻ system has remained unknown, but was generally simplified as



Only recently has the emphasis shifted to a pure solution-chemistry investigation of *n*-CdX/S_j²⁻ PECs, leading to some of the highest solar-to-electrical conversion efficiencies in PECs⁸

and to the demonstration of the long-term stability of thin-film solar cells⁹.

This study presents short-circuit photocurrent, *I*_{sc}, radiative-to-electrical energy conversion efficiency, η , and fill factor, *f*_i, reflecting the portion of the attainable power accessed, for a *n*-CdSe_{0.65}Te_{0.35} single-crystal photoelectrode immersed in two series of aqueous caesium polysulphide electrolytes, which are measured using a described experimental procedure^{4,8}. Caesium, compared with other polysulphide electrolytes, improves *n*-CdX/S_j²⁻ PEC characteristics⁴.

Figures 1 and 2 summarize the photoelectrochemical and chemical conditions in *n*-CdX/S_j²⁻ PECs using a series of polysulphide electrolytes with consistent hydrosulphide activities and varying pH. These figures include the calculated complex equilibrium distribution of (poly)sulphide chemical species in these electrolytes. In these solutions, at room temperature, spontaneous polysulphide/thiosulphate disproportionation is not significant. Figure 3 summarizes the photoelectrochemical effects in a second series of polysulphide electrolytes containing a nearly constant environment of tetrasulphide and supersulphide.

As Fig. 1 shows, an electrolyte that tends to shift electrolyte composition away from maximum tetrasulphide and supersulphide activities tends to suppress photocurrent. The close linear proportionality of supersulphide activity with short-circuit photocurrent contrasts strongly with the extreme (exponential) variations of most of the sulphide and polysulphide species in solution in Fig. 2. Depletion of the species to be oxidized below an activity level sufficient to utilize photogenerated holes will reduce *n*-CdX/S_j²⁻ photocurrent. These photocurrent losses will tend to be greatest under conditions of maximum band bending (maximum photocurrents). A chemical species whose activity varies linearly with *I*_{sc} is closely related to the process of photoinduced oxidation in *n*-CdX/S_j²⁻.

The importance of the adsorption process in *n*-CdX/S_j²⁻ PECs has been well documented^{1,2}. Supersulphide, rather than tetrasulphide, is likely to be the direct oxidation participant due to: (1) the more proportional relation of *I*_{sc} to supersulphide activity, rather than tetrasulphide activity (see Fig. 1); (2) the higher probability of a one-hole, rather than a two-hole, oxidative process; and (3) comparison of the known temperature dependence of the species distribution in the electrolyte with *I*_{sc}. *n*-CdX/S_j²⁻ *I*_{sc} increases smoothly with temperature¹⁰. Supersulphide displays this smooth increase in activity with temperature⁷, whereas the polysulphide formation equilibrium constants are temperature-insensitive⁵.

* Present address: Department of Chemistry, Room 6-427, Massachusetts Institute of Technology, Cambridge, Massachusetts 02139, USA.

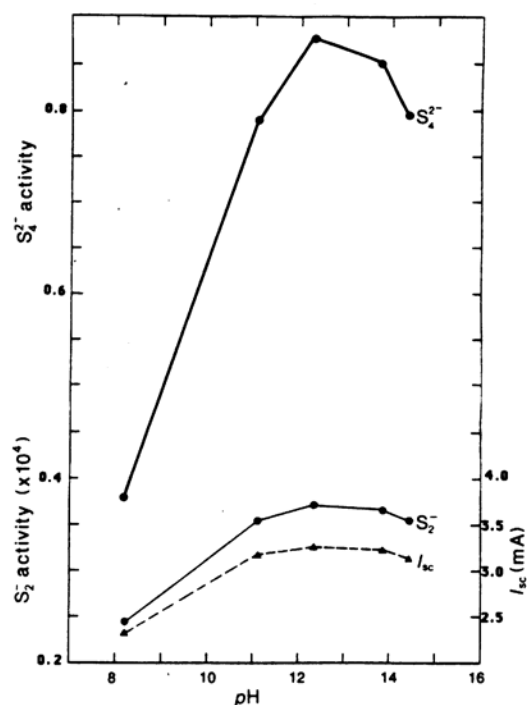
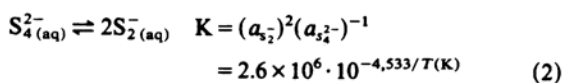


Fig. 1 The variation of supersulphide and tetrasulphide activities and the short-circuit photocurrent I_{sc} , for a 0.15-cm^2 $n\text{-CdSe}_{0.65}\text{Te}_{0.35}$ single crystal immersed in an aqueous electrolyte containing Cs_2S (1.0 mol per kg H_2O), CsHS (0.8 mol per kg H_2O) and sulphur (3 mol per kg H_2O) at various pH values, under an incident filtered tungsten-halogen illumination of 75 mW cm^{-2} . The crystal was mounted with the (0001) plane exposed, and pretreated with mechanical polishing, chemical etching in aqua regia, rinsing in polysulphide and cyanide solutions to remove excess selenium or tellurium, and photoelectrochemical etching in HCl. A 665-nm cutoff filter eliminated differences in light absorption of polysulphide solutions at shorter wavelengths. The pH was varied from an equilibrium value of 12.35 by addition of either H_2S or CsOH to the solution. Chemical activities were calculated by using equilibrium constants^{5,7} at 298 K, in a prescribed manner⁶.

Equilibrium concentrations of the supersulphide species are small, $\sim 10^{-5}$ mol kg^{-1} at room temperature, and insufficient to maintain mass transport at the high current densities measured. However, sufficient tetrasulphide will maintain supersulphide activity, preventing supersulphide depletion at the electrode surface and facilitating the adsorption and oxidation of supersulphide on the surface, M:



In Fig. 3 the nearly constant I_{sc} is again consistent with a constant S_2^{2-} activity, as in equations (3, 4).

Other data appear consistent with the process proposed in equations (2-4). Tetrasulphide was an important participant in $n\text{-CdX/S}_j^{2-}(\text{aq})$ oxidative processes¹¹⁻¹³. Loss of polysulphide in solution by disproportionation resulted in PECs of lowered efficiency^{6,9}. Hamilton and Woods¹⁴ provided evidence for an adsorbed species containing two sulphur atoms, tentatively identified as disulphide, S_2^{2-} , as active in the electrochemical oxidation of sulphide on gold. Lessner *et al.*¹⁵ suggested that supersulphide was a direct participant in the oxidation of polysulphide on cobalt, but their analysis incorrectly excluded adsorptive processes from their model¹⁶.

A significant increase in f_r , to >0.5 , parallels increases in

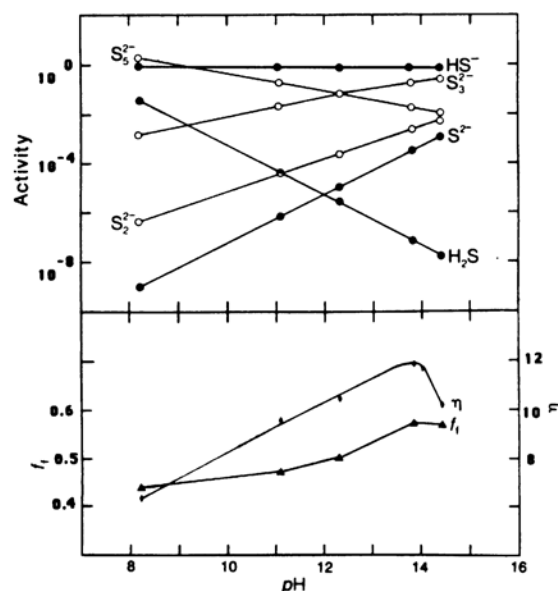
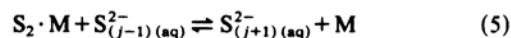


Fig. 2 The variation of fill factor, f_r , solar-electrical conversion efficiency, η , and the distribution of chemical species for a 0.15-cm^2 $n\text{-CdSe}_{0.65}\text{Te}_{0.35}$ single crystal prepared and measured under the conditions described in the legend to Fig. 1. The polysulphide data are shown as open circles, and the hydrogen sulphide, hydrosulphide and sulphide data are shown as solid circles.

hydroxide, disulphide and trisulphide activities (Fig. 2) and hydroxide and hydrosulphide activity (Fig. 3). The depletion of supersulphide activity has a primary effect on photocurrent (Fig. 1) with no relation to the diminishing f_r seen in Figs 2 and 3. Large f_r are maintained only at hydrosulphide and hydroxide activities >0.5 .

At maximum PEC power, band bending is intermediate between the flat band potential and the strong conduction and valence-band bending occurring at I_{sc} . The electrical gradient accelerating holes to the electrode surface is smaller at maximum power than at I_{sc} . As Fig. 3 shows, supersulphide activities are consistently sufficient to maintain high photocurrents. Despite this availability of reductant, the less-reactive holes occurring at maximum power will have a lower probability of favourable (non-corrosive) reaction if the oxidation product tends to accumulate at the electrode surface. As shown, hydroxide and hydrosulphide depletions have a strong effect on f_r , measured at this point of maximum power. This is symptomatic of the different mechanistic roles of supersulphide compared with hydroxide, hydrosulphide and the shorter polysulphide species. The latter species are not directly connected with photocurrent magnitude, but are related to a desorption-dissolution role of these species in the overall oxidative process, according to:



The various polysulphides, $\text{S}_{(j-1)(\text{aq})}^{2-}$, will tend to dissolve sulphur (equation (5)). However, a build-up in concentration of the longer polysulphide species will tend to suppress the rate of sulphur dissolution from the surface. This is minimized by the re-equilibration to shorter polysulphide species through equation (6). The sensitive role of hydroxide should be noted. At $\text{pH} < 13$ hydroxide depletion retards sulphur dissolution, and f_r is diminished (Fig. 2). But at $\text{pH} > 14$, tetrasulphide decreases (Fig. 1) as di- and trisulphide activities dominate¹¹⁻¹³. This can impose mass-transport limitations on the photocurrent (equations (2-4)).

Cahen *et al.*¹⁷ observed that aqueous electrolytes, which enhance the dissolution of elemental sulphur, enhance photo-

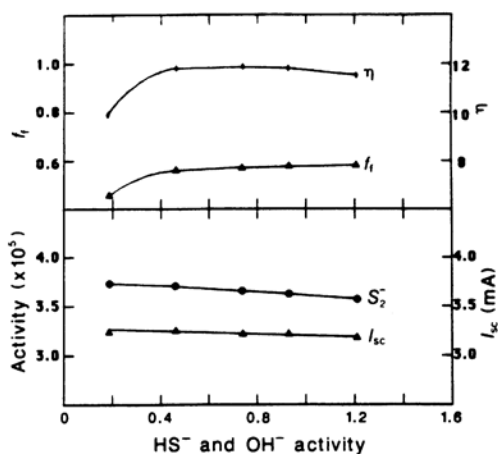


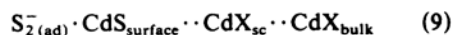
Fig. 3 The short-circuit photocurrent, I_{sc} , solar-electrical conversion efficiency, η , and fill factor, f_i , compared with supersulphide and hydrosulphide (equal to hydroxide) activities, for a 0.15-cm^2 $n\text{-CdSe}_{0.65}\text{Te}_{0.35}$ single crystal immersed in aqueous electrolytes containing sulphur (3 mol per kg H_2O) and Cs_2S (1.0–2.3 mol per kg H_2O), under an incident illumination of 75 mW cm^{-2} . Further measurement and calculation details are described in the legend to Fig. 1.

electrochemical effects in $\text{CdX}/\text{S}_{j(\text{aq})}^{2-}$ PECs. Moreover, the dissolution of an activated sulphur was related to the presence of hydroxide and hydrosulphide¹⁸ although inconsistencies arose in the analysis of the role of hydroxide and sulphide^{19,20}.

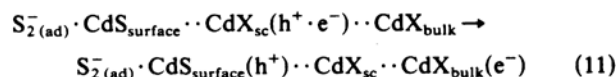
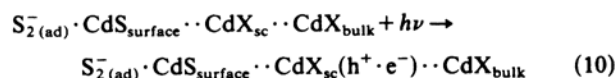
Now equations (2–6) are incorporated into an overall mechanism for the action of $\text{CdX}/\text{S}_{j(\text{aq})}^{2-}$ PECs. In both dark and photoactive environments $\text{Cd}(\text{S}_x, \text{Se}_y, \text{Te}_z)$ materials, when immersed in polysulphide electrolytes, exchange with sulphur at the surface^{1,2}



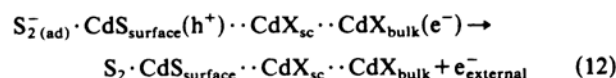
The resultant CdS surface provides stable sites for photooxidation, and must act as a window for photon absorption in the band-gap optimized space-charge region of the semiconductor, CdX_{sc} . Illumination results in useful electrical work and/or chemical fuel production, described here by the following primary process, including equilibration and adsorption of supersulphide,



photoexcitation and separation of electron-hole pair, within the semiconductor,



supersulphide oxidation and external work,

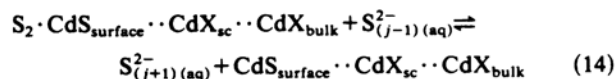


charge balance by reduction at a counter electrode involving either polysulphide reduction, a chemical product or fuel production²¹, or electrochemical storage^{3,22},

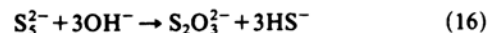


and dissolution of sulphur enhanced by re-equilibration to

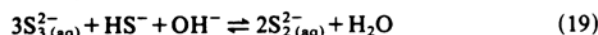
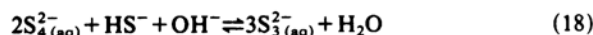
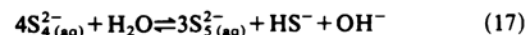
shorter polysulphides,



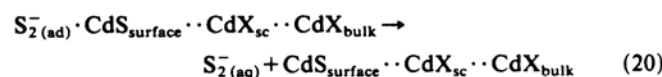
Processes deleterious to continued photooxidation can be consistently described as adverse to the overall mechanism for the action of $\text{CdX}/\text{S}_{j(\text{aq})}^{2-}$ PECs presented in equations (7–15). These include polysulphide disproportionation⁶, which will remove polysulphide from solution,



a shift of the polysulphide equilibrium away from tetrasulphide^{11–13},



or the enhancement of supersulphide desorption,



electron-hole pair recombination²³,

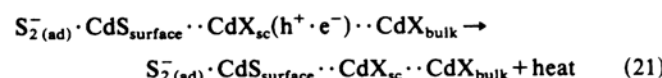
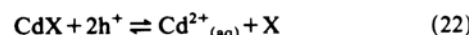
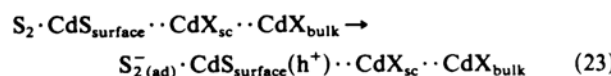


photo-induced corrosion of the semiconductor²⁴,



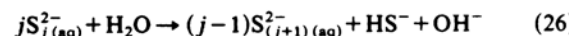
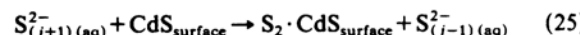
increased dark reactions, indicative of reduction at the semiconductor surface,



or reduction at an alternative material, M, with access to both semiconductor and electrolyte,



and competition to sulphur dissolution, related to depletion of shorter polysulphide species,



This study emphasizes the need for an understanding of solution-chemistry effects in interpreting photoelectrochemical systems. Determination of the reactive chemical species and relevant chemical steps for energy conversion in $n\text{-CdX}/\text{S}_{j(\text{aq})}^{2-}$ PECs, demonstrated here, can be applied to create more accurate modelling of these and other liquid solar cells^{20,23,25–27}.

I thank R. Tenne, Weizmann Institute, Rehovot, Israel, and R. Triboulet and C. Levy-Clement, Laboratoire de Physique de Solides, Meudon, France, for providing crystals.

Received 26 May; accepted 20 August 1987.

- Hodes, G. in *Energy Resources through Photochemistry and Catalysis* (ed. Gratzel, M.) 421–465 (Academic, New York, 1983).
- Hodes, G., Fonash, S. J., Heller, A. & Miller, B. in *Advances in Electrochemistry and Electrochemical Engineering* Vol. 13 (ed. Gerischer, H.) 113B–158B (Wiley, New York, 1985).
- Licht, S., Hodes, G., Tenne, R. & Manassen, J. *Nature* **326**, 863–864 (1987).
- Licht, S., Tenne, R., Flaisher, H. & Manassen, J. *J. Electrochem. Soc.* **133**, 52–59 (1986).
- Giggenbach, W. *Inorg. Chem.* **13**, 1724–1730 (1974).
- Licht, S., Hodes, G. & Manassen, J. *Inorg. Chem.* **25**, 2486–2489 (1986).
- Giggenbach, W. *Inorg. Chem.* **10**, 1306–1308 (1971).
- Licht, S. *et al. Appl. Phys. Lett.* **46**, 608–610 (1985).
- Licht, S. *J. phys. Chem.* **90**, 1096–1099 (1986).
- Muller, N. & Cahen, D. *Solar Cells* **9**, 229–245 (1983).

11. Licht, S. & Manassen, J. *J. electrochem. Soc.* **132**, 1076-1081 (1985).
12. Licht, S., Manassen, J. & Hodes, G. *J. electrochem. Soc.* **133**, 272-277 (1986).
13. Licht, S. & Manassen, J. *J. electrochem. Soc.* **133**, 277-280 (1986).
14. Hamilton, I. C. & Woods, R. *J. appl. Electrochem.* **13**, 783-794 (1983).
15. Lessner, P., Winnick, J., McLarnon, F. R. & Cairns, E. J. *J. electrochem. Soc.* **133**, 2517-2522 (1986).
16. Licht, S. *J. electrochem. Soc.* **134**, (in the press).
7. Lando, D., Manassen, J., Hodes, G. & Cahen, D. *J. Am. chem. Soc.* **101**, 3969-3971 (1979).
8. Frese, K. W. Jr & Canfield, D. G. *J. electrochem. Soc.* **131**, 2614-2618 (1984).
19. Licht, S. *J. electrochem. Soc.* **132**, 2801-2802 (1985).
20. Licht, S. & Marcu, V. *J. electroanal. Chem.* **210**, 197-204 (1982).
21. Smotkin, E. S. *et al. J. phys. Chem.* **91**, 6-8 (1987).
22. Bratin, P. & Tomkiewicz, M. *J. electrochem. Soc.* **129**, 2469-2473 (1982).
23. Flaisher, H. & Tenne, R. *J. phys. Chem.* **87**, 3061-3068 (1983).
24. Marcu, V., Tenne, R. & Rubinstein, I. *J. electrochem. Soc.* **133**, 1143-1148 (1986).
25. Orazem, M. E. & Newman, J. *J. electrochem. Soc.* **131**, 2569-2574 (1984).
26. Orazem, M. E. & Newman, J. *J. electrochem. Soc.* **131**, 2574-2582 (1984).
27. Benito, R. M. & Nozik, A. J. *J. phys. Chem.* **89**, 3429-3434 (1985).